



5-2006

The Role of Specific Interactions on the Dispersion and Properties of Carbon Nanotube-Polymer Nanocomposites

Asif Rasheed

University of Tennessee, Knoxville

Recommended Citation

Rasheed, Asif, "The Role of Specific Interactions on the Dispersion and Properties of Carbon Nanotube-Polymer Nanocomposites." PhD diss., University of Tennessee, 2006.
https://trace.tennessee.edu/utk_graddiss/4284

This Dissertation is brought to you for free and open access by the Graduate School at Trace: Tennessee Research and Creative Exchange. It has been accepted for inclusion in Doctoral Dissertations by an authorized administrator of Trace: Tennessee Research and Creative Exchange. For more information, please contact trace@utk.edu.

To the Graduate Council:

I am submitting herewith a dissertation written by Asif Rasheed entitled "The Role of Specific Interactions on the Dispersion and Properties of Carbon Nanotube-Polymer Nanocomposites." I have examined the final electronic copy of this dissertation for form and content and recommend that it be accepted in partial fulfillment of the requirements for the degree of Doctor of Philosophy, with a major in Chemistry.

Mark D. Dadmun, Major Professor

We have read this dissertation and recommend its acceptance:

Jimmy Mays, Robert Hindle, Kevin Kit

Accepted for the Council:

Dixie L. Thompson

Vice Provost and Dean of the Graduate School

(Original signatures are on file with official student records.)

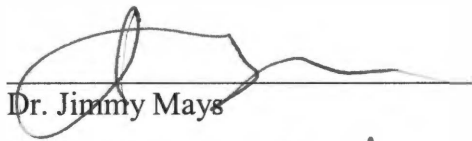
To the Graduate Council:

I am submitting herewith a dissertation written by Asif Rasheed entitled "The Role of Specific Interactions on the Dispersion and Properties of Carbon Nanotube-Polymer Nanocomposites". I have examined the final paper copy of this dissertation for form and content and recommend that it be accepted in partial fulfillment of the requirements for the degree of Doctor of Philosophy, with a major in Chemistry.

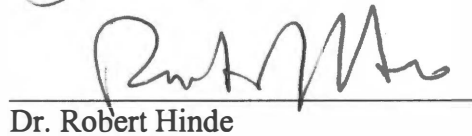


Mark D. Dadmun, Major Professor

We have read this dissertation
and recommend its acceptance:



Dr. Jimmy Mays

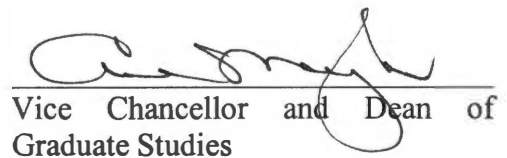


Dr. Robert Hinde



Dr. Keyin Kit

Accepted for the Council:



Vice Chancellor and Dean of
Graduate Studies

The Role of Specific Interactions on the Dispersion and Properties of Carbon Nanotube-Polymer Nanocomposites

**A Dissertation Presented for the
Doctor of Philosophy Degree
The University of Tennessee, Knoxville**

**Asif Rasheed
May 2006**

Acknowledgement

I would like to thank Professor Mark D. Dadmun for his excellent guidance and direction, which were necessary for completing this work. I would like to thank my committee members: Professor Jimmy Mays, Professor Robert Hinde and Professor Kevin Kit for their help. Special thanks to Charles O' Brian, Kevin Rice, Steve Wargacki, Scot Fontana, Sudesh Kamath, Rujul Mehta, Michael Lay, Nathan Crawford, Pradeep Kumar, Deepali Kumar, Sharddha Deodhar, Micheal Arlen, Eric Eastwood, Sriram Viwananthan, Diaz Linton, Caleb Dyer, Brian Bachner and Chang Uk Lee for their help, support and camaraderie, each aiding to the completion of this work.

I would like to thank Phil Britt and Dave Geohegan for their help and support in carbon nanotubes purification work. I would also like to thank, Ilia Ivanov for his assistance with the Raman spectroscopy, Professor Satish Kumar and Han Gi Chae for their help during our collaborative work.

Finally I would like to thank all my family whose support made this possible, specially my parents.

Abstract

This dissertation presents work that examines the role of specific chemical interactions in enhancing the dispersion of carbon nanotubes in a polymer matrix. Carbon nanotubes (CNT) possess unique mechanical, electrical and thermal properties hence can have a number of potential applications including high strength, light weight composites. Due to strong interaction among nanotubes, they stay as aggregates and hence their full potential for application is severely limited. Utilization of specific chemical interactions to induce/improve miscibility in polymer blends is well known. In this thesis, this approach is applied to carbon nanotubes polymer composites to enhance the dispersion of nanotubes in a copolymer of styrene and vinyl phenol with the idea that oxygenated functional groups on the nanotubes surface may potentially interact with the vinyl phenol groups on the polymer chain via hydrogen bonding.

The first part of this thesis compares methods to oxidize carbon nanofibers by using various oxidizing agents, such as 6M HNO₃, KMnO₄, RuO₄, and a mixture of concentrated H₂SO₄/HNO₃. The efficacy of an oxidizing agent is discussed in terms of the yield of oxidized nanofibers and the amount of oxygenated functional groups generated on the nanofiber surface.

Next, the dispersion of single walled carbon nanotubes (SWNT) in the matrix of a copolymer of styrene and vinyl phenol containing 0, 10, 20, 40 and 100% vinyl phenol, is examined. This study provides a method to control the dispersion of nanotubes in the polymer matrix by utilizing specific chemical interactions. The dispersion of the nanotubes was observed by optical microscopy. The dispersion of the SWNT in the

polymer matrix is also quantified by optical microscopy and Raman spectroscopy. Raman spectroscopy is also used to investigate preferred interactions between the SWNTs and the copolymers via the shift in the characteristic Raman peak of the SWNTs in the composites. All composites show regions of SWNT aggregates, however the aggregate size varies with composition of the PSVPh copolymer and the amount of SWNT oxidation. Optimal dispersion of the SWNT is observed in PSVPh with 20% vinyl phenol and oxidized nanotubes, which correlates with spectroscopic evidence that indicates that this system also incorporates the most interactions between SWNT and polymer matrix.

Polymer nanocomposite films containing 5 wt% single-walled carbon nanotubes (SWNT) or 5 wt% multi-walled carbon nanotubes (MWNT) with PSVPh copolymers were processed from dimethyl formamide solutions. The vinyl phenol mole ratio in the copolymers was 0, 10, 20, 30, and 40%. FTIR analysis indicates that the composites containing the copolymer with 20% vinyl phenol exhibit the maximum intermolecular interactions (hydrogen bonding) between the hydroxyl group of the vinyl phenol and the carbon nanotube functional groups. Tensile properties and electrical conductivity also are the highest in the samples containing the copolymer with 20% vinyl phenol. Thus, these results show that the optimization of the extent of intermolecular interactions between a polymer chain and a carbon nanotube results in an optimal increase in macroscopic properties. Moreover, the extent of intermolecular hydrogen bonding can be improved by optimizing the accessibility of the functional groups to participate in the non-covalent interaction. In this system, this optimization is realized by control of the amount of vinyl phenol in the copolymer, i.e., the copolymer composition.

Finally, the approach of utilizing intermolecular interaction to enhance dispersion and properties was applied to composites of carbon nanofibers. Dynamic mechanical analysis (DMA) and differential scanning calorimetry (DSC) indicate that the composites prepared from oxidized nanofibers exhibit improved thermal and structural properties relative to those prepared from unoxidized nanofibers. The optimum enhancement in the mechanical and thermal properties was observed for the composite formed from oxidized nanofiber and the copolymer containing 20% vinyl phenol.

Table of Contents

CHAPTER 1	
INTRODUCTION	1
1.1 Carbon Nanotubes and Carbon Nanofibers: Background & Properties	1
1.2 Polymer Nanotube Composites: Interaction and Interfacial Adhesion.....	6
1.3 Polymer Nanotube Composites: Dispersion	12
1.4 New Approach for Dispersion	15
1.5 Objectives of this Thesis	18
CHAPTER 2	
THE EFFICIENCY OF THE OXIDATION OF CARBON NANOFIBERS WITH VARIOUS OXIDIZING AGENTS	21
2.1 Literature Survey	21
2.2 Experimental	24
2.3 Results.....	30
2.4 Discussion	41
2.5 Conclusions.....	46
CHAPTER 3	
POLYMER-NANOTUBE COMPOSITES: OPTIMIZING THE DISPERSION IN A POLYMER MATRIX USING SPECIFIC INTERACTIONS	47

3.1	Experimental.....	47
3.2	Results and Discussion	58
3.3	Conclusions.....	84
 CHAPTER 4.....		
 POLYMER NANOTUBE NANOCOMPOSITES: CORRELATING INTERMOLECULAR INTERACTION TO ULTIMATE PROPERTIES.....		
4.1	Experimental.....	85
4.2	Results.....	88
4.3	FTIR Data Analysis	96
4.4	Discussion.....	105
 CHAPTER 5.....		
 POLYMER-NANOFIBER COMPOSITES: ENHANCING COMPOSITE PROPERTIES BY NANOFIBER OXIDATION.....		
5.1	Experimental.....	109
5.2	Results.....	112
5.3	Discussion.....	120
 CHAPTER 6.....		
 CONCLUSIONS AND FUTURE WORK.....		
 REFERENCES.....		
		131

APPENDIX.....140

VITA..... 144

List of Tables

Table		Page
1.1	Properties of various carbon forms	5
1.2	Summary of mechanical property results for CNT-polymer composites	16
2.1	Specifications of as received nanofibers	25
2.2	Comparison of oxidation routes	42
3.1	Composition and molecular weight of polymers prepared for chapter 3	53
3.2	Aggregate Size (weight average) in composites obtained by image analysis	65
3.3	Contribution of free and associated –OH in PSVPh20 and its composites	71
3.4	D* peak position shift in composite	78
4.1	Composition and molecular weight of polymers prepared for chapter 4	86
4.2	Summary of tensile results: Polymer-SWNT and Polymer-MWNT composite	90
4.3	Curve fitting results for PSVPh polymers	99
4.4	Curve fitting results for PSVPh-SWNT composites	103
4.5	Curve fitting results for PSVPh-MWNT composites	106
5.1	Composition and molecular weight of polymers prepared for chapter 5	110
5.2	Storage modulus for composites of PSVPh and CNF	116
5.3	Glass transition temperature (T _g , °C) of PSVPh and composites	119

List of Figures

Figure		Page
1.1	Single walled and multi-walled Carbon nanotubes	4
1.2	Schematic of various states of dispersion of carbon nanotubes into a polymer matrix.	14
1.3	Schematic of hydrogen bonding interaction between SWNT and PSVPh copolymer	19
2.1	Representative SEM image of CNF	26
2.2	SEM image of CNF (a) treated with H ₂ SO ₄ /HNO ₃ and (b) further treated with piranha solution	31
2.3	SEM image of CNF (a) treated with KMnO ₄ and (b) further treated with piranha solution.	32
2.4	SEM image of CNF (a) treated with RuO ₄ and (b) further treated with piranha solution	33
2.5	SEM image of CNF treated with 6M HNO ₃ .	35
2.6	SEM image of CNF treated by piranha solution.	36
2.7	Raman Spectra of carbon nanofibers (a) Untreated (b) oxidized by concentrated H ₂ SO ₄ /HNO ₃ mixture, (c) oxidized by 6M HNO ₃ , (d) oxidized by H ₂ SO ₄ /H ₂ O ₂ , (e) oxidized by KMnO ₄ and (f) oxidized by RuO ₄ .	38
2.8	FTIR spectra of octadecylamine and derivatized carbon nanofiber.	40
2.9	Comparison of yield versus the ratio I(D)/I(G) (■) and number of acidic sites/g CNF (▲) for the oxidized CNF treated by various oxidizing agents.	43
3.1	Synthesis scheme for poly(styrene-co-vinyl phenol) copolymer.	49
3.2	NMR spectra of Poly(styrene-co-acetoxystyrene, 20%) and PSVPh20	52
3.3	SEM of (a) raw SWNT (b) purified SWNT	55
3.4	TGA of purified SWNT	56

3.5	Raman Spectra of purified and oxidized SWNT	57
3.6	Optical Micrographs and histograms of the aggregates from image analysis of (a) PS+1%p-SWNT, (b) PS+1% ox-SWNT.	60
3.7	Optical Micrographs and histograms of the aggregates from image analysis of (a) PSVPh10+1%p-SWNT, (b) PSVPh10+1% ox-SWNT.	61
3.8	Optical Micrographs and histograms of the aggregates from image analysis of (a) PSVPh20+1%p-SWNT, (b) PSVPh20+1% ox-SWNT.	62
3.9	Optical Micrographs and histograms of the aggregates from image analysis of (a) PSVPh40+1%p-SWNT, (b) PSVPh40+1% ox-SWNT.	63
3.10	Optical Micrographs and histograms of the aggregates from image analysis of (a) PVPh+1%p-SWNT, (b) PVPh+1% ox-SWNT.	64
3.11	Average aggregate size of p-SWNT (■) and ox-SWNT (▲) in composite versus copolymer composition.	67
3.12	FTIR spectrum of PSVPh20, PSVPh20+1% ox-SWNT and PSVPh20+1% p-SWNT in the region of –OH stretching vibrations	70
3.13	(a) Optical micrographs of PSVPh20+1%pSWNT on glass substrate (b) Color coded map of the integrated area under the G-band for this optical micrograph. The dark areas corresponds to low SWNT content whereas the Red area corresponds to highest SWNT content (c) The integrated area under the G-band along the vertical line shown in (b)	73
3.14	(a) Optical micrographs of PSVPh20+1% ox-SWNT on a glass substrate (b) The color coded map of the integrated area under the G-band for this optical micrograph. The dark areas correspond to low SWNT content whereas the Red area corresponds to the highest SWNT content (c) The integrated area under the G-band along the vertical line shown in (b)	74
3.15	Ratio of G-band intensity in the clear region to the G-band intensity in the aggregate for p-SWNT composites (▲) and ox-SWNT composites (■) as a function % vinyl phenol in the copolymer matrix.	76
3.16	D* band peak position for p-SWNT (▲) and Ox-SWNT (■) in nanocomposites as a function of the composition of the copolymer	79

	matrix. The circle (●) indicates the D* band peak position for the purified or oxidized SWNT in air.	
4.1	FTIR spectrum of SWNT	89
4.2	Normalized tensile strength (■), tensile modulus (▲) and strain to failure (◆) versus % vinyl phenol for PSVPh-SWNT composites	91
4.3	Normalized tensile strength (■), tensile modulus (▲) and strain to failure (◆) versus % vinyl phenol for PSVPh-MWNT composites.	92
4.4	Electrical conductivity of polymer composites as a function of polymer composition for SWNT composites (▲) and MWNT composites (■).	94
4.5	FTIR spectra of pure copolymers and their composites with SWNT (a) PSVPh10 & PSVPh10+5%SWNT, (b) PSVPh20 & PSVPh20+5%SWNT, (c) PSVPh30 & PSVPh30+5%SWNT and (d) PSVPh40 & PSVPh40+5%SWNT in the region of -OH vibration.	95
4.6	Example of fitting and deconvolution procedure for PSVPh30. The curves F and A are deconvoluted peaks assigned for Free and Intra-associated OH bonds respectively obtained from the fit.	98
4.7	Dependence of calculated concentration of free OH to total OH, $C_{F,-OH}/C_{T,-OH}$ (■) and associated OH to total OH, $C_{asso,-OH}/C_{T,-OH}$ (▲) on % vinyl phenol for pure copolymers.	100
4.8	Example of fitting and deconvolution procedure for and PSVPh30-SWNT. The curves F, A and I are deconvoluted peaks assigned for Free, Intra- and Inter-associated OH bonds respectively obtained from the fit.	102
4.9	Dependence of calculated concentration of free OH to total OH, $C_{F,-OH}/C_{T,-OH}$ (◆), associated OH to total OH, $C_{asso,-OH}/C_{T,-OH}$ (●), intra-associated OH to total OH, $C_{A,-OH}/C_{T,-OH}$ (■) and inter-associated OH to total OH, $C_{I,-OH}/C_{T,-OH}$ (▲) on % vinyl phenol for PSVPh-SWNT composites.	104
4.10	Dependence of calculated concentration of free OH to total OH, $C_{F,-OH}/C_{T,-OH}$ (◆), associated OH to total OH, $C_{asso,-OH}/C_{T,-OH}$ (●), intra-	107

associated OH to total OH, $C_{A,-OH}/C_{T,-OH}$ (■) and inter-associated OH to total OH, $C_{I,-OH}/C_{T,-OH}$ (▲) on % vinyl phenol for PSVPh-MWNT composites.

5.1	Storage modulus (E') versus temperature for PSVPh10 (●) and its composites with 1% unoxidized nanofibers (■), 1% oxidized nanofibers (▲) and 5% oxidized nanofibers (◆)	113
5.2	Storage modulus (E') versus temperature for PSVPh20 (●) and its composites with 1% unoxidized nanofibers (■), 1% oxidized nanofibers (▲) and 5% oxidized nanofibers (◆)	114
5.3	Storage modulus (E') versus temperature for PSVPh40 (●) and its composites with 1% unoxidized nanofibers (■), 1% oxidized nanofibers (▲) and 5% oxidized nanofibers (◆).	115
5.4	Normalized Storage modulus versus % Vinyl phenol for PSVPh+1% unoxidized-CNF (◆), PSVPh+1% oxidized CNF (▲) and PSVPh+5% oxidized CNF (■).	117
5.5	SEM images of fractured surface of composite PSVPh20+5% oxidized CNF.	121
5.6	SEM images of fractured surface of composite PSVPh40+5% oxidized CNF.	122

Chapter 1

Introduction

1.1 Carbon Nanotubes and Carbon Nanofibers: Background & Properties

The industrial revolution accelerated the search to create materials capable of sustaining heavier loads. With the advancement of polymer science, the availability of materials to engineer broadened many folds, however most of the first polymeric materials were not as strong as metals. In order to improve polymer properties, the science of blending different polymers emerged. Mixing two polymers creates a range of materials whose properties can be controlled by the composition of each polymer in the system. For instance a small amount of a stronger polymer added to a weak polymer imparts its strength in the final blend.

Carbon fibers brought about a later revolution in material science. Carbon fibers are intrinsically strong, and are utilized primarily to create high strength light weight composites with polymers. Commercial production of carbon fibers started in the 1960's, primarily to cater to the aerospace industry. Typically, carbon fibers are manufactured by the pyrolysis of a polyacrylonitrile or a pitch precursor. Structurally, carbon fibers are composed of strands of graphitic ribbons oriented parallel to the fiber axis.¹ The orientation however is not perfect and depending on the method of production, the fibers can have varying degrees of orientation. Subsequently, mechanical properties of the carbon fibers vary depending on the post production heat treatment. Typically, high

strength carbon fibers have tensile modulus ~ 250 GPa, tensile strength ~ 3.1 - 4.6 GPa¹ and surface area on the order of ~ 0.5 m²/g.²

Carbon fiber went through its own developmental stages and in the early 1990's, a new form of carbon fiber, called vapor grown carbon fibers (VCGF) or carbon nanofibers were produced.³ Carbon nanofiber, as the name implied, are smaller in diameter than traditional carbon fibers and possess better properties than conventional carbon fibers. Produced from a hydrocarbon via catalytic vapor deposition, vapor grown carbon fibers have smaller diameters (on the order of 50's to 200's nm)⁴, as well as significantly higher tensile modulus ~ 600 GPa¹ and surface area ~ 40 - 45 m²/g⁵ relative to conventional carbon fibers.

Carbon nanotubes (CNT) are another nanoscale carbon structure and were first observed by Sumio Ijima in 1991 during the synthesis experiments of fullerenes by the electric arc method.⁶ The soot deposited at certain parts of the cathode contained multiwalled nanotubes (MWNT). Subsequent research in Ijima's lab showed that by varying arc-evaporation conditions, large quantities of carbon nanotubes can be produced. The arc-evaporation method is limited to the production of multi-walled carbon nanotubes (MWNT), however a major break through in nanotube synthesis occurred in 1993 when it was discovered that the addition of metals such as cobalt to the graphite electrodes resulted in single-walled carbon nanotubes (SWNT).⁷ Structurally, a carbon nanotube is a graphite sheet rolled-over to make a cylinder. A single-walled carbon nanotube consists of only one cylinder whereas multi-wall carbon nanotubes are composed of multiple concentric tubes. Typically, SWNT have a Young's modulus of \sim

0.64 – 1.2 TPa⁸⁻¹¹ with surface area of 1180 m²/g.¹² Figure 1.1 shows the structure of typical SWNT and MWNT.

Comparison of some of the properties of these carbon allotropes are presented in Table 1.1, which also includes the properties of steel. The comparison clearly reveals that carbon nanotubes are far superior materials to the other members of the carbon family. Their tensile modulus is on the order of a tera pascal as compared to about 200 GPa for steel¹³, about 5 times stronger than steel with only 1/6 of weight. Besides mechanical strength, carbon nanotubes also possess unique electrical, electronic and thermal properties.^{14,15,16} These unique properties of carbon nanotubes have significant potential applications in a number of fields. Examples of potential application of carbon nanotubes include nanometer sized devices,¹⁷⁻²¹ field emission devices,²²⁻²⁵ and light structural materials such as conductive and high strength nanocomposites.^{26,27}

A significant application of nanotubes is in the field of polymer composites, however to realize their full potential in this application, nanotubes must be dispersed well into the polymer matrix. The high surface area of nanotubes provides a large interfacial area between the nanotubes and the polymer matrix. This greater surface area implies that a larger interfacial area can exist between the nanotubes and the polymer matrix if they are used as filler in a nanocomposite. In a composite having interfacial adhesion between the nanotubes and the polymer matrix, superior properties in their nanocomposites are expected relative to a composite with similar interfacial interactions but formed with conventional carbon fibers, which have smaller interfacial area. However, the smaller diameter and greater surface area of the nanotubes also implies stronger interactions among the nanotubes, hence it is often difficult to disperse them into

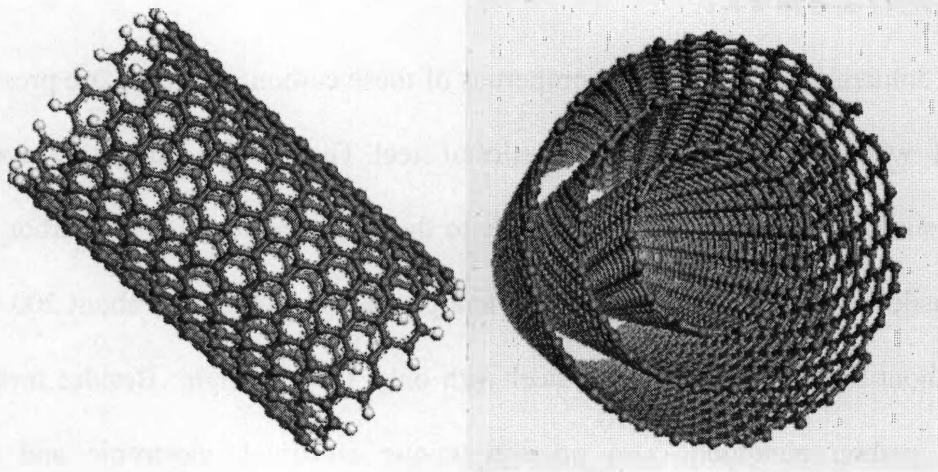


Figure 1.1: Single walled and multi-walled Carbon nanotubes

Table 1.1: Properties of various carbon forms

	Elastic Modulus (GPa)	Tensile Strength (GPa)	Density (g/cm³)	Surface area (m²/g)
SWNT	~640-1200	150	~1.2	1180
MWNT		150	2.6	
VCNF	600	~20		40-60
Carbon fiber	~207		1.7	~0.5
Steel	208	0.4	7.8	

a polymer matrix. The difficulty in achieving a uniform dispersion of individual nanotubes originates from the strong interparticle forces that exist between carbon nanotubes, which are the result of its extended π electron system. This π electron system of the nanotubes is highly polarizable, which results in significant attraction between nanotubes via van der Waals forces. These van der Waals forces are responsible for the formation of nanotube bundles, which are difficult to exfoliate, impeding the uniform dispersion of the nanotubes in a polymer matrix.

Enhancing the dispersion of the nanotube in the polymer matrix is not only critical for the mechanical properties of the resulting composite but also for thermal and electrical properties. Thus, achieving precise control of nanotube dispersion in a polymer matrix could pave the way to create materials with a broad range of tunable properties. Additionally, it is known from the polymer composite field that a strong interaction between filler and matrix is required to transfer stress across the interface and a similar mechanism will be required for polymer nanocomposite to be effective.²⁸⁻³⁰

1.2 Polymer Nanotube Composites: Interaction and Interfacial Adhesion

The interaction between a polymer and nanotubes has been addressed by theoretical studies.³¹⁻³⁵ The experimental evidence of these interactions has been demonstrated by observation of wetting of the nanotubes with polymer as observed by transmission electron microscopy (TEM)³⁶⁻³⁹ and by shifts in the characteristic peaks in Raman spectra.⁴⁰⁻⁴⁴ Attempts to quantify the amount of the interaction between the nanotube and polymer matrix have been made by stress induced fragmentation⁴⁵ and by detaching an individual nanotube from a polymer matrix using a scanning probe microscopy (SPM)

tip⁴⁶ or an atomic force microscopy (AFM) tip⁴⁷ and by the measurement of the adhesion between nanotube paper and a modified AFM tip.^{48,49}

Among various critical aspects of the nanotube-polymer interface, such as wetting, adhesion, and stress transfer, the most important and unarguably most difficult to assess is the efficiency of stress transfer from polymer matrix to the nanotubes. However, theoretical attempts have been made to understand this issue. Liao³¹ measured the interfacial shear stress of single-walled carbon nanotubes and double-walled nanotubes in polystyrene by molecular mechanics simulations. This simulation of the nanotube pull out yielded an interfacial shear stress of about 160 MPa for SWNT. This value is significantly higher than that of a conventional fiber composites system. The effect of cross-linking polyethylene with SWNT on the interfacial shear strength was studied by Frankland et al³² using molecular dynamics simulations and these results are compared with a similar system without cross links. The results reveal that a significant enhancement in the interfacial shear strength is observed for the cross-linked system relative to the non-cross linked samples. It was also predicted that the functionalization of nanotubes would have a negligible effect on the the modulus of the nanotube.³² Wagner³³ modified the Kelly-Tyson model, which is used to predict the interfacial shear strength of fiber-polymer composite systems, for SWNT-polymer systems and studied interfacial shear strength as a function of various model parameters such as tube diameter and critical tube length . The results suggest that a wide range of interfacial shear strengths are possible depending on the tube diameter, length and tensile strength. Contrary to Frankland³², Wagner predicted that minute amounts of defect present on the SWNT can decrease the tube strength, hence would result in a significant variation in its interfacial

strength. The stress-strain behavior of polyethylene with short and long SWNT was also studied by molecular dynamics simulations.³⁴ The composite with long nanotubes showed a significant enhancement in the modulus over that of pure polymer. The short nanotubes composite, owing to the low aspect ratio of the filler, did not show any improvement. Gou et al³⁵ performed molecular dynamics simulations to predict the interfacial bonding in SWNT reinforced epoxy composites. The interfacial shear strength was calculated to be 75 MPa based on SWNT pull out in this simulation.

Experimentally, the interaction between carbon nanotubes and a polymer matrix has been evidenced by polymer adhesion on nanotubes as observed under transmission electron microscopy (TEM).³⁶⁻³⁸ Lourie³⁶ observed the wetting of SWNT in an epoxy matrix under stress that is present due to thermal effects by TEM. Bower³⁷ observed the fractured surface of a polyhydroxyaminoether composite with multiwall nanotubes and found nanotube wetted by the polymer. Nanotube coated by polypyrrole has also been reported.³⁸ Polymer sheathing of MWNT by polycarbonate was also observed.³⁹

The first spectroscopic evidence of interactions between carbon nanotubes and polymer matrix was reported by Schadler⁴⁰ using Raman spectroscopy. The shift in the characteristic Raman peak of the nanotube was considered as indicative of an interaction between the epoxy matrix and MWNT under tension and compression. A large Raman shift under compression, as compared to that under tension, was observed. This implies that the load transfer in tension is poorer than in compression. It is argued that this observation is due to poor load transfer to the inner tubes of the MWNT in tension (because of weak bonding of the tube layers) and the outer tube slips past the inner ones. In compression mode, however all layers respond. Ajayan⁴¹ studied the Raman

spectroscopy of a SWNT-epoxy composite under compression and tension. No shifts in the characteristic peak position were observed under compression, however, negative shifts were observed under tension.

Wood et al^{42,43} have shown that the characteristic Raman peak position shows positive shifts when the SWNT is dispersed in liquids. The magnitude of this shift is found to be related to the cohesive energy density (CED) of the liquid. Cooper et al⁴⁴ studied composites of epoxy with SWNT and MWNT under tensile deformation using a diamond anvil cell and monitored the characteristic Raman peak position. The peak shifted to lower wave number under tensile stress and this was attributed to stress transfer to nanotubes.

Experimental evidence of interaction between carbon nanotubes and molecules containing various functional groups via formation of electron-donor acceptor complex have also been reported.⁴⁵⁻⁵³

Dispersion of SWNT in various organic solvents is studied by Ausman et al.⁴⁵ The solvents that were able to readily disperse SWNT include NMP, DMF, hexamethylphosphoramide, cyclopentanone, tetramethylene sulfoxide and ϵ -caprolactone. All of these solvents are Lewis basis having free electron pair with negligible values for hydrogen bond donation parameter. Kong et al⁴⁶ studied the adsorption of alkyamine molecules on semiconducting and metallic SWNT by electrical transport measurements. The results showed that the electrical conductance of semiconducting SWNT changed drastically upon adsorption of alkyamines, however no change was observed for metallic SWNT. The variation in electrical conductance of semiconducting SWNT upon exposure to molecules such as NO₂ (electron withdrawing)

or NH_3 (electron donating) make them suitable candidates for chemical sensors.⁴⁷ Adu et al⁴⁸ studied the thermoelectric response of a bundle of SWNT to a variety of gases such as He, N_2 , H_2 , O_2 and NH_3 . The response is interpreted to be the result of charge-transfer induced change in the Fermi energy of the nanotubes.

Interaction of various anthracene derivatives (-CN, -Br, $-\text{CH}_2\text{OH}$, -H and -OH) with SWNT was studied.⁴⁹ The coverage of the anthracene derivative on the SWNT were found to correlate well with electrochemical measurements. In general, it followed that the functional groups with higher electron affinity afforded higher surface coverage of SWNT. Wise et al⁵⁰ achieved stable dispersion of SWNT in polyimide containing a nitrile group. The stabilization of SWNT dispersion is interpreted as due to the presence of a donor acceptor interaction between the nanotubes and nitrile moiety of the polymer.

Shim et al⁵¹ studied SWNT as field effect transistors (FETs). SWNT which exhibit p-type behavior was due to electron withdrawing O_2 molecules adsorbed on the surface. However, the irreversible adsorption of polyethylene imine (PEI) on the SWNT surface transformed the nanotubes from p-type to n-type. This effect is interpreted as the ability of the electron donating amine groups of PEI to n dope the nanotubes.

Claye et al⁵² studied the doping of SWNT by potassium and lithium using Raman scattering. A downshift of the tangential mode was observed in doped SWNT. The shift was argued to be the result of electron transfer from the alkali dopant to the SWNT. Jouguelet et al⁵³ studied the chemical doping of SWNT to control its electronic properties using solutions of various organic radical anions such as fluorenone, benzophenone and naphthalene with lithium as the counter ion. The results suggest that the conductivity of the doped SWNT varies linearly with the redox potential of the dopant.

Various attempts to measure the interfacial strength between a polymer and nanotubes have been reported.⁵⁴⁻⁵⁸ The fragmentation of MWNT in an epoxy matrix under stress was observed by Wagner.⁵⁴ Using a force balance model, the interfacial shear strength was calculated for tubes of varying moduli and estimated to be in the order of 500 MPa, an order of magnitude higher than the stress transfer ability of conventional fiber composites. In a separate experiment, a scanning probe microscopy (SPM) tip was used to detach an individual SWNT bundle or a MWNT from a polymer matrix to measure the interfacial adhesion between the polymer and tubes.⁵⁵ The interfacial shear strengths for MWNT samples were measured in the range of 90-376 MPa. The variability in the results was attributed to the presence of defects on the MWNT surface. Similar pull-out experiments on SWNT ropes resulted in the breakage of SWNT ropes without being pulled out of the polymer matrix suggesting stronger nanotubes-polymer interface. MWNT pull-out experiments were also performed by Barber et al⁵⁶, where a MWNT-polyethylene-butene system was studied using atomic force microscopy (AFM). In this experiment, the MWNT was attached to the AFM tip and embedded in the polymer matrix at its melting temperature. The polymer is then allowed to cool to room temperature. The nanotube is then pulled out of the polymer matrix just above room temperature hence providing a direct measure of the force of interaction between the nanotube and the polymer matrix. The interfacial stress required to remove the MWNT from polyethylene-butene matrix was estimated to be around 47 MPa. Poggi et al^{57,58} used chemical force microscopy (CFM) to measure the adhesion between modified AFM tip and the nanotubes paper. The AFM tip was modified using alkane thiols with various end groups including methyl, hydroxyl, carboxylic and amine groups. A direct correlation

between the adhesion force with respect to each functional end group was observed. The adhesion force measured was highest for amine terminated thiol end groups among the functional groups studied.

So far, the efforts to quantify the interaction between polymer and carbon nanotubes are limited to techniques such as AFM and SPM that provide only local information on the interfacial adhesion of the nanotube-polymer composite system. How this local information on adhesion between nanotubes and polymer can be extrapolated to the bulk is a matter of investigation. Raman spectroscopy has been utilized to examine the interactions between nanotubes and polymer matrix, however, attempts to quantify the interaction by spectroscopic means has not been made. There is certainly need for an approach to systematically quantify the amount of interaction present between nanotubes and polymer matrix. Furthermore, correlation of interaction between nanotubes and polymer to the composite properties would indeed be desirable as such a correlation would enable better understanding of the composite systems and pave the way for the creation of materials with controlled properties.

1.3 Polymer Nanotube Composites: Dispersion

Along with wetting and interfacial adhesion, the uniform dispersion of carbon nanotubes in a polymer matrix is important to achieve the desired properties in a polymer nanocomposite. Wong et al⁵⁹ studied the physical interactions that exist at a carbon nanotube polystyrene interface in a polymer nanocomposite. Good adhesion of polystyrene on a MWNT surface was evident, however the presence of MWNT agglomerates were also observed. The lower values of the tensile strength and tensile modulus of the resultant nanocomposites were attributed to the poor dispersion of the

MWNT in the polystyrene matrix. The importance of the dispersion is evident in a similar study of SWNT/PMMA fiber composites where well aligned nanotubes (1 weight %) in the polymer matrix yielded only a 6% increase in the modulus. This modest enhancement in the modulus was inferred to be due to the presence of nanotubes bundles in the composites, which resulted in insufficient load transfer to the inner tubes in the bundles to improve the tensile properties of the composite.⁶⁰ Gou⁶¹ performed molecular dynamics simulations on a SWNT rope in an epoxy matrix. The results exhibit that strong interaction between the nanotube and the polymer results in efficient load transfer as the filler exists as individual nanotubes rather than nanotube ropes.

Several other studies on polymer-SWNT nanocomposites show that when SWNT are dispersed in a polymer matrix as bundles, only a modest enhancement is observed in the modulus over that of the polymer matrix.⁶²⁻⁶⁵ This minimal increase in properties of the resultant composite is proposed to be due to the slippage of individual SWNTs within bundles when stress is applied.^{11,41} Therefore it is of significant importance that nanotube bundles must be broken into individual nanotubes in order to achieve effective reinforcement of the polymer matrix. A schematic of the various degrees of nanotube dispersion into a polymer matrix is given in Figure 1.2.

Although several techniques have been employed to achieve good dispersion of nanotubes into a polymer matrix, such as the use of surfactant,⁶⁶ melt mixing⁶² and in-situ polymerization,⁶⁷ achieving the dispersion of individual nanotubes in a polymer matrix remains a challenge and impedes the progress towards creating the next generation of nanocomposites with targeted properties. A number of papers have been published reporting the properties of composites prepared from carbon nanotubes and polymer.

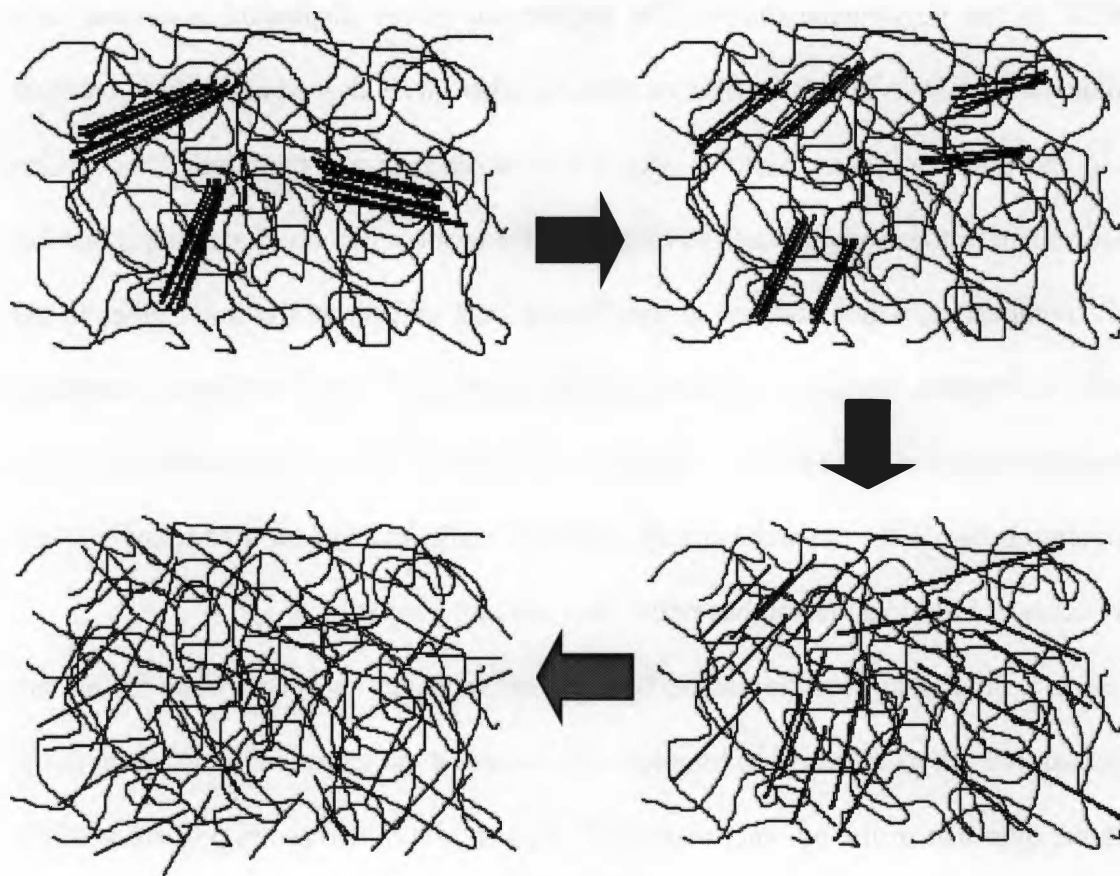


Figure 1.2: Schematic of various states of dispersion of carbon nanotubes into a polymer matrix.

Some representative results^{60,68-72} on tensile properties of carbon nanotubes-polymer composites are summarized in Table 1.2.

1.4 New Approach for Dispersion

In this thesis a new approach to achieve an improved dispersion of carbon nanotubes in a polymer matrix has been studied. The concept of this new approach goes back to the science of polymer blends. The equilibrium state of a polymer blend can be described in terms of the free energy of mixing according to;

$$\Delta G_m = \Delta H_m - \Delta S_m$$

where ΔG_m is the free energy change of mixing, ΔH_m and ΔS_m are the enthalpy and entropy of mixing respectively. For two polymers to be miscible, the free energy change of mixing must be negative. However, this is often not the case with the polymers. The long polymer chains already possess high entropy and hence don't gain entropy upon mixing with another polymer. Hence, in order to achieve a negative free energy of mixing in a polymer blend, the enthalpic contributions should play a major role. Strong intermolecular interactions between polymer chains would create a favorable enthalpic interaction which induces miscibility in the polymer blend by resulting in negative free energy of mixing. The role of intermolecular interactions to induce miscibility in polymer blends has been well studied by Coleman and Painter.⁷³⁻⁷⁵ Their work has established that the optimization of intermolecular hydrogen bonding between two amorphous polymers improves miscibility. Moreover, by controlling the extent of intermolecular interaction between the components, the extent of miscibility or dispersion in a multicomponent polymer system can be controlled. Later work by Viswanathan et al⁷⁶⁻⁸⁰ have shown that

Table 1.2: Summary of mechanical property results for CNT-polymer composites

System	Sample Preparation	% Increase in E'	Ref
PMMA+1%SWNT	Melt-mixing fiber	6	60
Epoxy+1% unmodified SWNT	Solution	5	68
Epoxy+1% COOH-SWNT	Solution	30	68
PVA-SDS+5%SWNT	Film coating	60	69
PEO+1%SWNT	Solution evaporation	3	70
PEO+4%SWNT	Solution evaporation	5	70
PMMA+0.1%SWNT	In-situ polymerization	10	71
IPP+0.6%SWNT	Solution evaporation	-7.7	72
IPP+1.8%SWNT	Solution evaporation	42	72

by controlling the extent of hydrogen bonding between a liquid crystalline polymer and an amorphous polymer, a miscibility window can be realized and a true “molecular composite” can be formed. This optimization of the extent of intermolecular hydrogen bonding correlates to the maximum accessibility of the functional groups to participate in intermolecular interaction, which is optimized by controlling the copolymer composition.

As improving and optimizing the extent of hydrogen bonding between two components is known to increase the level of dispersion and miscibility in a polymer blend, the role of hydrogen bonding in improving and controlling the dispersion of polymer nanocomposites is intriguing. Can the same principles that are known to apply to polymer blends be applied to polymer nanocomposites? To answer this question, the interactions between polymers and carbon nanotube must be systematically varied. This variation in intermolecular interaction must then be correlated to the dispersion and structural properties of the resultant nanocomposite. However, in order to apply such an approach on polymer nanotubes nanocomposite, one should ensure the presence of functional groups on carbon nanotubes that are capable of participating in intermolecular interactions.

To date, there has not been reported a similar study on polymer carbon nanotube nanocomposites, i.e; where the extent of dispersion of the nanotube in a polymer matrix has been correlated to the extent of the intermolecular interaction between the nanotube and polymer matrix. However, as this mechanism worked for one anisotropic nanoscale filler (LCP molecule⁷⁶⁻⁸⁰) it seems logical that it may also provide a method to control the dispersion of CNT in polymer matrix.

1.5 Objectives of this Thesis

This thesis studies the role of specific chemical interactions i.e, hydrogen bonding on the nanotubes dispersion in a polymer matrix and its subsequent effect on the composite properties. A schematic representation of a possible hydrogen bond interaction between a nanotube and polymer chain is shown in figure 1.3. To apply and examine this approach, it is essential to design a system of polymer-nanotube composites in which the intermolecular interaction between the two components can be controlled. This is achieved by synthesizing a copolymer of styrene and vinyl phenol with varying vinyl phenol content. The vinyl phenol groups on the copolymer chain are potential hydrogen bond donors. In the case where functional groups exist on the nanotube that are capable of participating in a hydrogen bonding interaction, an intermolecular hydrogen bonding interaction between the polymer chains and the nanotubes may result. Therefore, it is essential that the carbon nanotubes must contain a certain amount of functional groups in order to participate in the desired intermolecular interactions. It is known that carbon nanotubes contain structural defects⁸¹ as well as oxidized carbon sites.⁸² The structural defects include kinks, dangling bonds, dislocations, and 5,7 ring defects, whereas the oxygenated functional groups that exist contain carbonyls, carboxylic acids and other oxygenated functional groups. The oxygenated functional groups on the nanotube ends and surface are potential sites for interaction with the vinyl phenol groups on the copolymer chain.

This thesis attempts to answer questions such as (1) What are the efficient ways to incorporate oxygenated functional groups on carbon nanotubes/nanofibers? (2) Can the optimization of interactions between the nanotube and polymer assist in enhancing

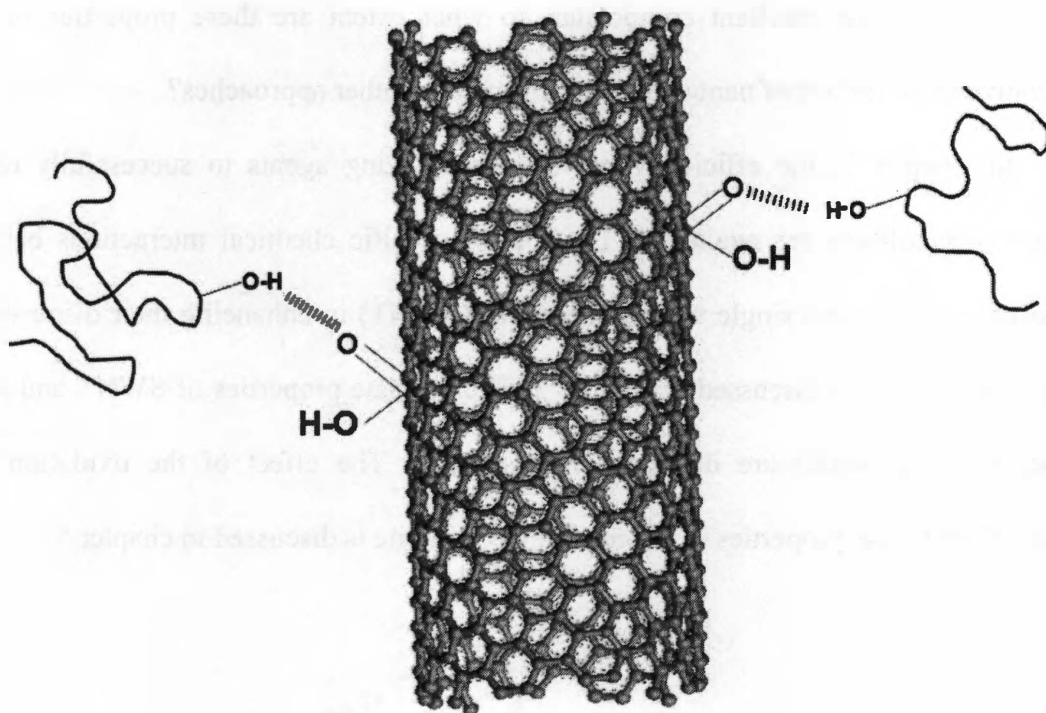


Figure 1.3: Schematic of hydrogen bonding interaction between SWNT and PSVPh copolymer.

nanotubes dispersion into the polymer matrix? (3) Does this optimization of these interactions improve the ultimate properties of the nanocomposite? (4) If it enhances the properties of the resultant composites, to what extent are these properties improved relative to properties of nanocomposites formed by other approaches?

In Chapter 2, the efficiency of various oxidizing agents to successfully oxidized carbon nanofibers are evaluated. The role of specific chemical interactions between a polymer matrix and single walled nanotubes (SWNT) in enhancing their dispersion in a polymer matrix is discussed in chapter 3. The ultimate properties of SWNT and MWNT polymer composites are discussed in chapter 4. The effect of the oxidation of the nanofiber on the properties of the resulting composite is discussed in chapter 5.

Chapter 2

The Efficiency of the Oxidation of Carbon Nanofibers with Various Oxidizing Agents

Chapter 2 compares the efficiency of various oxidizing agents by their ability to successfully oxidize carbon nanofibers. The parameters that are examined to define the effectiveness of an oxidizing agent include yield of the nanofiber after oxidation and amount of oxygenated functional groups present on the nanofiber after oxidation. A brief literature review on the oxidation of carbon nanofibers and carbon nanotubes is presented first, followed by a discussion of the experimental details. Finally, the efficiencies of the oxidizing agents studied are presented. These studies used Raman spectroscopy, SEM and indirect quantification of acidic sites on nanofibers by FTIR to analyze the oxidized nanofibers.

2.1 Literature Survey

The oxidation of carbon nanotubes and nanofibers have been reported by a number of researchers.⁸³⁻⁹⁰ Jie et al⁸³ first reported the oxidative treatment of single-walled carbon nanotubes (SWNT) by using a mixture of concentrated sulfuric and nitric acids ($\text{H}_2\text{SO}_4/\text{HNO}_3$) in order to open the nanotubes ends and shorten the nanotubes' length, however no yields were reported. The oxidative purification of nanotubes by KMnO_4 , H_2O_2 , HClO_4 and ozone has also been reported.⁸⁴ The results demonstrate that

KMnO_4 creates an oxidized tube that is free from amorphous carbon, however, additional steps are needed to remove the MnO_2 that is generated during the oxidation process. Kuznetsova et al⁸⁵ have shown that both carbonyl ($\text{C}=\text{O}$) and ether ($\text{R}-\text{O}-\text{R}$) functional groups are produced when single-walled carbon nanotubes are purified using $\text{H}_2\text{SO}_4/\text{HNO}_3$ and $\text{H}_2\text{SO}_4/\text{H}_2\text{O}_2$ mixtures. The effect of chemical oxidation on the SWNT structure by various oxidizing agents has been reported by Zhang et al.⁸⁶ The results reveal that various functional groups can be introduced when the SWNT are treated with different oxidants, including 2.6 M HNO_3 , $\text{H}_2\text{SO}_4/\text{HNO}_3$ and KMnO_4 in alkali. Dilute nitric acid has been shown to generate carboxylic acid groups on the defect sites already present on the nanotubes, while a mixture of concentrated sulfuric and nitric acid generates carboxylic acid groups on initial and newly created defect sites. Potassium permanganate (KMnO_4) introduces different amounts of hydroxyl ($-\text{OH}$), carbonyl ($\text{C}=\text{O}$) and carboxylic acids ($-\text{COOH}$) groups on the nanotubes surface. Theoretical calculations by Zhang⁸⁶ suggest that only $-\text{COOH}$, $-\text{OH}$ and $\text{C}=\text{O}$ groups can be generated during the oxidative treatment of carbon nanotubes, contrary to previous indications that ether groups can be formed as well.⁸⁴ The oxidation of carbon nanotubes to open the tube ends using HNO_3 , H_2SO_4 , aqua regia, KMnO_4 and osmium tetroxide (OsO_4) has also been reported.⁸⁷ The quantification of the amount of carboxylic acid sites by acid-base titration indicate that OsO_4 introduces fewer $-\text{COOH}$ on a nanotube than other oxidants. Hwang⁸⁸ applied KMnO_4 , OsO_4 , and RuO_4 as oxidants at 100°C to open the ends of carbon nanotubes. RuO_4 exhibited the highest efficiency for the reaction, though the tubes were completely destroyed after only 90 minutes of treatment. Ruthenium tetroxide has been utilized extensively in organic chemistry as an oxidizing agent to yield a variety of

functional groups.⁹¹⁻⁹⁴ For instance, the oxidation of naphthalene to phthalic acid⁹¹ and various substituted benzenes to carboxylic acid⁹² have been reported by treatment with ruthenium tetroxide. The selective oxidation of polycyclic aromatic hydrocarbons (PAHs) using RuO₄ has been reported by Mendez et al.⁹³ These results indicate that carboxylic acid, carbonyl, or carbonyl anhydrides can be the result of the oxidation process, depending on the structure of the original PAH. With the help of model compounds such as anthracene and phenanthrene, it has been demonstrated that RuO₄ oxidation can convert anthracene to quinone and phenanthrene to carboxylic acid, indicating its selectivity to yield specific functional groups based on PAH structure. Generally, it is believed that the chemical modification of nanotubes or nanofibers starts from the defect sites, i.e, heptagon-pentagon pairs that are under heavy strain, while other non-sp² defect sites on the nanotubes, such as -CH and -CH₂ are attacked next. In the presence of strong oxidizing agents, the integrated graphene structure is also attacked to create additional defect sites, which can subsequently react with the oxidizing agent.⁸⁶

Though the subject of the oxidation of carbon nanotubes and nanofibers has been examined by many researchers and efforts to explain the oxidation mechanism have been attempted, most of these studies have focused on identification of the functional groups by FTIR with no attention to yield of functionalized material. However, for practical applications, the yield of oxidized CNF and the density of functional groups, ideally carboxylic acids, of a given oxidation process is needed to rationally evaluate the utility of a given oxidation process. This chapter addresses this important question by correlating the oxidant strength to the yield of the oxidized nanofibers and to the quantification of oxygenated functional groups. In this chapter, the oxidation of carbon

nanofibers (CNF) by various oxidizing agents is examined. For a variety of oxidizing agents, the defect sites created as a result of the oxidation treatment are determined by Raman spectroscopy, while the quantity of carboxylic acid groups on the nanofiber is quantified by analysis of a derivatization reaction. The quality of nanofibers before and after the oxidation reaction is also observed by SEM. The oxidants used are 6M HNO₃, KMnO₄, RuO₄, and a mixture of concentrated H₂SO₄ /HNO₃. This correlation of oxidizer strength to defect sites, acidic sites, and yield will provide guidelines by which the optimal oxidation process of carbon nanofibers can be utilized in future studies.

2.2 Experimental

2.2.1 Materials

Carbon Nanofibers (CNF), grade PR24HT, were received from Applied Sciences Inc. The specifications of as received CNF and a typical SEM image of the nanofibers are given in Table 2.1 and Figure 2.1, respectively. H₂SO₄, HNO₃ and H₂O₂ were purchased from Fisher Scientific and used without any further treatment. Ru(IV) Oxide and KMnO₄ were obtained from Sigma-Aldrich and were used as received.

2.2.2 Oxidation Procedures

The oxidation using concentrated H₂SO₄/HNO₃ was completed by following a literature procedure.⁸³ 50mg of CNF was added to a mixture of concentrated H₂SO₄ (150ml) and concentrated HNO₃(50ml). The resulting nanofiber-acid mixture was sonicated for 24 hours (Branson Model 1510 Sonicator) at 40-45°C after which the mixture was diluted with 1000 ml of deionized water and filtered through 1 micron poly(tetrafluoroethylene) (PTFE) filter paper. The acid treated nanofibers were washed with 10 mM NaOH solution until neutral pH and subsequently with 10 mM HNO₃

Table 2.1: Specifications of as received nanofibers

Diameter, nm	60 - 150
Length, μ	30 - 100
Iron Content (ppm)	< 100
PAH Content(mg PAH/ g fiber)	< 1

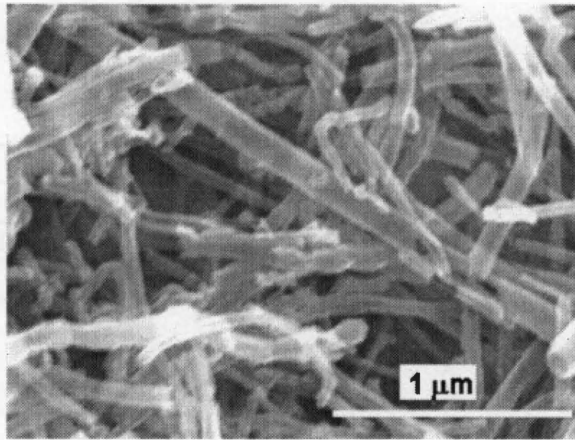


Figure 2.1: Representative SEM image of CNF

solution and again with deionized water until pH ~ 7. The resulting nanofibers were dried under vacuum at 100°C overnight. The sample was treated with piranha solution ($\text{H}_2\text{SO}_4:\text{H}_2\text{O}_2 = 4:1$) at 70°C to remove the amorphous carbon that was produced during the oxidation process.

In a typical KMnO_4 oxidation,⁹⁵ 50mg CNF and 262 mg KMnO_4 (1:0.4 molar ratio CNF: KMnO_4) were added to 25 ml 0.5M H_2SO_4 and sonicated for 4 hours at ~ 40 – 45°C. The CNF was filtered and washed with concentrated HCl followed by deionized (DI) water, 10mM NaOH, DI water, 0.5 M HCl and finally again with DI water until the filtrate indicated neutral pH. The oxidized CNF was treated with piranha solution to ensure the successful removal of amorphous carbon that was generated during the oxidation.

CNF oxidation by RuO_4 was carried out as follows:⁹¹ 5 mg RuO_2 was added to 75 ml sodium hypochlorite (6 weight% NaOCl) and stirred until RuO_2 was converted to RuO_4 . The conversion of RuO_2 to RuO_4 is detected by appearance of yellowish color. Then 250 mg of CNF was added. The mixture was then stirred for three (3) days at room temperature. This oxidized CNF was also treated with piranha solution to ensure removal of amorphous carbon that was generated during oxidation. The HNO_3 oxidation was carried out by refluxing CNF in 6M HNO_3 at 120°C for 20 hours.

The CNF was also treated with only piranha solution for 30 minutes at 70°C to determine if this treatment by itself is responsible for introducing defect sites on the nanofiber. This reaction consisted of 50mg CNF added to 100 ml piranha solution

(H₂SO₄:H₂O₂ =4:1) at 70°C for 30 minutes. The piranha treated CNF were filtered and washed with DI water until the filtrate indicated neutral pH.

2.2.3 Scanning Electron Microscopy (SEM)

In SEM, a beam of electrons is utilized to create a magnified image. The electron beam is generated by a cathode usually made of a tungsten filament. When a voltage is applied, the filaments heats up and the anode forms attractive forces for electrons. The electrons accelerate towards the anode with some electrons accelerated by the anode and down the column. The electron beam is focused into a small probe across the sample surface. The interaction of electrons with the sample results in emission of electrons from the sample surface. The emitted electrons are than collected by the detector.

The quality of CNF before and after the oxidation reaction was observed by a Hitachi S4700 scanning electron microscopy using the secondary electron (SE) detector. The SEM images were acquired at voltage of 10kV, 20 μA beam current.

2.2.4 Raman Spectroscopy

Spectroscopy is an analytical technique arising from the interaction of materials with electromagnetic radiation. The electromagnetic radiation absorbed, emitted or scattered by the molecule is analyzed. When a beam of electromagnetic radiation is irradiated on a sample, the scattered light contains photons that have the same wavelength as the incident photons. This is known as Rayleigh scattering. Additionally, a small fraction of photons scatter that have a wavelength different than the incident photons, a process known as Raman scattering. In Raman spectroscopy, the scattered photons that are different in wavelength from the wavelength of the incident photons are observed in the direction perpendicular to the incident beam. In a Raman spectrum, the intensity of

the Raman scattered radiation is plotted as a function of its frequency difference from the incident radiation, which is called the Raman shift. The defect sites on the nanofibers were analyzed by Raman spectroscopy using a Renishaw 1000 micro Raman spectrometer with a 632.8 nm excitation wavelength.

The prominent features of a first order Raman spectrum of carbon nanofibers include a graphitic induced G-band and a disorder induced D-band.⁹⁶ The G-band shoulder for CNF that appears at $\sim 1580\text{ cm}^{-1}$ is typical of graphite-like materials with many defects. The D-band for the CNF used in this study appears at around 1325 cm^{-1} . The ratio of the peak intensity of the D-band to that of the G-band $[I(D)/I(G)]$ serves as a measure of the amount of defect sites that are present on the nanofibers.⁹⁷

2.2.5 Quantification of Acidic Sites

Acidic sites on the oxidized nanofibers were quantified by reacting the oxidized CNF with thionyl chloride (SOCl_2) followed by reaction with octadecylamine (ODA) and characterizing the resulting grafted CNF by FTIR. In this reaction, 100 mg of oxidized CNF was reacted with 20 ml of SOCl_2 at 70°C for 24 hours under argon. SOCl_2 was then withdrawn from the reaction flask and 2.5 mg of ODA was added and stirred for 96 hours at $90\text{-}100^\circ\text{C}$. The final mixture was washed with ethanol to remove excess ODA. The resulting ODA grafted CNF, denoted as “derivatized CNF”, were dispersed in CCl_4 and characterized by FTIR. The C-H stretch of the grafted aliphatic chains at 2850 cm^{-1} was used to quantify the amount of ODA that was successfully grafted to the oxidized tubes and thus indicative of the number of carboxylic acid sites available on the oxidized surface. Standard solutions of ODA in CCl_4 were also prepared and used to create a calibration curve of FTIR peak intensity to ODA concentration following the procedure

reported by Hamon et al.⁹⁸ It is important to mention here that untreated nanofiber was also reacted with ODA in an identical procedure, to insure that the attachment of ODA to the CNF was solely due to covalent bonding of the ODA on the CNF through the acid chloride groups. In this process, ODA was added to untreated carbon nanofiber and stirred under similar conditions as mentioned above. The resultant mixture was washed thoroughly with ethanol. The FTIR spectrum of the resulting nanofibers did not indicate the presence of any ODA.

2.3 Results

The SEM images of the CNF oxidized by the mixture of concentrated $\text{H}_2\text{SO}_4/\text{HNO}_3$ and subsequent piranha solution treatment are shown in Figures 2.2a and 2.2b, respectively. Immediately after oxidation, the nanofibers appear to be embedded in amorphous carbon matrix that is generated during the oxidative treatment. However, after treatment by piranha solution, the SEM image indicates little to no amorphous carbon, and the resulting oxidized nanofibers are produced with an overall yield of 12%. The SEM images of the CNF treated with KMnO_4 and then further treated with piranha solution are given in Figures 2.3a and 2.3b, respectively. A small amount of amorphous carbon is apparent after the KMnO_4 oxidation process. The presence of a small amount of amorphous carbon is contrary to the earlier reported results on KMnO_4 oxidation.⁹⁵ Yield after the initial oxidation step is 70%, while after the piranha treatment for removal of amorphous carbon, the yield was only 45% of the starting nanofibers.

The SEM images of the CNF after treatment with ruthenium oxide and then further treatment with piranha solution are given in Figures 2.4a and 2.4b, respectively. The presence of amorphous carbon after this oxidation process is not as evident as for the

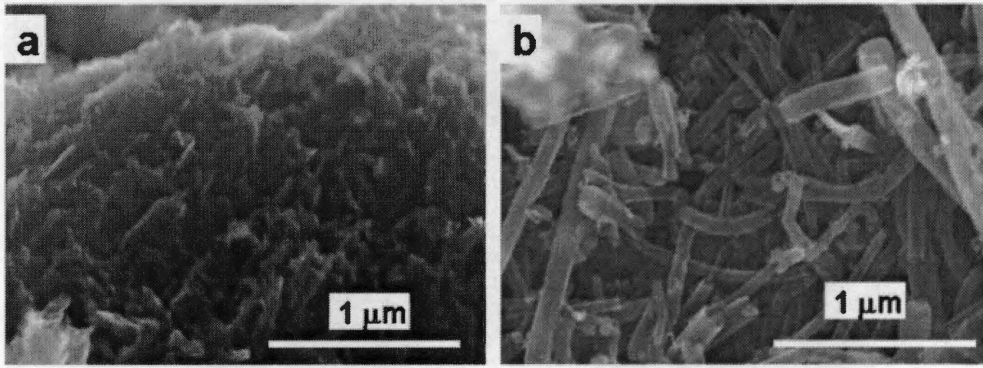


Figure 2.2: SEM image of CNF (a) treated with H₂SO₄/HNO₃ and (b) further treated with piranha solution.

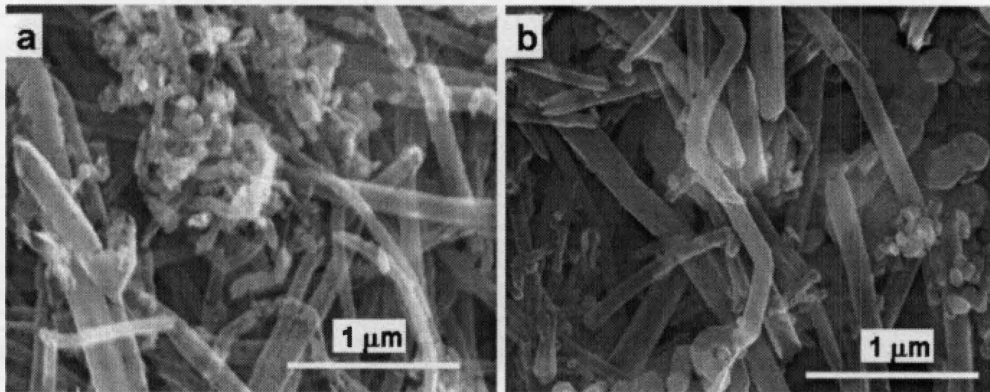


Figure 2.3: SEM image of CNF (a) treated with KMnO_4 and (b) further treated with piranha solution.

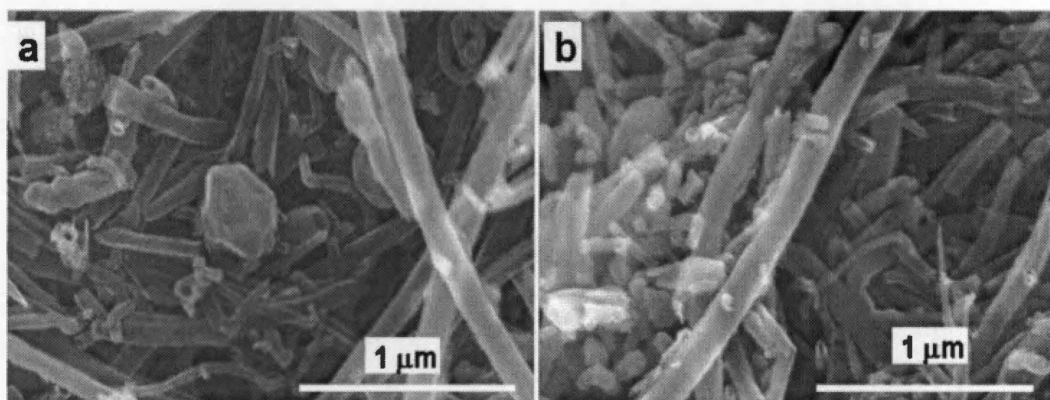


Figure 2.4: SEM image of CNF (a) treated with RuO₄ and (b) further treated with piranha solution.

previous reactions. The quality of the nanofibers appears similar before and after oxidation. The overall yield of this oxidation process is ~65%. The SEM of the 6M HNO₃ treated CNF is given in Figure 2.5. The SEM image indicates that the quality of the nanofiber is similar before and after the oxidation treatment, i.e. there is very little amorphous carbon formation during this process. The yield is about 70%. The H₂O₂/H₂SO₄ (piranha solution) is primarily used to remove amorphous carbon that is produced during the oxidative treatment by strong oxidizing agents. However, it is important to verify that this process does not dramatically impact the oxidation of the CNF. Thus, a neat CNF was treated with piranha solution under the same conditions for the same amount of time (30 minutes) as was used to treat oxidized CNF to remove amorphous carbon. The SEM image (Figure 2.6) of this piranha treated CNF indicates no significant formation of amorphous carbon. The yield of this reaction is 76%.

2.3.1 Raman Spectroscopy of CNF

As mentioned in the experimental section, the prominent features of a first order Raman spectrum of carbon nanofibers include a graphitic induced G-band and a disorder induced D-band.⁹⁶ In a graphitic material such as nanofibers, D-band corresponds to the amount of any non-sp² carbon present and would contribute to the D-band in Raman spectrum. Since the oxidation reaction would generate oxygenated functional groups on the nanofiber surface, each carbon atom that undergoes reaction would lose its sp² character, hence contributing to the peak intensity of D-band in the Raman spectrum. However, the G-band is not expected to alter its intensity due to such modification of the nanofiber surface. Hence a ratio of D-band intensity to G-band intensity, I(D)/I(G) can serve as a qualitative measure of amount of defects present in the carbon nanofiber. It is

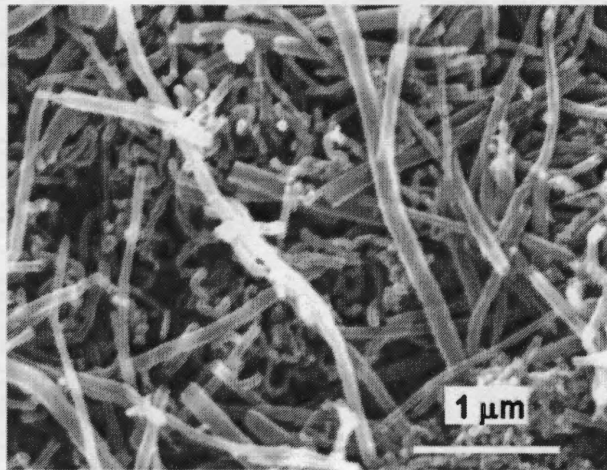


Figure 2.5: SEM image of CNF treated with 6M HNO₃.

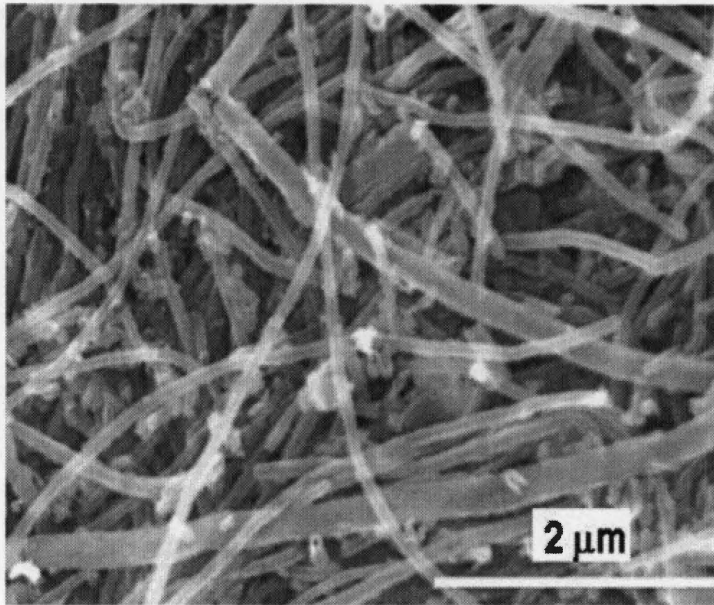


Figure 2.6: SEM image of CNF treated by piranha solution.

important to remember that the defect sites after oxidation may include carboxylic acid, carbonyl, hydroxyl, ether groups etc, depending on the oxidizing agent. Thus, the quantity $I(D)/I(G)$ is used in this study as a measure of the extent of oxidation of the CNF for a given oxidation process.

The Raman spectra of the untreated and oxidized CNF are given in Figure 2.7. The value of $I(D)/I(G)$ ratio is 0.25 for the untreated CNF. The oxidation process that increases this value the most, and thus introduces the most defects in the CNF, is the oxidation by the concentrated H_2SO_4/HNO_3 mixture. The $KMnO_4$ oxidized nanofibers experienced an increase in the value of $I(D)/I(G)$ up to 0.61, while the nanofibers oxidized by RuO_4 result in a value of $I(D)/I(G)$ that is 0.55. The 6M HNO_3 treatment however, only exhibited a small increment in the $I(D)/I(G)$ ratio to 0.34. The nanofibers treated with piranha solution for 30 minutes did not exhibit any significant change in the amount of defect sites. This suggests that the reaction of the tubes with piranha solution for 30 minutes is not sufficiently harsh to introduce defects on the nanofibers, though it is efficient at removing amorphous carbon.

It is important to remember that the D-band in the Raman spectra originates from a variety of defects present on the nanofibers. The enhanced D-band in the nanofiber after oxidative treatment originates from alterations to the graphene sheet due to the oxidation of the nanofiber surface and introduction of various functional groups to that surface. While it is difficult to estimate the amount of each functional group introduced on the nanofibers during the oxidation process, there is a literature procedure to quantify the amount of carboxylic acid sites on the nanofibers.⁹⁸

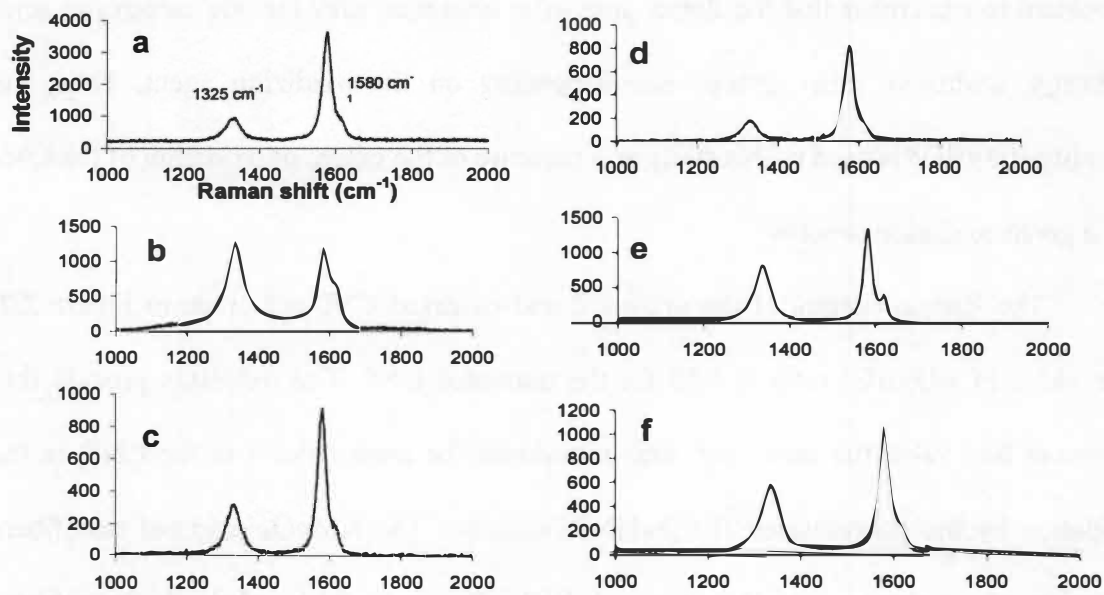
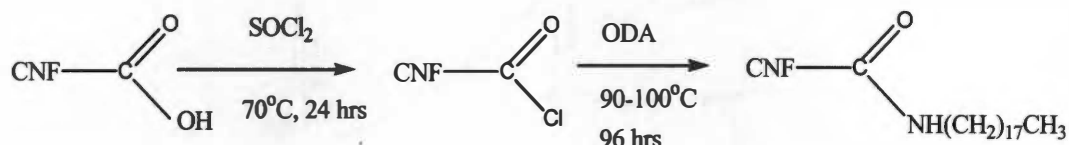


Figure 2.7: Raman Spectra of carbon nanofibers (a) Untreated (b) oxidized by concentrated H₂SO₄/HNO₃ mixture, (c) oxidized by 6M HNO₃, (d) oxidized by H₂SO₄/H₂O₂, (e) oxidized by KMnO₄ and (f) oxidized by RuO₄.

2.3.2 Quantification of Acidic sites on oxidized CNF

Acidic sites introduced on the nanofibers can be quantified by reacting the oxidized CNF with thionyl chloride followed by reaction with octadecylamine (ODA) and characterizing the derivatized CNF by FTIR.



The result of this reaction process is a series of grafted aliphatic chains on the nanofiber surface selectively at the carboxylic acid sites. Upon completion of this reaction, the FTIR spectrum of the derivatized CNF indicates the incorporation of ODA onto the nanofiber. The FTIR of the derivatized CNF is shown in Figure 2.8. The ODA derivatized CNF shows the C-H bond stretching of the $-\text{CH}_2$ and $-\text{CH}_3$ groups at 2920 cm^{-1} and 2850 cm^{-1} , respectively. For the purpose of quantifying the amount of grafted ODA, the C-H stretching vibration at 2850 cm^{-1} was examined. The amount of ODA on the derivatized CNF was quantified by comparing the intensity of this peak to that of a calibration curve of ODA, which was measured at various concentrations in CCl_4 . Then the amount of ODA is converted to moles of ODA by dividing the amount by molar mass of ODA and then to the number of ODA molecules by multiplying it with Avagadro's number. Next, assuming the number of ODA molecules correspond to the number of acidic sites present on nanofiber surface, the number is divided with the mass of oxidized sample to obtain the acidic sites per gram of nanofiber. The details of this calculation procedure can be found in reference 98.

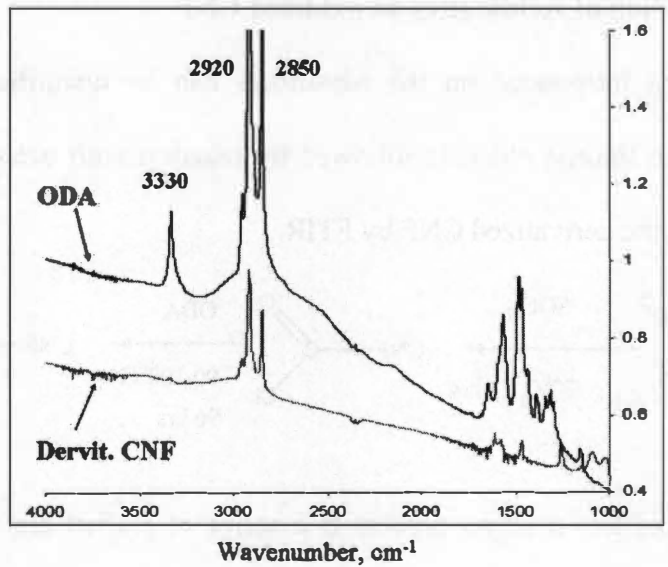


Figure 2.8: FTIR spectra of octadecylamine and derivatized carbon nanofiber.

The results reveal 1.55 mole percent ODA on the surface of the CNF that is oxidized by RuO_4 , which corresponds to 7.77×10^{20} acidic sites per gram of CNF. The number of acidic sites on the 6M HNO_3 treated CNF is 3.27×10^{20} per gram of CNF, while the highest number of acidic sites, 1.05×10^{21} per gram CNF was found on the nanofibers treated with concentrated $\text{H}_2\text{SO}_4/\text{HNO}_3$. Finally, the number of acidic sites for the KMnO_4 treated CNF is 4.58×10^{20} per gram of CNF. The yield, $I(\text{D})/I(\text{G})$ and amount of acidic sites/g CNF after each oxidation treatment is summarized in Table 2.2.

2.4 Discussion

Among the oxidizing agents examined in this study, the overall yield of oxidized nanofibers follows the trend: $6\text{M HNO}_3 > \text{RuO}_4 > \text{KMnO}_4 > \text{H}_2\text{SO}_4/\text{HNO}_3$. For the amount of defects found on the nanofibers after each oxidation treatment, as measured by the ratio $I(\text{D})/I(\text{G})$, the trend is, not surprisingly, almost the opposite of the yield: $\text{H}_2\text{SO}_4/\text{HNO}_3 > \text{KMnO}_4 \approx \text{RuO}_4 > 6\text{M HNO}_3$. The trend is $\text{H}_2\text{SO}_4/\text{HNO}_3 > \text{RuO}_4 > \text{KMnO}_4 > 6\text{M HNO}_3$ for the amount of carboxylic acid sites found on the nanofibers after oxidation. The correlation of the yield of each oxidation process to the number of defect sites as measured by $I(\text{D})/I(\text{G})$ and to the number of acidic sites is plotted as Figure 2.9. In general, the stronger oxidants generate more defects on the nanofibers, which results in a lower yield of oxidized CNF. This trend is very obvious when comparing the 6M HNO_3 and concentrated $\text{H}_2\text{SO}_4/\text{HNO}_3$ processes.

The oxidation using 6M HNO_3 yields 70% oxidized CNF with an $I(\text{D})/I(\text{G})$ ratio of 0.34, while the concentrated $\text{H}_2\text{SO}_4/\text{HNO}_3$ mixture, on the other hand, yields only about 12% oxidized CNF with an $I(\text{D})/I(\text{G})$ ratio of 1.07. Also, the quantification of acidic sites reveals approximately 3 times more carboxylic acid sites are generated on the

Table 2.2: Comparison of oxidation routes

	Yield after Oxidation	Yield after Piranha Sol. Treatment	Overall Yield	Formation of amorphous carbon	I(D)/I(G)	Acidic sites/g CNF
Untreated CNF					0.25	
Conc.H ₂ SO ₄ /HNO ₃	40%	31%	12%	Yes	1.07	1.05*10 ²¹
6M HNO ₃	70%	NA	70%	No	0.34	3.27*10 ²⁰
KMnO ₄	74%	61%	45%	Yes	0.61	4.58*10 ²⁰
RuO ₄	80%	81%	65%	No	0.55	7.77*10 ²⁰
H ₂ SO ₄ /H ₂ O ₂	76%	NA	76%	No	0.22	

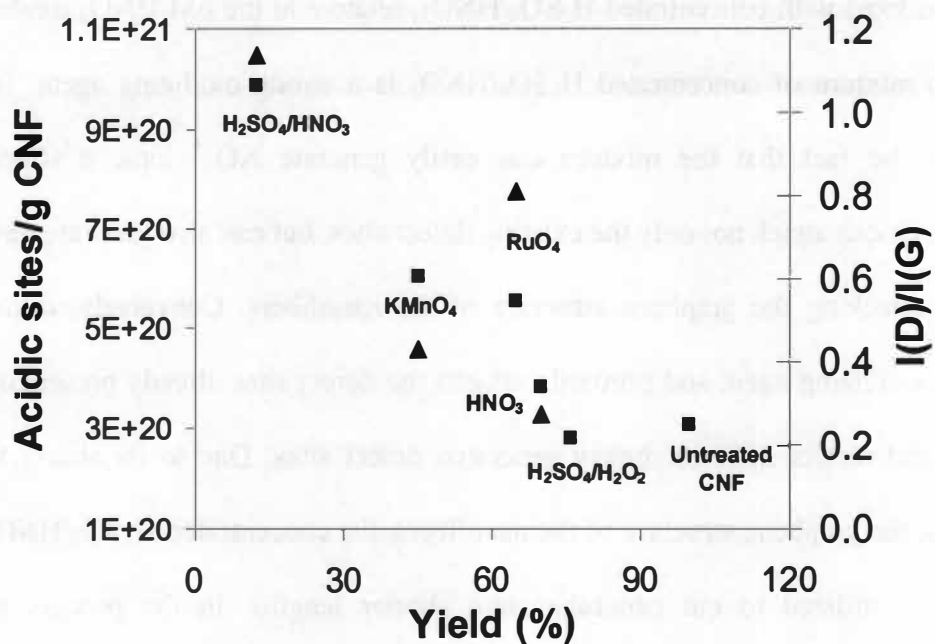


Figure 2.9: Comparison of yield versus the ratio $I(D)/I(G)$ (■) and number of acidic sites/g CNF (▲) for the oxidized CNF treated by various oxidizing agents.

CNF that are oxidized with concentrated $\text{H}_2\text{SO}_4/\text{HNO}_3$, relative to the 6M HNO_3 treated nanofibers. The mixture of concentrated $\text{H}_2\text{SO}_4/\text{HNO}_3$ is a strong oxidizing agent. Its efficacy lies in the fact that the mixture can easily generate NO_2^+ ions, a strong electrophile, which can attack not only the existing defect sites, but can also generate new defect sites by attacking the graphene structure of the nanofibers. Conversely, dilute HNO_3 is a mild oxidizing agent and primarily attacks the defect sites already present on the nanofibers and results in fewer newly generated defect sites. Due to its ability to efficiently attack the graphene structure of the nanofibers, the concentrated $\text{H}_2\text{SO}_4/\text{HNO}_3$ mixture has been utilized to cut nanotubes into shorter lengths. In the process of oxidizing and cutting nanotubes and nanofibers, significant amounts of nanofibers are destroyed and amorphous carbon is generated.

The amount of defect sites on the nanofibers oxidized by the RuO_4 and KMnO_4 processes are very similar, with values of $I(\text{D})/I(\text{G})$ of 0.55 and 0.61 respectively, however, significant differences are observed for the yield and amount of $-\text{COOH}$ groups present on the nanofibers after each oxidation process. The yield for CNF oxidized by RuO_4 is about 65% as opposed to 45% for the KMnO_4 oxidized CNF. Additionally, there are approximately 1.7 times as many carboxylic acid functional groups in the RuO_4 oxidized nanofibers relative to the KMnO_4 oxidized nanofibers. This structural difference suggests that the KMnO_4 oxidized nanofibers contain significant amounts of other oxygenated functional groups such as $-\text{OH}$ and other $\text{C}=\text{O}$ groups on the nanofiber as a result of the oxidation process.

Qualitatively, the results of the oxidative treatment of carbon nanofibers by concentrated $\text{H}_2\text{SO}_4/\text{HNO}_3$, dilute HNO_3 and KMnO_4 are in agreement with previously

reported results for the creation of functional groups on carbon nanotubes by oxidation.⁸⁶ However, the results of our Ru based oxidation of nanofibers does not agree as well with previous examinations of the oxidation of nanotubes and nanofibers using ruthenium oxides. For instance, the work by Hwang⁸⁸ indicates that Os and Ru based oxidations are very efficient at opening the nanotubes' ends, whereas another study reveals OsO₄ generates fewer –COOH than other oxidants utilized, including HNO₃, H₂SO₄ and KMnO₄.⁸⁷ These contradictory observations may be due to structural differences of the nanotubes and nanofibers that are examined. The extent and rate of oxidation unarguably depends on the structural features of the nanotubes, which include, but are not limited to, curvature, pentagon, heptagon ring position and helicity.⁸⁹

Thus, while the results provide guidelines that can be used to devise optimal oxidation procedures for carbon nanofibers and nanotubes, it must be emphasized that the behavior of moderate-strength oxidizing agents, such as Os and Ru based oxidants and KMnO₄, will depend intimately on the specific structure of the carbon nanotube or nanofiber that is being oxidized. For these carbon nanofibers, RuO₄ exhibits a higher yield of nanofibers that are oxidized and a significant amount of –COOH present, which makes this oxidation procedure optimal for these nanofibers. Moreover, our results quantify the correlation between the oxidizing strength of the oxidant to the yield and extent of introduction of defects. This data can be utilized to design optimal oxidation procedures for other nanofibers and nanotubes, a process that can be optimized dependent on the relative importance of yield, the targeted functionality, and the need for the introduction of oxygenated defect sites.

2.5 Conclusions

The results show that the different oxidizing agents vary in their ability to effectively oxidize CNF. A combination of concentrated $\text{H}_2\text{SO}_4/\text{HNO}_3$, a severe oxidative treatment, results in the generation of amorphous impurities thus lowering the overall yield of oxidized CNF, but substantial oxygenated defects on the remaining CNF. Oxidation of the CNF by 6M HNO_3 , the mildest oxidant, introduced a smaller amount of defect sites and $-\text{COOH}$ groups, but improved the yield. Ruthenium tetroxide, which is a well known oxidizing agent for aromatic compounds, selectively oxidized the CNF to offer substantial $-\text{COOH}$ groups, with good overall yields and a moderate increase in the defect sites. Nanofibers oxidized by KMnO_4 provide fewer carboxylic acid groups than the RuO_4 treatment but a similar amount of overall defects, and thus must introduce a broader range of oxygenated functional groups to the nanofiber.

Chapter 3

Polymer-Nanotube Composites: Optimizing the Dispersion in a Polymer Matrix using Specific Interactions

Chapter 3 describes the role of specific chemical interactions between a polymer matrix and single walled nanotubes (SWNT) in enhancing their dispersion in a polymer matrix. The dispersion of SWNT in composites that contain purified and oxidized SWNT are prepared and examined by optical microscopy and Raman spectroscopy. Raman spectroscopy is also utilized to determine the interaction between the polymer and the nanotubes. The copolymers used in this study contain styrene and vinyl phenol with varying vinyl phenol content. The detailed account of copolymer synthesis and characterization procedure is presented in the experimental section. The copolymers containing 10, 20 and 40% vinyl phenol are utilized in this study and are designated as PSVPh10, PSVPh20 and PSVPh40, respectively. The polymer containing 100% vinyl phenol, PVPh is also examined as a matrix for the nanocomposites.

3.1 Experimental

Polymer Synthesis:

The synthesis of the copolymers, poly(styrene-co-vinyl phenol) (PSVPh) was carried out by free radical polymerization of styrene and 4-acetoxystyrene in appropriate amounts using 2,2'-azobisisobutyronitrile (AIBN) as the initiator and dioxane as the

solvent. The resulting copolymer is hydrolyzed by hydrazine hydrate using dioxane as the solvent to yield PSVPh. In a typical synthesis of the copolymer (20% vinyl phenol), styrene (75 mL, 0.654 mol), 4-acetoxystyrene (25 mL, 0.164 mol) and AIBN (45 mg) are transferred to a 3-neck round bottom reaction flask containing anhydrous dioxane (200 mL). The mixture was degassed by freeze-pump-thaw cycles. The reaction mixture was stirred by a magnetic stirrer at 65°C for 20 h under argon flow. The resulting copolymer was precipitated in cold methanol and dissolved in dioxane and precipitated in cold methanol an additional time to ensure removal of unreacted monomers. The copolymer was then dried under vacuum at 80 – 90°C overnight. The resulting copolymer composition was determined using NMR. The acetoxystyrene groups were converted to vinyl phenol groups by hydrolysis. In a typical hydrolysis reaction, poly(styrene-co-acetoxystyrene) (20 g) was dissolved in dioxane (150 mL); hydrazine hydrate (60 mL) was then added to the reaction, and the mixture was stirred for 48 h at room temperature under argon. The hydrolyzed copolymer (PSVPh) was precipitated using cold methanol for copolymers with 10 and 20% vinyl phenol and hexane as the nonsolvent for copolymers with 40% vinyl phenol. The completion of the hydrolysis reaction was confirmed by the disappearance of the peak for the acetoxy group by NMR. The copolymers with 10, 20 and 40% vinyl phenol content are designated as PSVPh10, PSVPh20 and PSVPh40 respectively. The copolymers containing 10, 20 and 40% vinyl phenol groups were utilized in this study and are designated as PSVPh10, PSVPh20 and PSVPh40, respectively. The reaction scheme for the copolymer synthesis is given in Figure 3.1. The pure poly(vinyl phenol) was purchased from Polysciences Inc. The GPC measurement reveals the molecular weight of poly(vinyl phenol) to be 17,000 g/mol.

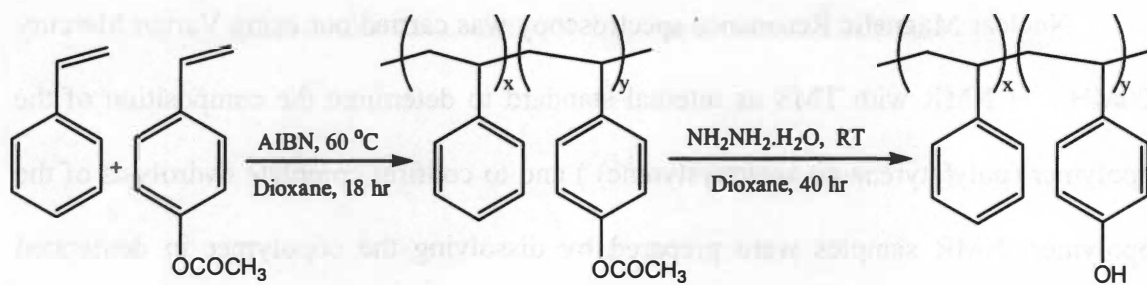


Figure 3.1: Synthesis scheme for poly(styrene-co-vinyl phenol) copolymer.

Nuclear Magnetic Resonance (NMR)

Nuclear Magnetic Resonance spectroscopy was carried out using Varian Mercury 300MHz ^1H NMR with TMS as internal standard to determine the composition of the copolymer (poly(styrene-co-acetoxystyrene)) and to confirm complete hydrolysis of the copolymer. NMR samples were prepared by dissolving the copolymer in deuterated chloroform (except for 40%vinylphenol content copolymer, which was dissolved in deuterated dimethyl sulfoxide). The ^1H NMR peak assignment for poly(styrene-co-acetoxystyrene) are;

6.2-7.2 ppm	multiplet	9H	aromatic protons
2.2 ppm	singlet	3H	-OCOCH ₃
1.7 ppm	triplet	1H	-CH
1.4 ppm	doublet	2H	-CH ₂

The peak at 2.2 ppm appears due to the presence of the acetoxy groups, and thus the disappearance of this peak is indicative of complete hydrolysis of the copolymer. The composition (molar) of poly(styrene-co-acetoxystyrene) is determined using the acetoxy peak (2.2 ppm) and aromatic peak (6.2-7.2 ppm).⁹⁹ Integration of peaks at 2.2 ppm and 6.2-7.2 ppm gives the area under these peaks. Peak area under the 2.2 ppm (acetoxy groups) can be normalized by dividing the area by number of protons (3 for acetoxy group),

$$A_{\text{acetoxy}} = \text{Area of 2.2 ppm peak} / 3$$

The normalized peak area (per proton) for styrene can be calculated by subtracting the peak area for the acetoxystyrene (4 aromatic protons) from the total peak area in the region 6.2-7.2 ppm, which leaves the peak area for styrene only and dividing this by 5

(number of styrene protons) gives normalized area per proton corresponding to styrene repeating unit.

$$A_{\text{styrene}} = [(\text{Total area of region from 6.2-7.2 ppm}) - 4 A_{\text{acetoxy}}] / 5$$

The percentage of acetoxystyrene groups in the copolymer is then calculated as;

$$\% \text{ acetoxystyrene} = A_{\text{acetoxy}} / (A_{\text{acetoxy}} + A_{\text{styrene}}) * 100$$

The NMR spectra of poly(styrene-co-acetoxystyrene, 20) and PSVPh20 are given in Figure 3.2.

Gel Permeation Chromatography (GPC)

The molecular weights and the polydispersity of the polymers are determined using Gel Permeation Chromatography. The technique is based on separating the polymer samples according to their size using a column made of porous material. The instruments must be calibrated by using well-characterized, narrow molecular weight samples. The molecular weight and polydispersity of an unknown sample can be determined by comparing the elution times of the standard and the unknown. Gel permeation chromatography was carried out using PL-GPC20 Integrated GPC system by Polymer Laboratories Inc, equipped with Ultrastyrigel columns with a refractive index detector. THF was used as elution solvent. The exact compositions, molecular weights and polydispersity of these copolymers are given in Table 3.1.

SWNT Purification

SWNT were produced by laser ablation using a Nd-YAG laser of a Dylon target containing 1 wt% of Ni and Co at 1100 °C under 500 Torr argon at Oak Ridge National Laboratory.¹⁰⁰ For purification, raw SWNTs were refluxed in 6M HNO₃ for 16 h. The resulting reaction mixture was filtered through 1 micron PTFE filter paper, the solids were

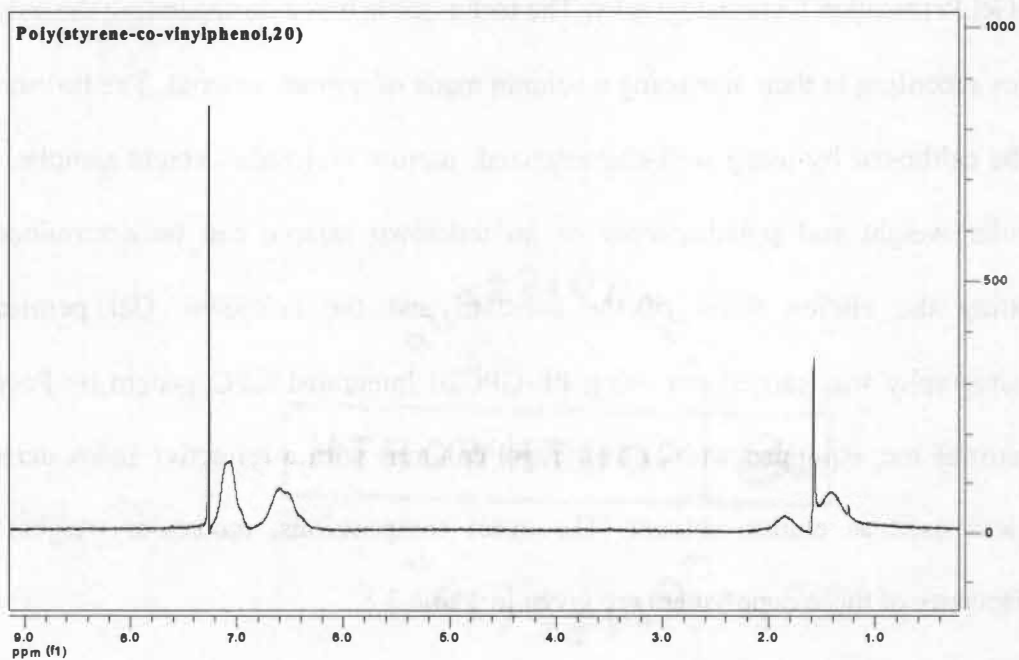
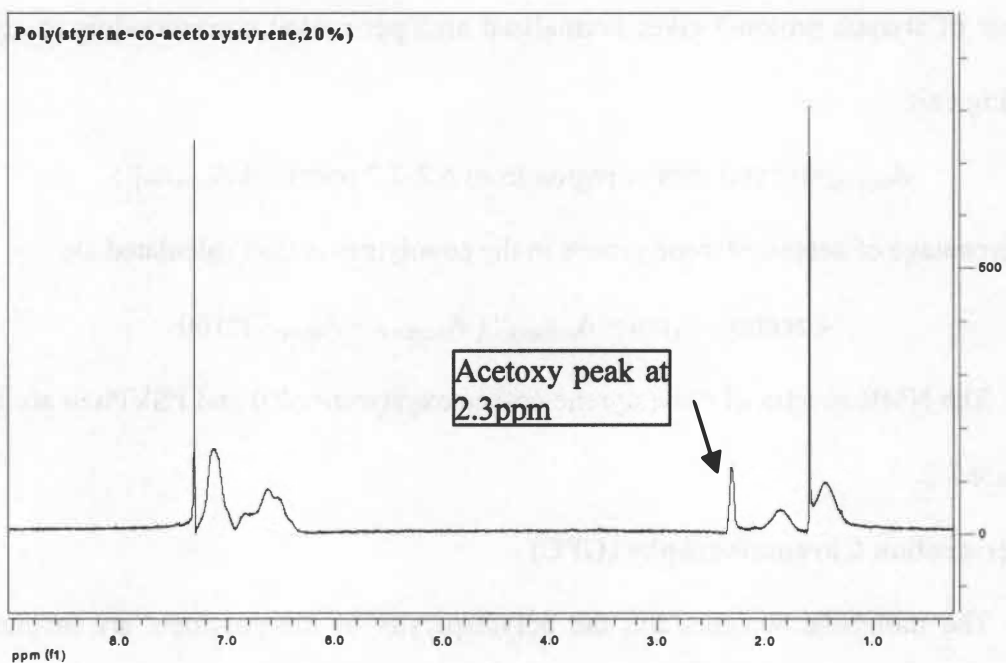


Figure 3.2: NMR spectra of Poly(styrene-co-acetoxystyrene, 20%) and PSVPh20.

Table 3.1: Composition and molecular weight of polymers prepared for chapter 3

	%Vinyl phenol	Mn (g/mol)	PDI
PS	0	105,800	1.58
PSVPh10	11.2	93,800	1.71
PSVPh20	21.5	101,000	1.60
PSVPh40	40.7	91,700	1.72
PVPh*	100	17,000	

* Supplied by Polysciences Inc.

repeatedly washed with Milli-Q water until the filtrate was neutral, and the solids dried under vacuum at 100°C. The resulting SWNT was then thermally oxidized at 450°C for 70 min in the presence of air to remove residual amorphous carbon and subsequently washed with concentrated HCl/HF to remove metal impurities (Ni and Co). The resulting SWNT was then characterized by SEM and TGA for its quality and subjected to another thermal oxidation at 500°C for 30 min as well as an additional concentrated HCl/HF wash. Purified SWNT are designated as p-SWNT. The SEM of raw and purified SWNT is shown in Figure 3.3 and the TGA of purified SWNT is shown in Figure 3.4, indicating the level of purification attained.

SWNT Oxidation

Purified SWNT were oxidized by refluxing in 6M HNO₃ for 16 h. This treatment generates oxygenated functional groups on the ends and surface of the SWNT.⁹² The oxidized SWNT is designated as ox-SWNT. Comparison of the Raman spectra of p-SWNT and ox-SWNT is given in Figure 3.5. The increase in the D-band intensity at ~1350 cm⁻¹ indicates the successful incorporation of defects on the nanotube surface and ends.

Nanocomposite Preparation

p-SWNT (5mg) was added to DMF (5 mL) and sonicated for 1 minute using a sonic horn (Cole Parmer ultrasonic processor 750W operated at 40%). The copolymer (50.0 mg) was separately dissolved in DMF (2 mL). The p-SWNT/DMF solution (0.50 μL) was then added to the copolymer solution (50.0mg polymer, 0.50mg p-SWNT in total of 2.5mL DMF ~ 2 weight % solution). The polymer-SWNT solution was then sonicated for an

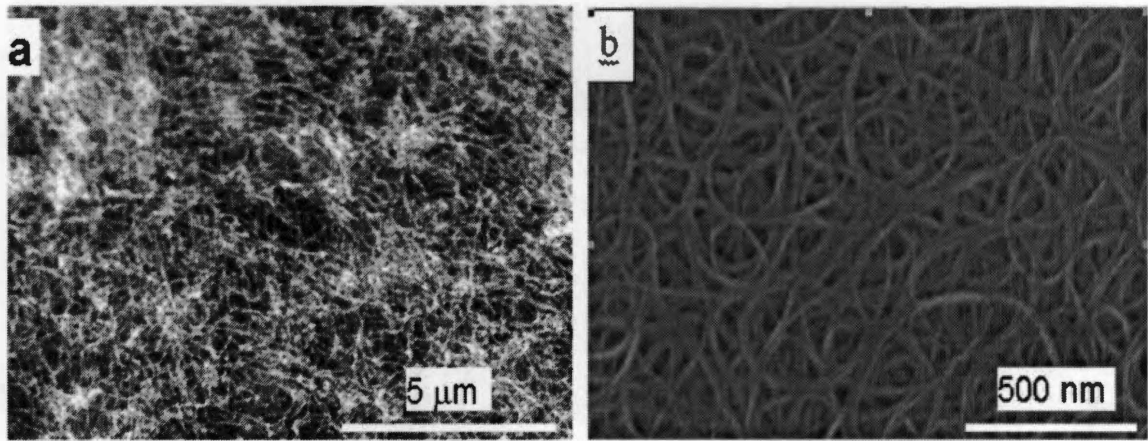


Figure 3.3: SEM of (a) raw SWNT (b) purified SWNT.

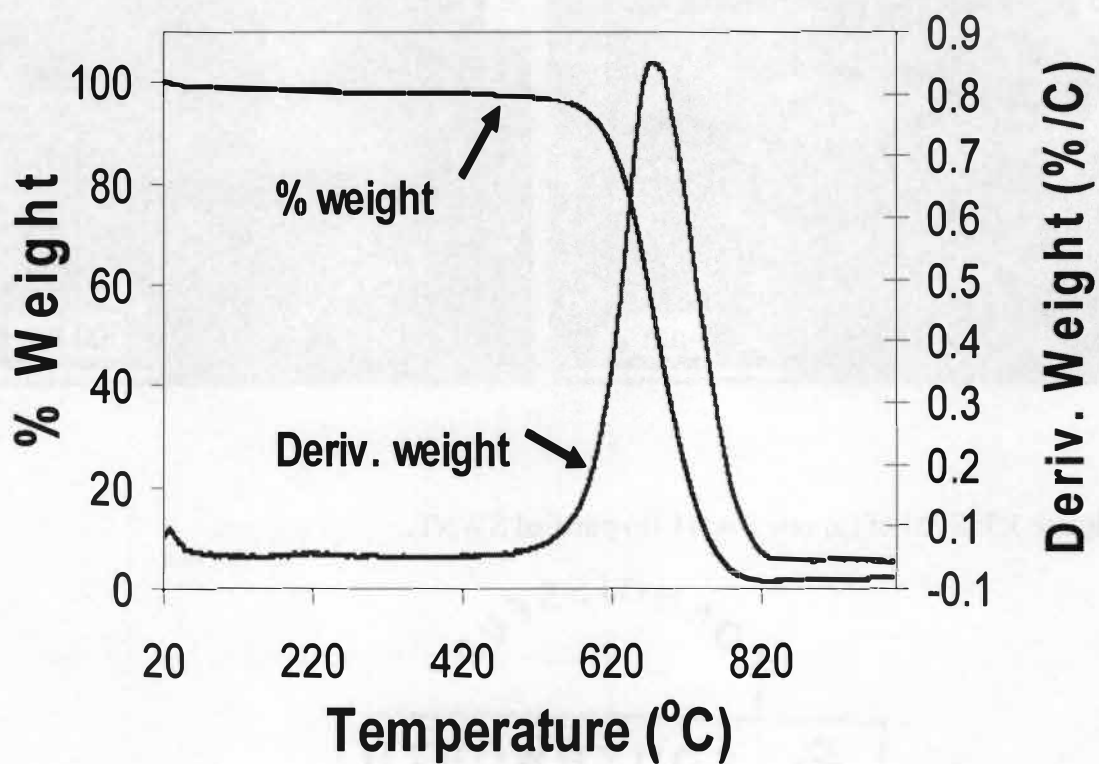


Figure 3.4: TGA of purified SWNT.

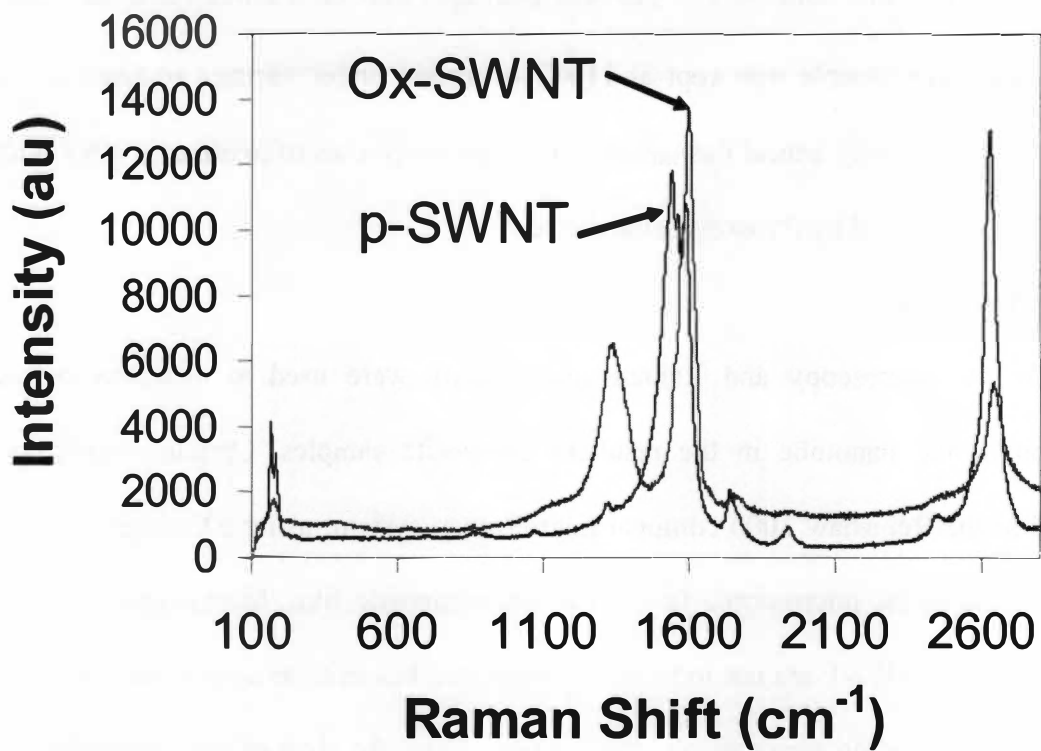


Figure 3.5: Raman Spectra of purified and oxidized SWNT.

additional minute. The solution (50 μL) was then spin cast on a silica substrate (2500 rpm, 60 sec). The sample was kept at 110°C overnight under vacuum to remove the solvent and to thermally anneal the sample. The nanocomposites of oxidized SWNT with polymer were prepared by the exact same method.

Optical Microscopy

Optical microscopy and Raman spectroscopy were used to characterize the dispersion of the nanotube in the resultant composite samples. Optical microscopy (attached to the Renishaw 1000 confocal microRaman system, using 5X objective) was used to visualize the microscopic features of the composite film. Microscopic analysis indicates that the SWNT are not individually dispersed but exist as aggregates, however the level of aggregation varies among the samples. Thus, the sizes of the aggregates are determined using image analysis software by SIMAGIS Research to quantify the average aggregate size in each composite sample.

Raman and FTIR Spectroscopy

Raman spectroscopy analysis was performed using a Renishaw 1000 with 632.8nm excitation wavelength at 25% energy (50X objective) and a laser spot size of 0.2 micron. FTIR spectra were collected by a FTS 6000 FTIR spectrometer by Bio-rad. The copolymer and the nanocomposites were analyzed as films on glass substrate. The FTIR spectra for polymer and nanocomposite films were collected as absorbance spectra using 256 scans at 2 cm^{-1} resolution.

3.2 Results and Discussion

A total of ten (10) composite samples were prepared according to the procedure described in experimental section. These include composites of the purified and oxidized

single walled nanotubes with PS, PSVPh10, PSVPh20, PSVPh40 and PVPh. In all cases, the SWNT loading is 1% by weight.

3.2.1 Optical Microscopy & Aggregate Size Analysis

The optical micrographs and the histograms obtained from aggregate size analysis of composites of PS, PSVPh10, PSVPh20, PSVPh40 and PVPh with purified and oxidized SWNT are shown in Figures 3.6, 3.7, 3.8, 3.9 and 3.10 respectively. Aggregates of nanotubes are visible in all nanocomposites, however their sizes vary. It is important to note that the composite preparation procedure was not optimized to break apart these aggregates. Large and irregularly shaped aggregates are visible in both composites of PS with similar aggregate size (Figures 3.6a and 3.6b). Large aggregates of nanotubes are also evident in both nanocomposites of PSVPh10 (Figures 3.7a and 3.7b) however their sizes are relatively smaller as compared to the composites of PS. The aggregate size reduces further as the polymer becomes more polar for the PSVPh20 nanocomposites with the aggregates exhibiting a roughly circular shape (Figures 3.8a and 3.8b). For the PSVPh40 (Figures 3.9a and 3.9b) nanocomposites, no further obvious decrease in aggregate size is observed. Also, initial observation reveals that the nanotube aggregate size appears to be smaller for the nanocomposites of the copolymers with the oxidized SWNT relative to the nanocomposites with the purified SWNT. The aggregate size of nanotube clusters in each composite sample is measured by Image analysis software and the results are given in Table 3.2. For each analysis all visible aggregates in the image are included in the analysis. For each aggregate, the maximum distance between two points on the aggregate edge is taken as the aggregate size. These measurements provide a

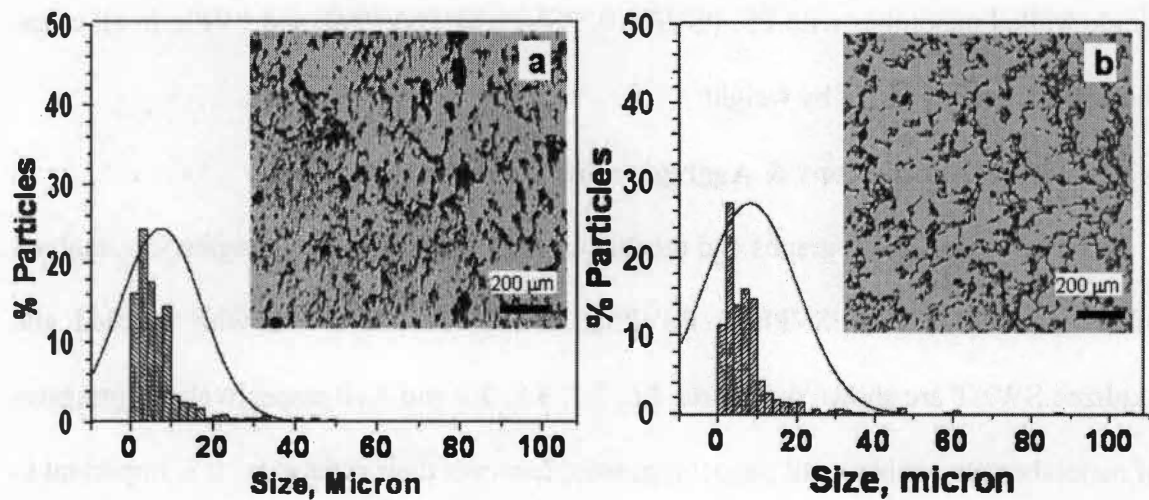


Figure 3.6: Optical Micrographs and histograms of the aggregates from image analysis of (a) PS+1%p-SWNT, (b) PS+1% ox-SWNT.

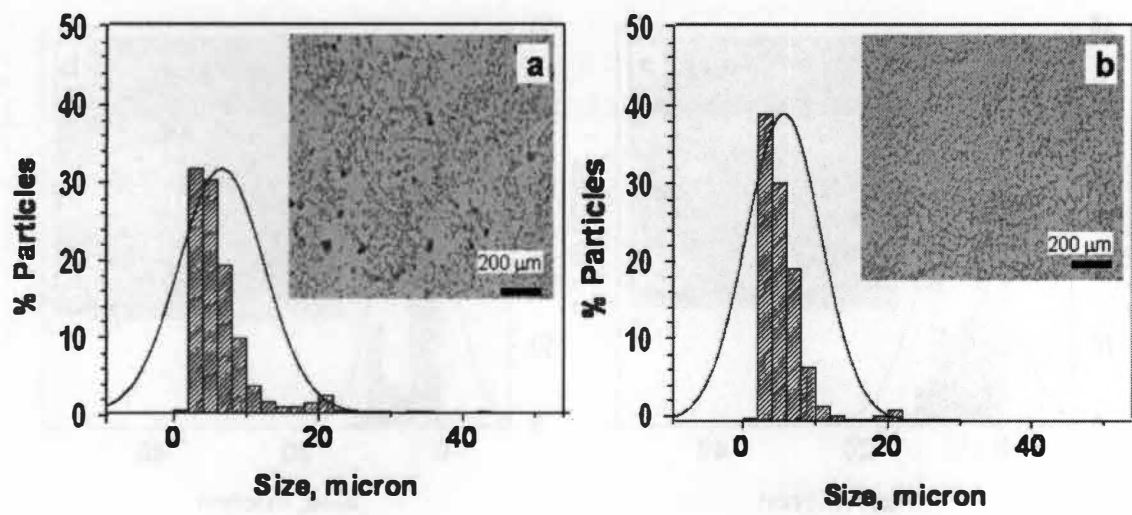


Figure 3.7: Optical Micrographs and histograms of the aggregates from image analysis of (a) PSVPh10+1%p-SWNT, (b) PSVPh10+1% ox-SWNT.

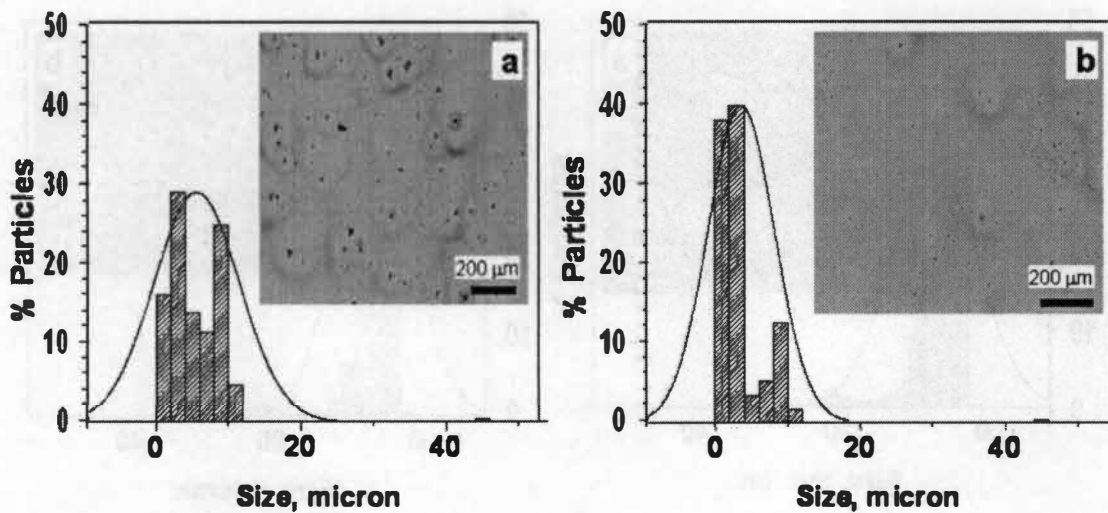


Figure 3.8: Optical Micrographs and histograms of the aggregates from image analysis of (a) PSVPh20+1%p-SWNT, (b) PSVPh20+1% ox-SWNT.

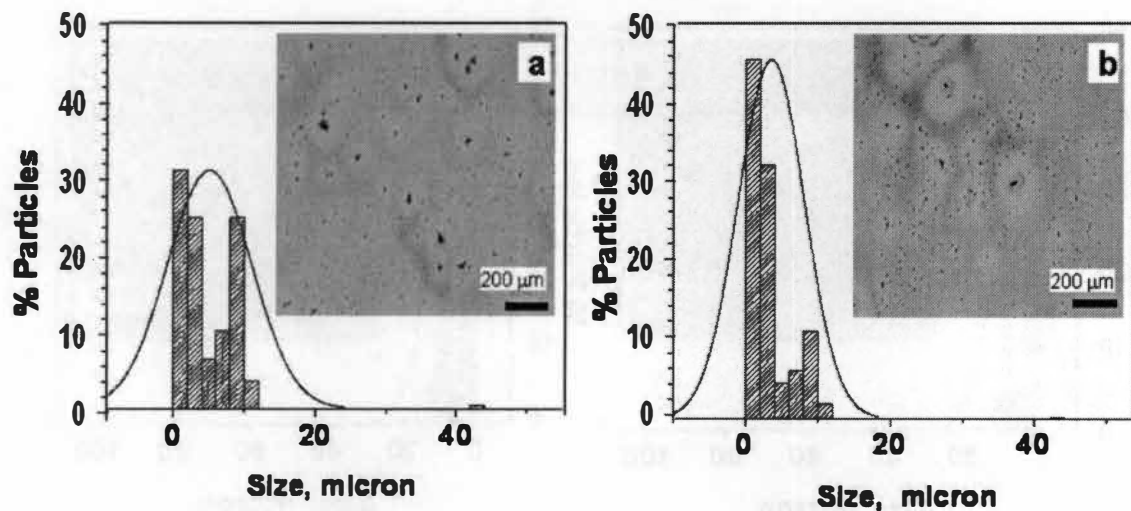


Figure 3.9: Optical Micrographs and histograms of the aggregates from image analysis of (a) PSVPh40+1%p-SWNT, (b) PSVPh40+1% ox-SWNT.

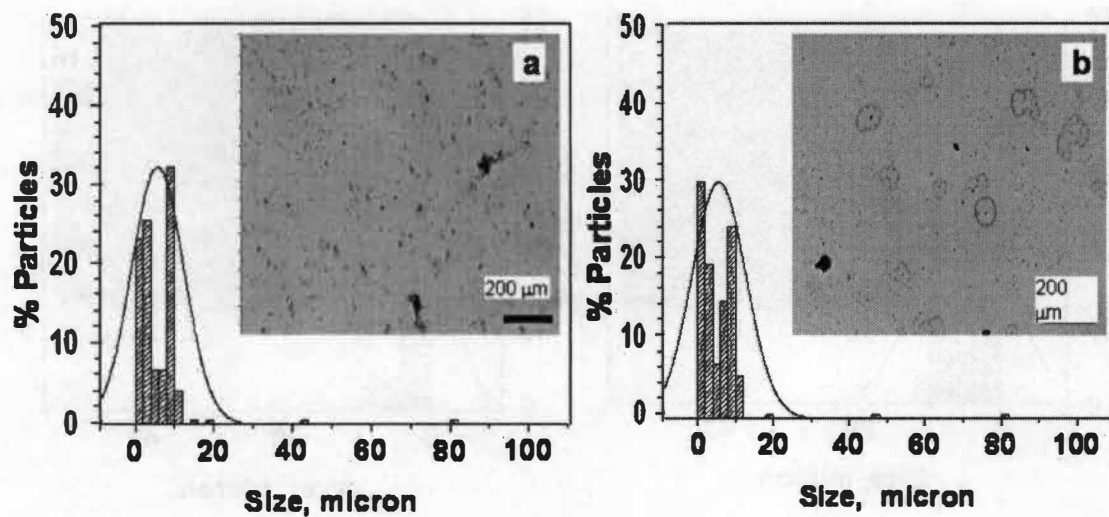


Figure 3.10: Optical Micrographs and histograms of the aggregates from image analysis of (a) PVPh+1%p-SWNT, (b) PVPh+1% ox-SWNT.

Table 3.2: Aggregate Size (weight average) in composites obtained by image analysis

	p-SWNT Avg. Size (μ)	Ox-SWNT Avg. Size (μ)
PS	7.5 ± 0.4	8.3 ± 0.5
PSVPh10	6.6 ± 0.1	5.6 ± 0.1
PSVPh20	5.6 ± 0.3	3.6 ± 0.2
PSVPh40	5.1 ± 0.4	3.5 ± 0.2
PVPh	5.7 ± 0.4	5.6 ± 0.5

distribution of aggregate sizes from which the average aggregate size is calculated. The average aggregate size is plotted in Figure 3.11 as a function of copolymer composition. The average aggregate size of the oxidized SWNT in PS is about $8 (\pm 0.5) \mu\text{m}$. The aggregate size decreases to about $5.6 (\pm 0.1) \mu\text{m}$ for the oxidized SWNT in the PSVPh10 copolymer. This drop in aggregate size suggests that the presence of vinyl phenol groups in the polymer chain breaks apart the oxidized SWNT aggregates into smaller clusters. A further decrease in aggregate size (to $\sim 3.6 (\pm 0.2) \mu\text{m}$) is observed as the copolymer becomes more polar in the PSVPh20 copolymer. The oxidized SWNT aggregate size stays about the same ca. $3.5 (\pm 0.2) \mu\text{m}$ as the copolymer adds more hydroxyl groups in the PSVPh40 copolymer and poly(vinyl phenol) polymer. The trend of the aggregate size of the oxidized SWNT in the composites clearly indicates that the introduction of the vinyl phenol groups to the copolymer chain provides the polymer chain the ability to break apart the oxidized SWNT aggregates. We interpret this observation as being due to the presence of improved interactions between the copolymer and the defect sites on the oxidized SWNT. Obviously, the interaction between the vinyl phenol groups and the defect sites on the SWNT is not possible in polystyrene and thus, results in the oxidized SWNT remaining as large aggregates in polystyrene.

Additionally, the average aggregate size of the composites with purified SWNT is always larger than those of the oxidized SWNT composites. This observation can be attributed to a smaller number of defect sites present on the purified SWNT, hence a lesser extent of interaction is possible between the vinyl phenol of the copolymer and the

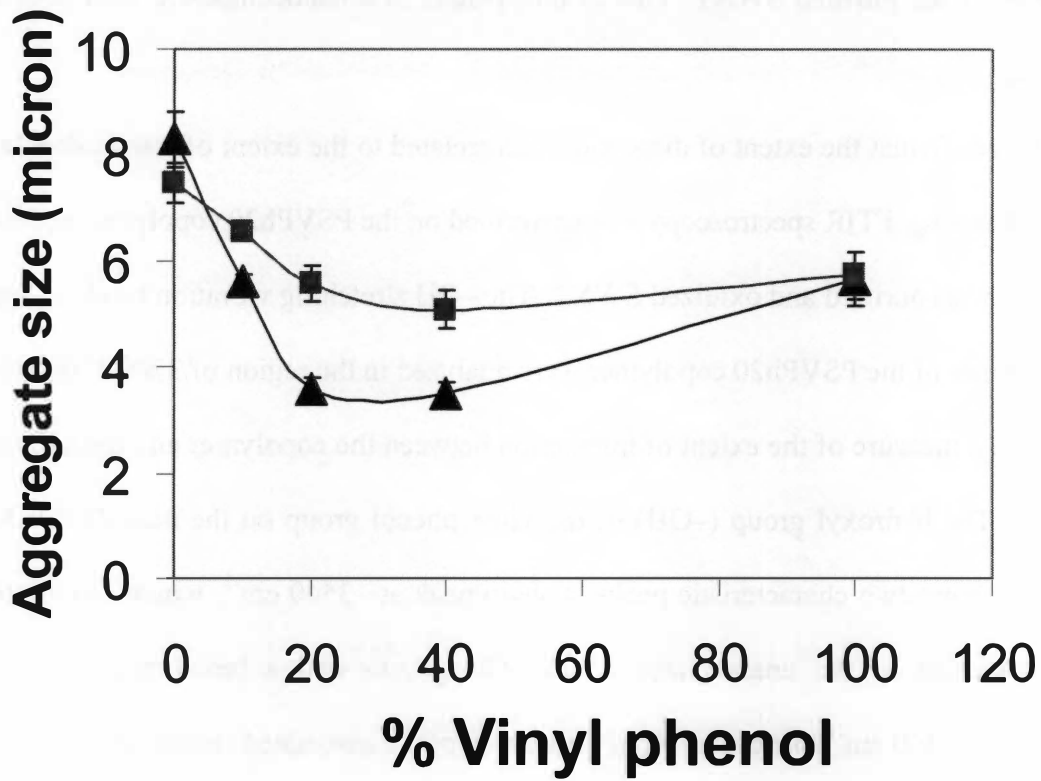


Figure 3.11: Average aggregate size of p-SWNT (■) and ox-SWNT (▲) in composite versus copolymer composition.

defect sites of the purified SWNT. This in turn results in a nanocomposite with poorer dispersion.

To verify that the extent of dispersion is correlated to the extent of intermolecular hydrogen bonding, FTIR spectroscopy was performed on the PSVPh20 copolymer and its composites with purified and oxidized SWNT. The –OH stretching vibration bands of the FTIR spectrum of the PSVPh20 copolymer were analyzed in the region of 3700-3100 cm^{-1} to provide a measure of the extent of interaction between the copolymer and the carbon nanotubes. The hydroxyl group (–OH) of the vinyl phenol group on the neat PSVPh20 copolymer shows two characteristic peaks, a sharp peak at $\sim 3540 \text{ cm}^{-1}$, which originates from the motion of the unassociated (free) –OH groups and a broad peak with a maximum at $\sim 3400 \text{ cm}^{-1}$ that comes from the motion of the associated (hydrogen bonded) –OH groups. The two peaks in the FTIR curve were deconvoluted using Peakfit v4.11 software. In the copolymer-nanotube nanocomposite systems, some of the hydroxyl groups of the PSVPh copolymer also interact with the oxygenated defect sites on the carbon nanotube via hydrogen bonding. Hence the peak in the FTIR curve of the nanocomposites that originates from the motion of the associated –OH groups in the polymer-nanotube composites is comprised of the motions of –OH groups that are associated with another –OH on the polymer chain, an interaction that we term intra-associated –OH groups, as well as the motions of –OH groups that are hydrogen bonded to the oxygenated functional groups of the nanotube, an interaction that we term inter-associated –OH groups. The area under the curve for each peak (free –OH, inter-, and intra-associated –OH) is considered a qualitative measure of its contribution to the motions of the copolymer in the composites, and thus provides a measure of the extent

the –OH moieties exist in each state. The details of FTIR analysis is given in Appendix A-1.

The FTIR spectra of PSVPh20 and its composites with purified and oxidized SWNT are shown in Figure 3.12. The area under the deconvoluted peaks for each of these curves as obtained by the Peakfit software is given in Table 3.3. The motion of the free –OH contributes approximately 11% of the total –OH peak area in the neat PSVPh20, whereas the associated –OH contributes 89%. In the presence of purified SWNT, the motion of the intra-associated –OH still contributes approximately 88% to the –OH peak in the FTIR curve, while the motion of the free –OH still contributes 11% and the motion of the inter-associated –OH provides only 1% of the total FTIR peak. This indicates that here is very little hydrogen bonding or other intermolecular interaction between the PSVPh20 copolymer and the purified nanotubes. This changes, however, for the PSVPh20 nanocomposite with oxidized SWNT. In this nanocomposite, the motion of the intra-associated –OH contributes 74% to the –OH peak in the FTIR curve, the free –OH contributes 9%, and the motion of the inter-associated –OH makes up 17% of the FTIR curve, providing spectroscopic evidence that the PSVPh20 copolymer forms significantly more intermolecular interaction to the oxidized SWNT than it does in to the purified SWNT. This extent of interaction also correlates very well with the observed dispersion of the SWNT in the polymer matrix.

3.2.2 Raman Spectroscopy

Raman spectroscopy has been used extensively to study SWNT, as SWNT possess unique features observed by Raman spectroscopy.¹⁰² Features at low frequency ($\sim 150\text{-}300\text{cm}^{-1}$) are known as radial breathing modes (RBM) and are related to

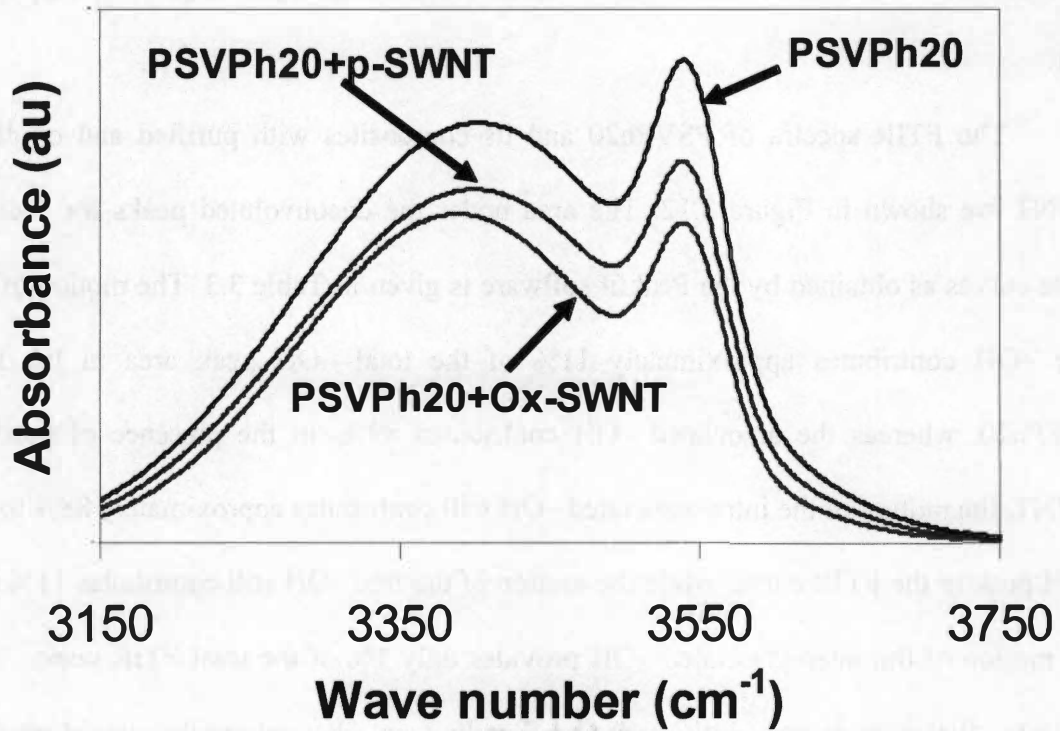


Figure 3.12: FTIR spectrum of PSVPh20, PSVPh20+1% ox-SWNT and PSVPh20+1% p-SWNT in the region of -OH stretching vibrations.

Table 3.3: Contribution of free and associated –OH in PSVPh20 and its composites

	Contribution of free and associated –OH (%)		
	Free –OH	Intra-associated - OH	Inter-associated – OH
PSVPh20	11	89	
PSVPh20+p-SWNT	11	88	1
PSVPh20+ox-SWNT	09	74	17

symmetric movements of all carbon atoms in the radial direction. The disorder-induced D-band is observed at $\sim 1350\text{cm}^{-1}$, while the tangential or G-band appears at around 1400-1600 cm^{-1} . The second-order overtone of the D-band, referred to as D* (or G'), appears at $\sim 2600\text{-}2700\text{cm}^{-1}$.¹⁰³

Among all the features of Raman spectroscopy of SWNT, the G-band is the most prominent, even in the regions where SWNT concentration is low. Hence, this band can be used to detect the presence of nanotubes in nanocomposite samples throughout the image on the length scale of the Raman beam size, whether or not optical microscopy indicates the presence of tubes in that region. The intensity of the G-band in a particular region of the nanocomposite can thus be used to measure the amount of SWNT present in a given area of the sample. The nanocomposite sample was thus mapped (beam size $\sim 2\ \mu\text{m}$) with Raman spectroscopy to investigate the state of SWNT dispersion in the nanocomposite. The variation of G-band intensity in different regions of the nanocomposite sample thus provides quantitative information regarding the SWNT dispersion in the sample. Complementarily, the D* band peak shift in the nanocomposite relative to the D* peak of the pure SWNT can be analyzed to provide an indication of interaction between the nanotube and polymer.¹⁰³

Nanotube Dispersion using Raman Spectroscopy

Figures 3.13 and 3.14 show the optical micrograph, color coded map of the integrated area under the G-band, and the integrated area under the the G-band for PSVPh20 composites with purified and oxidized SWNT, respectively. The variation in the area of the G-band clearly indicates that the quality of dispersion of the oxidized

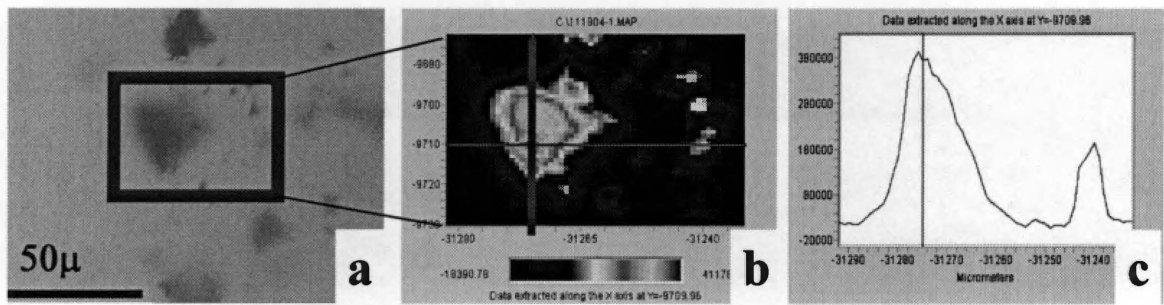


Figure 3.13: (a) Optical micrographs of PSVPh20+1%pSWNT on glass substrate (b) Color coded map of the integrated area under the G-band for this optical micrograph. The dark areas corresponds to low SWNT content whereas the Red area corresponds to highest SWNT content (c) The integrated area under the G-band along the vertical line shown in (b).

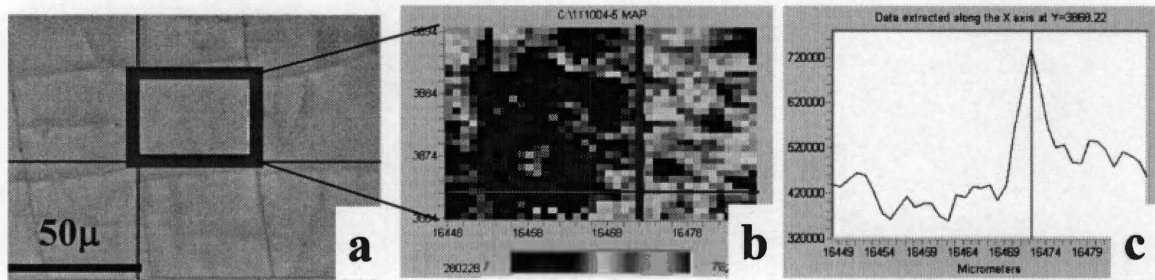


Figure 3.14: (a) Optical micrographs of PSVPh20+1% ox-SWNT on a glass substrate (b) The color coded map of the integrated area under the G-band for this optical micrograph. The dark areas correspond to low SWNT content whereas the Red area corresponds to the highest SWNT content (c) The integrated area under the G-band along the vertical line shown in (b)

SWNT is significantly improved relative to the nanocomposites with purified SWNT. To quantify the SWNT dispersion in the polymer matrix, the G-band intensity is considered for all the composite samples. The G-band intensity is obtained for the clear and aggregate regions of a given image and averaged. The ratio of the average G-band intensity in the clear regions (I_G^{clear}) to the average G-band intensity in the aggregates (I_G^{agg}) provides a measure of the quality of the dispersion of the SWNT in a given composite sample. In cases where the SWNT is well dispersed in a polymer matrix, the ratio $I_G^{\text{clear}}/I_G^{\text{agg}}$ will approach 1, while in a composite sample where the SWNT is poorly dispersed, the G-band intensity in the aggregates is expected to be significantly higher than the G-band intensity in the clear regions, thus, the ratio $I_G^{\text{clear}}/I_G^{\text{agg}}$ will approach zero in these samples.

$I_G^{\text{clear}}/I_G^{\text{agg}}$ is found to be very low for all p-SWNT composite samples. However, the difference in intensity of the G-band for the clear and aggregate regions is significantly smaller for the composites of oxidized SWNT. The ratio of the G-band intensity in the clear regions to that in the aggregate region ($I_G^{\text{clear}}/I_G^{\text{agg}}$) is plotted versus percent vinyl phenol in the copolymer matrix in Figure 3.15. This data quantifies the dispersion of the SWNT in the various copolymer matrices and shows that they are significantly better dispersed in the PSVPh20 and ox-SWNT composite than in the PSVPh20 and p-SWNT composite. The enhanced dispersion of Ox-SWNT in PSVPh20 matrix is attributed to the presence of specific interactions between the two components. Figure 3.15 also shows the effect of copolymer composition on the dispersion of the SWNT in the polymer matrix as measured by the ratio $I_G^{\text{clear}}/I_G^{\text{agg}}$. The value of $I_G^{\text{clear}}/I_G^{\text{agg}}$ is

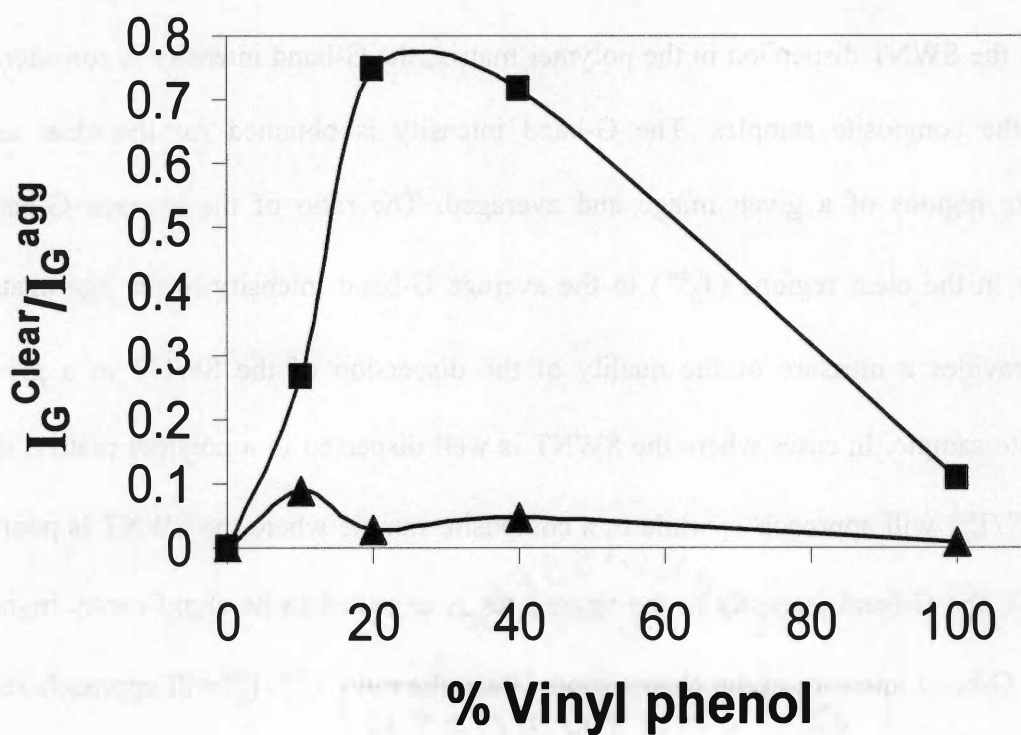


Figure 3.15: Ratio of G-band intensity in the clear region to the G-band intensity in the aggregate for p-SWNT composites (\blacktriangle) and ox-SWNT composites (\blacksquare) as a function % vinyl phenol in the copolymer matrix.

close to zero for the nanocomposite of polystyrene with ox-SWNT and increases to 0.26 for the nanocomposite of PSVPh10 and ox-SWNT. Increasing further the amount of vinyl phenol in the polymer chain to 20% creates a nanocomposite where this ratio increases to 0.75. Upon further increasing the vinyl phenol content to 40% (PSVPh40), the value of $I_G^{\text{clear}}/I_G^{\text{agg}}$ does not change appreciably but goes down to 0.15 for the PVPh and ox-SWNT nanocomposite. A trend is clearly emerging for the oxidized SWNT composites; increasing vinyl phenol content from 0% to 20% improves dispersion, however higher amount of vinyl phenol shows no further improvement in dispersion. This trend was not observed for the composites of purified SWNT. For all the composites of purified SWNT, the value of the ratio $I_G^{\text{clear}}/I_G^{\text{agg}}$ remains around 0.1, indicating poor dispersion in all of these composites.

Interaction between the Nanotube and Copolymer by Raman Spectroscopy

The optical microscopy results clearly show smaller aggregate sizes for the ox-SWNT in PSVPh copolymer relative to the nanocomposites with p-SWNT and FTIR indicates that this dispersion correlates very well with the extent of intermolecular interaction between the polymer matrix and nanotube. To further investigate this correlation, Raman spectroscopy can be used to examine the interactions between the polymer and nanotubes for all composites.

The shift of the D* band peak position in a polymer nanocomposite relative to that of the pure nanotube is an indicator of the interaction between a nanotube and polymer.⁴¹⁻⁴⁴ The D* position for the p-SWNT and ox-SWNT in the nanocomposites are given in Table 3.4 and shown in Figure 3.16 as a function of copolymer composition. The composites with

Table 3.4: D* peak position shift in composite

	P-SWNT (cm ⁻¹)	Ox-SWNT (cm ⁻¹)
	2628.3	2645.1
PS	2634.8 (+6.5)	2640.0 (-5.1)
PSVPh10	2638.5 (+10.2)	2637.7 (-7.4)
PSVPh20	2637.7 (+9.4)	2634.8 (-10.3)
PSVPh40	2638.5 (+10.2)	2639.0 (-6.1)
PVPh	2638.5 (+10.2)	2637.7 (-7.4)

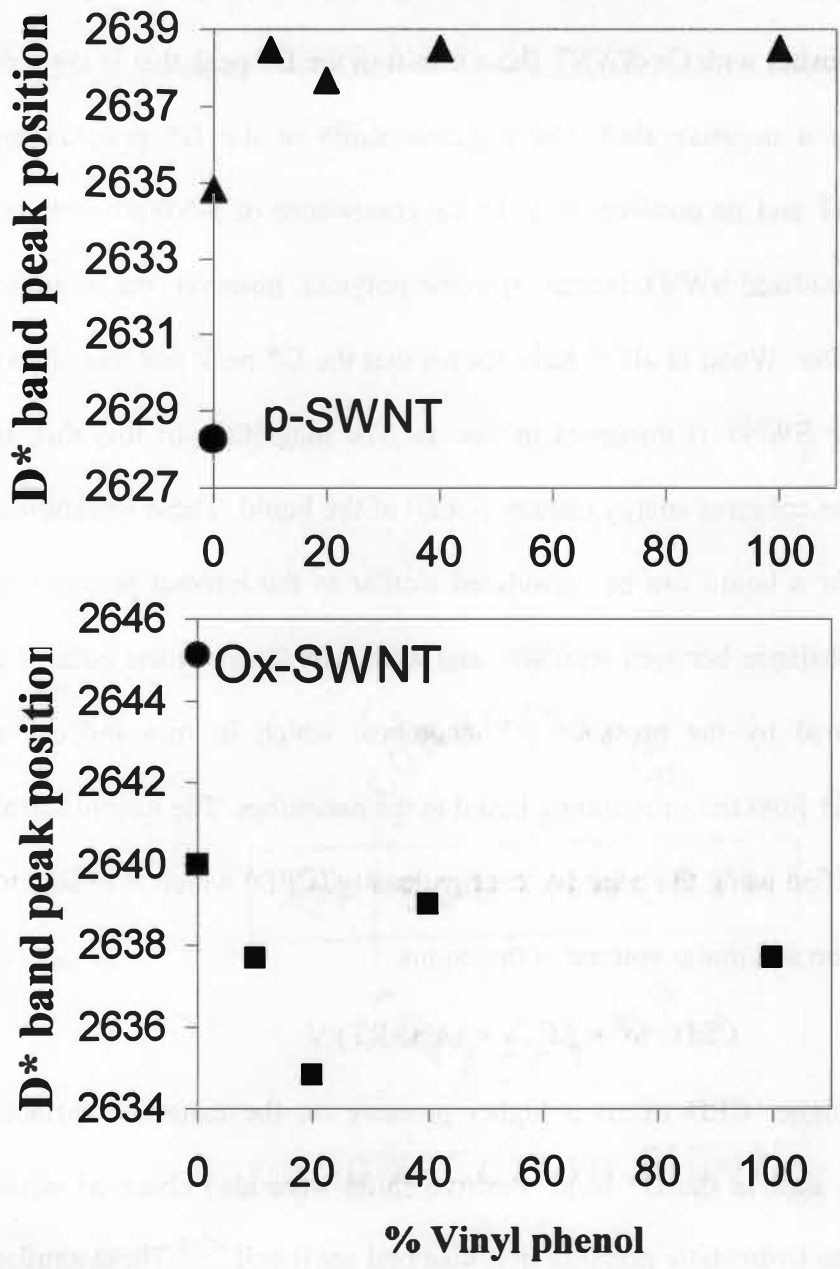


Figure 3.16: D* band peak position for p-SWNT (▲) and Ox-SWNT (■) in nanocomposites as a function of the composition of the copolymer matrix. The circle (●) indicates the D* band peak position for the purified or oxidized SWNT in air.

p-SWNT show a shift in the D* peak that is towards higher wave number or a positive shift, whereas the composites with Ox-SWNT show a shift in the D* peak that is towards lower wave number or a negative shift. The negative shifts in the D* position for composites of ox-SWNT and its positive shifts in the composites of p-SWNT indicate that both purified and oxidized SWNT interact with the polymer, however, the origin of this interaction must differ. Wood et al^{42,43} have shown that the D* peak position shows positive shifts when the SWNT is dispersed in liquids. The magnitude of this shift is found to be related to the cohesive energy density (CED) of the liquid. These researchers argued that the CED for a liquid can be considered similar to the internal pressure of liquids. There exists a balance between repulsive and attractive forces in the bulk of a liquid which is disturbed by the presence of nanotubes, which in turn induces a hydrostatic stress transfer from the surrounding liquid to the nanotubes. The magnitude of this stress can be quantified using the cohesive energy density (CED) which is related to the energy of vaporization and molar volume of the liquid.

$$CED = \delta^2 = \Delta E_v/V = (\Delta H_v - RT)/V$$

A liquid with higher CED exerts a higher pressure on the nanotube surface, causing higher positive shift in the D* band. Positive shifts were also observed when SWNT were subjected to hydrostatic pressure in a diamond anvil cell.^{42,43} These similar trends of D* peak shifts suggests that the SWNT responds similarly to molecular (SWNT dispersed in liquid) and macroscopic (hydrostatic pressure by diamond anvil cell) pressure. A positive D* band peak shift was also observed for SWNT embedded in polycarbonate matrix.¹⁰⁶ Hence, the positive shift in D* peak position can be interpreted

as a consequence of the internal pressure experienced by SWNT in the presence of a surrounding second phase.

Cooper et al⁴⁴ studied composites of epoxy with SWNT and MWNT under tensile deformation using a diamond anvil cell and monitored the D* band peak position. The D* band shifted to lower wave number under tensile stress and this was attributed to stress transfer to nanotubes. Ajayan⁴¹ studied the Raman spectroscopy of a SWNT-epoxy composite under compression and tension. No shifts in D* band peak position were observed under compression, however, negative shifts were observed under tension. These negative shifts under tension are interpreted to be due to reduced radial stress on the nanotubes, which is possibly due to debundling of the nanotubes. The debundling in turn causes an increase in inter-tube spacing, which results in a change in the stiffness for the out-of-plane vibrations.⁴¹

In our case, positive shifts in D* band peak position are observed in the nanocomposites of p-SWNT and can be interpreted in terms of the internal pressure on the SWNT in the composite due to the presence of the neighboring polymer. Due to this internal pressure from the polymer, the inter-tube spacing decreases, which stiffens the bond between SWNTs. This observation is consistent with Wood et al,^{42,43} where a macroscopic pressure on nanotubes causes a positive shift. However, in the case of our oxidized SWNT and polymer nanocomposites, negative shifts in the D* band are observed. In our composite system of ox-SWNT with polymer, the negative shifts indicate a reduction in radial stress on the nanotubes. This reduced radial stress correlates to a decrease in bundle size of SWNT (i.e. improvement of dispersion), which is a result of the enhanced interaction between the nanotube and polymer containing vinyl phenol.

It is also interesting to note the magnitude of the D* shifts in the composites. For the p-SWNT composites, the shift is 6.5 cm⁻¹ for polystyrene. The magnitude of the shift is higher for the PSVPh copolymers with values ranging from 9.4 cm⁻¹ (for PSVPh20 composite) to 10.2 cm⁻¹. Hence the difference in D* peak shifts among PSVPh copolymer composites is less than 1 cm⁻¹, which implies that the pressure applied by these different copolymers on the p-SWNT is similar in magnitude. For the ox-SWNT composites, the magnitude of the shifts among the PSVPh copolymers is between 4-10 cm⁻¹ with PSVPh20 showing the maximum shift (10.3 cm⁻¹). The greater variation in D* band peak position in the composites of ox-SWNT with the PSVPh copolymer suggests that the interaction of the ox-SWNT with the various copolymers varies significantly in these systems.

The magnitude of the shift in the D* peak corresponds to the amount of interaction between the polymer and the nanotube,⁴² i.e., a greater amount of interaction between polymer and nanotube is reflected by a larger shift in the D* band peak position. The degree of interaction between polymer and the oxidized carbon nanotube increases as the polymer changes from pure polystyrene to PSVPh10, as signified by a negative shift of 2.3 cm⁻¹. Clearly, incorporation of vinyl phenol groups in the polymer chain enhances the amount of interaction between the two components. The interaction between oxidized SWNT and polymer increases further when PSVPh20 was utilized to prepare the composite, where a negative shift of 10.3 cm⁻¹ is observed. For PSVPh40 and PVPh polymers, negative shifts of 6.1 and 7.4 cm⁻¹ are observed, respectively. This trend of increasing interaction between oxidized SWNT and polymers correlates well with the dispersion as measured by the ratio $I_G^{\text{clear}}/I_G^{\text{agg}}$. This correlation of trends between

spectroscopic evidence of specific interactions between the carbon nanotubes and the polymer matrix (D^* band shifts) and the dispersion of the nanotube in the polymer matrix (I_G^{clear}/I_G^{agg}) strongly suggests that enhanced molecular level interaction is responsible for the improved nanotube dispersion in the polymer matrix. Moreover, the enhanced interaction, as well as dispersion, is optimum for the PSVPh20 copolymer.

This optimization of the dispersion and interaction in the nanocomposite with copolymer composition can be interpreted in terms of the accessibility of the hydroxyl groups on the copolymer to participate in intermolecular specific interactions and the influence of the copolymer composition on this accessibility.⁸¹⁻⁸⁴ PSVPh is a random copolymer with vinyl phenol groups distributed relatively evenly along the polymer backbone. Thus, the variation in copolymer composition controls the average distance between two vinyl phenol moieties. Hence, by increasing the vinyl phenol content in the copolymer backbone, the average separation between moieties decreases. At high vinyl phenol content, the decreased spacing between vinyl phenol groups enables the formation of intramolecular hydrogen bonding, which decreases the number of hydroxyl groups available to form intermolecular hydrogen bonds. The formation of hydrogen bonds (intra- or intermolecular) also limits the rotational freedom of neighboring functional groups on the polymer chain. Thus, the accessibility of these neighboring functional groups to form intermolecular hydrogen bonds, i.e. access and orient correctly to the defect sites on nanotubes to form a hydrogen bond, is limited when there exist many hydroxyl groups on the copolymer chain. Conversely, at low vinyl phenol content, there exist insufficient interacting groups on the polymer chain to create optimal interactions. Therefore, there must exist an optimum vinyl phenol content in the polymer chain, where

the accessibility of the hydroxyl groups to form intermolecular hydrogen bonds is maximum. Our results indicate that this optimal composition of the styrene-vinyl phenol copolymer in these nanocomposites is 20% vinyl phenol.

3.3 Conclusions

A scheme to control the dispersion of a SWNT in a polymer matrix by systematically changing the polymer's ability to interact with the nanotube is presented. SWNT nanocomposites of a copolymer of styrene and vinyl phenol with varying amount of vinyl phenol are prepared using purified and oxidized SWNT. Optical microscopy and Raman spectroscopy results clearly indicate that the SWNT is optimally dispersed in the copolymer with 20% vinyl phenol when the SWNT is oxidized. Poor dispersion was found for the nanocomposites of the copolymers with purified SWNT. FTIR analysis indicates that the oxidized SWNT forms significantly more intermolecular interactions with PSVPh20 than the purified SWNT, which correlates very well to the dispersion results. Moreover, the D* peak position in the Raman spectra of the SWNT in each nanocomposite indicates an interaction between the copolymer and SWNT. Analyses of these shifts indicate that the oxidized nanotubes interact more readily and strongly with the styrene-vinyl phenol copolymers than the purified nanotubes. This data also show that the copolymer with 20% vinyl phenol interacts the most with the SWNT. Thus, the dispersion of a SWNT in a polymer matrix can be readily and reproducibly controlled and optimized by varying the extent of specific interactions between the polymer and the carbon nanotube, which in turn can be readily realized by modifying the composition of the copolymeric nanocomposite matrix.

Chapter 4

Polymer Nanotube Nanocomposites: Correlating Intermolecular Interaction to Ultimate Properties

In this chapter, the results on mechanical and electrical properties of single wall carbon nanotubes (SWNT) and multiwalled carbon nanotubes (MWNT) composites are presented. The copolymers used in this study contain styrene and vinyl phenol with varying vinyl phenol content. The copolymers were synthesized according to the procedure described in Chapter 3. The copolymers containing 10, 20, 30 and 40% vinyl phenol are utilized in this study and are designated as PSVPh10, PSVPh20, PSVPh30 and PSVPh40, respectively. The exact copolymer composition, molecular weights and polydispersity are given in Table 4.1. The mechanical and electrical properties of the composites are determined by tensile tests and electrical conductivity measurements respectively. The interaction between nanotubes and the polymer is examined by Fourier transform infra-red (FTIR) spectroscopy.

4.1 Experimental

Materials

SWNT prepared by high pressure disproportionation reaction of carbon monoxide, (HiPCO) (< 1% metal impurities) are received from Carbon Nanotechnologies, Inc. and used without further treatment. MWNT (prepared by chemical vapor deposition, CVD, containing 2.5% metal impurities) are obtained from

Table 4.1: Composition and molecular weight of polymers prepared for chapter 4

	%Vinyl phenol	%Vinyl phenol actual*	Before Hydrolysis	After Hydrolysis	
			Mn ** (g/mol)	Mn ** (g/mol)	PDI
PS	0	0		105,840	1.6
PSVPh10	10	13.2	129,000	118,000	1.8
PSVPh20	20	19.0	116,000	108,000	1.9
PSVPh30	30	32.5		105,000	2.4
PSVPh40	40	42.0	123,000	116,900	2.2

* Determined by NMR

** Measured by GPC

Iljin Nanotech, Co. (Korea) and used as received. The solvent, *N,N*-dimethyl formamide (DMF) is obtained from Aldrich and received without any further treatment.

Composite preparation

12.5 mg of SWNT was dispersed in 100 ml of DMF by sonication in a sonic bath (Branson 3510, 40 kHz) for 24 hours. 237.5 mg of polymer was subsequently added to the SWNT/DMF dispersion and stirred at 70°C until sufficient amount of solvent evaporated to reduce the volume of the dispersion to 25 ml. The homogenous dispersion of the polymer and nanotubes was assisted by using a homogenizer (Bio Homogenizer by ESGE) for 5-10 minutes. The Polymer/SWNT/DMF dispersion was then cast on a hot glass substrate (~ 60-65°C). After solvent evaporation, the composite film was peeled off the glass substrate and further dried under vacuum at 90 °C for one day to ensure complete solvent removal. The MWNT composites were prepared using the same procedure. All composite samples contain 5% nanotubes by weight.

Characterization

Tensile tests were performed on an RSA III by Rheometric Scientific, where tensile strength, tensile modulus and strain were obtained from these measurements. The gauge length and crosshead speed for the tests were 10 mm and 0.05 mm/s, respectively. Ten strips (2 mm wide, 25 microns thick) of polymers and composite films were tested in each sample. The results for each sample were averaged, normalized to the tensile properties of the pure copolymer and plotted as a function of the copolymer composition. Tensile results for each copolymer and its composite were normalized to the tensile properties of the pure copolymer in order to eliminate molecular weight and composition effects. Electrical conductivity was measured using the four-probe method.

FTIR spectra were collected by a Spectrum One FTIR spectrometer by Perkin Elmer. SWNTs were mixed with KBr powder and compressed as pellets for data collection. The spectrum was collected against KBr background. The copolymer and the nanocomposites were analyzed as films and the spectra were collected against air background. The FTIR spectra for polymer and nanocomposite films were collected as absorbance spectra using 64 scans at 2 cm^{-1} resolution. The FTIR spectrum of SWNT is given in Figure 4.1. The peak at 1630 cm^{-1} in the FTIR spectrum indicates the presence of significant number of carbonyl groups in the as received purified SWNTs.

4.2 Results

4.2.1 Tensile Test

The tensile test results, given in Table 4.2, and the normalized tensile test results plotted in Figure 4.2 and 4.3 show that for both, MWNTs and SWNTs, the maximum improvement in the composite tensile properties are observed for the 20% vinyl phenol containing samples. In general, tensile strength of the PSVPh10, PSVPh20, and PSVPh30 SWNT composites showed enhancement, while the nanocomposites of PS and PSVPh40 suffered a loss in strength. It is clear from Figure 4.2 that the tensile strength of the composite increases as the PS is modified to PSVPh10 by incorporation of $-\text{OH}$ groups that can interact with functional groups on the carbon nanotube, and this interaction increases further as the copolymer is modified to include 20% hydroxyl groups. This interaction, however, decreases as further hydroxyl groups are incorporated in the polymer chain (PSVPh30 and PSVPh40). The trend for dependence of the tensile modulus and strain to failure on the copolymer composition is similar to that of the

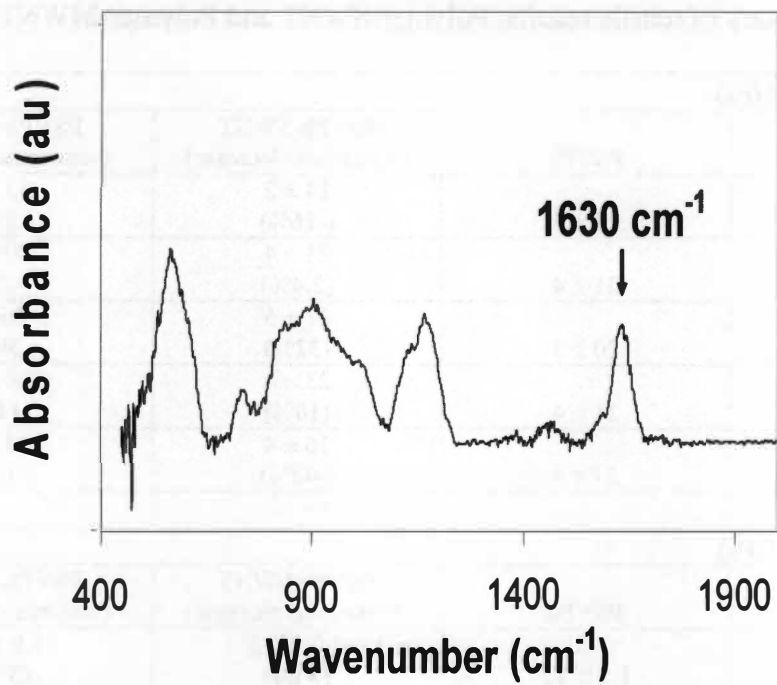


Figure 4.1: FTIR spectrum of SWNT

Table 4.2: Summary of tensile results: Polymer-SWNT and Polymer-MWNT composites

Tensile Strength (MPa)			
%Vinyl phenol	PSVPh	PSVPh-SWNT (%increase/decrease)	PSVPh-MWNT (%increase/decrease)
0	16 ± 4	14 ± 2 (-16%)	12 ± 2 (-23%)
10	21 ± 4	21 ± 4 (2.4%)	20 ± 8 (-2%)
20	20 ± 3	27 ± 5 (32%)	26 ± 6 (30%)
30	21 ± 4	23 ± 4 (10%)	24 ± 8 (11%)
40	27 ± 4	16 ± 4 (-42%)	24 ± 3 (-10%)
Tensile Modulus (GPa)			
%Vinyl phenol	PSVPh	PSVPh-SWNT (%increase/decrease)	PSVPh-MWNT (%increase/decrease)
0	1.5 ± 0.3	2.0 ± 0.2 (34%)	1.9 ± 0.2 (33%)
10	1.7 ± 0.3	2.6 ± 0.4 (57%)	1.9 ± 0.4 (16%)
20	1.6 ± 0.3	2.9 ± 0.3 (84%)	2.2 ± 0.2 (39%)
30	1.9 ± 0.3	2.8 ± 0.4 (47%)	2.7 ± 0.4 (43%)
40	2.1 ± 0.2	2.0 ± 0.5 (-2.8%)	2.7 ± 0.3 (32%)
Strain to Failure (%)			
%Vinyl phenol	PSVPh	PSVPh-SWNT (%increase/decrease)	PSVPh-MWNT (%increase/decrease)
0	1.5 ± 0.4	0.8 ± 0.2 (-44%)	0.7 ± 0.2 (-54%)
10	1.6 ± 0.3	0.9 ± 0.2 (-42%)	1.2 ± 0.3 (-27%)
20	1.3 ± 0.2	1.2 ± 0.2 (-6%)	1.4 ± 0.4 (6%)
30	1.2 ± 0.1	0.9 ± 0.2 (-25%)	1.0 ± 0.3 (-20%)
40	1.5 ± 0.1	0.7 ± 0.1 (-54%)	1.0 ± 0.1 (-36%)

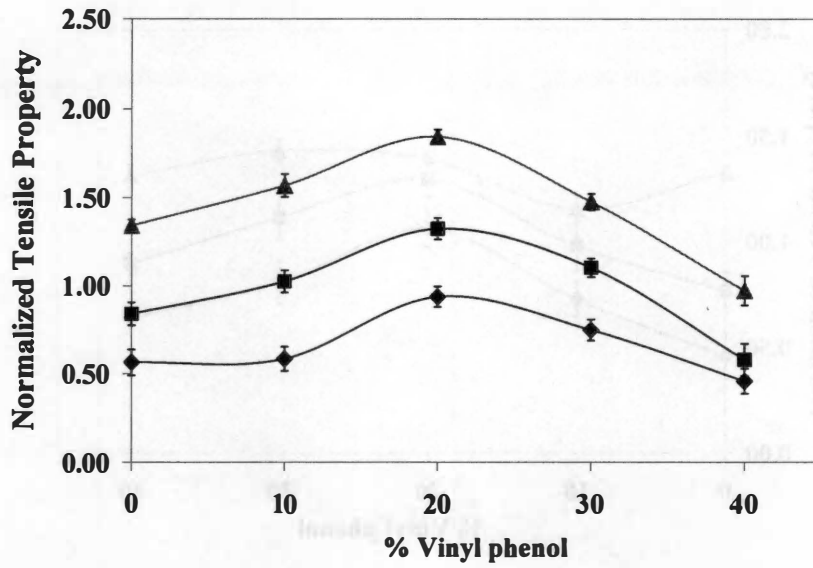


Figure 4.2: Normalized tensile strength (■), tensile modulus (▲) and strain to failure (◆) versus % vinyl phenol for PSVPh-SWNT composites

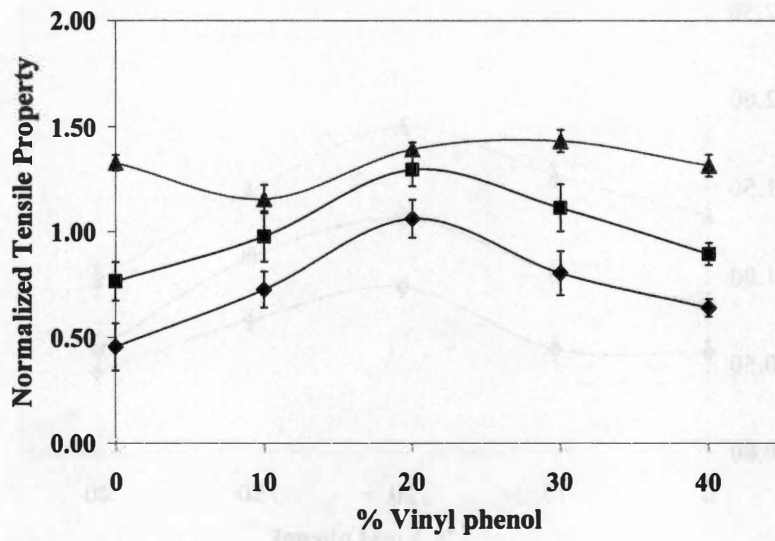


Figure 4.3: Normalized tensile strength (■), tensile modulus (▲) and strain to failure (◆) versus % vinyl phenol for PSVPh-MWNT composites.

tensile strength, however, the strain to failure decreased for all SWNT composites as compared to that of the pure copolymer. The tensile strength and strain to failure of the MWNT nanocomposites exhibited similar trends to the copolymer-SWNT composites, whereas no clear trend for the tensile modulus was observed.

4.2.2 Electrical Conductivity of Nanocomposites

The dc electrical conductivity of the nanocomposites for both SWNT and MWNT composites was also highest for the 20% vinyl phenol sample, as shown in Figure 4.4. The electrical conductivity of a polymer-carbon nanotubes composite depends on a number of factors including nanotube loading, nanotube length, as well as their dispersion and exfoliation state. A higher value of electrical conductivity corresponds to more well dispersed nanotubes in the polymer matrix,¹⁰⁴ provided all other variables remain unchanged. Thus, based on the electrical conductivity of these samples, we conclude that among the polymer samples studied, the PSVPh20 nanocomposite attained the best dispersion of the SWNT and MWNT.

4.2.3 FTIR Spectra of the Nanocomposites

FTIR spectra of the PSVPh copolymers in the hydroxyl stretching region (~ 3200 - 3600 cm^{-1}) and their composites with SWNT are plotted in Figure 4.5. All spectra indicate that the hydroxyl group ($-\text{OH}$) of vinyl phenol exists as unassociated $-\text{OH}$ groups ($\sim 3540 \text{ cm}^{-1}$) and associated (hydrogen bonded) $-\text{OH}$ groups ($\sim 3400 \text{ cm}^{-1}$) in all systems.

In these polymer-nanotube nanocomposites, some of the hydroxyl groups of PSVPh copolymer can interact with the oxygenated defect sites on the carbon nanotube via hydrogen bonding.^{81,82} Hence, the associated $-\text{OH}$ groups in the polymer-nanotube

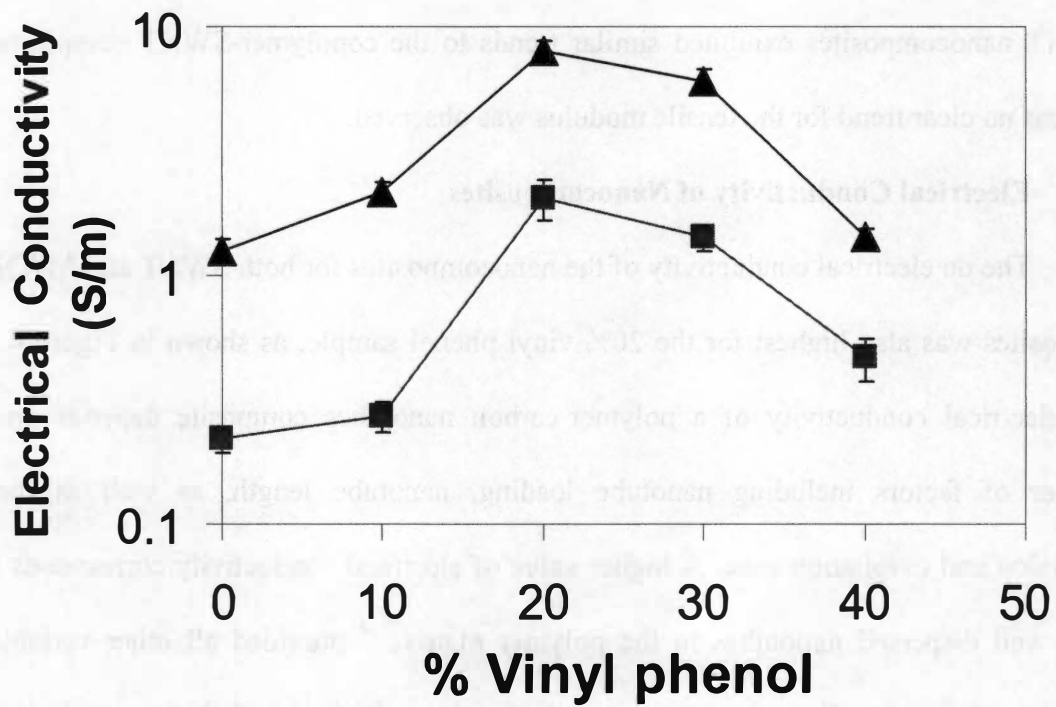


Figure 4.4: Electrical conductivity of polymer composites as a function of polymer composition for SWNT composites (\blacktriangle) and MWNT composites (\blacksquare).

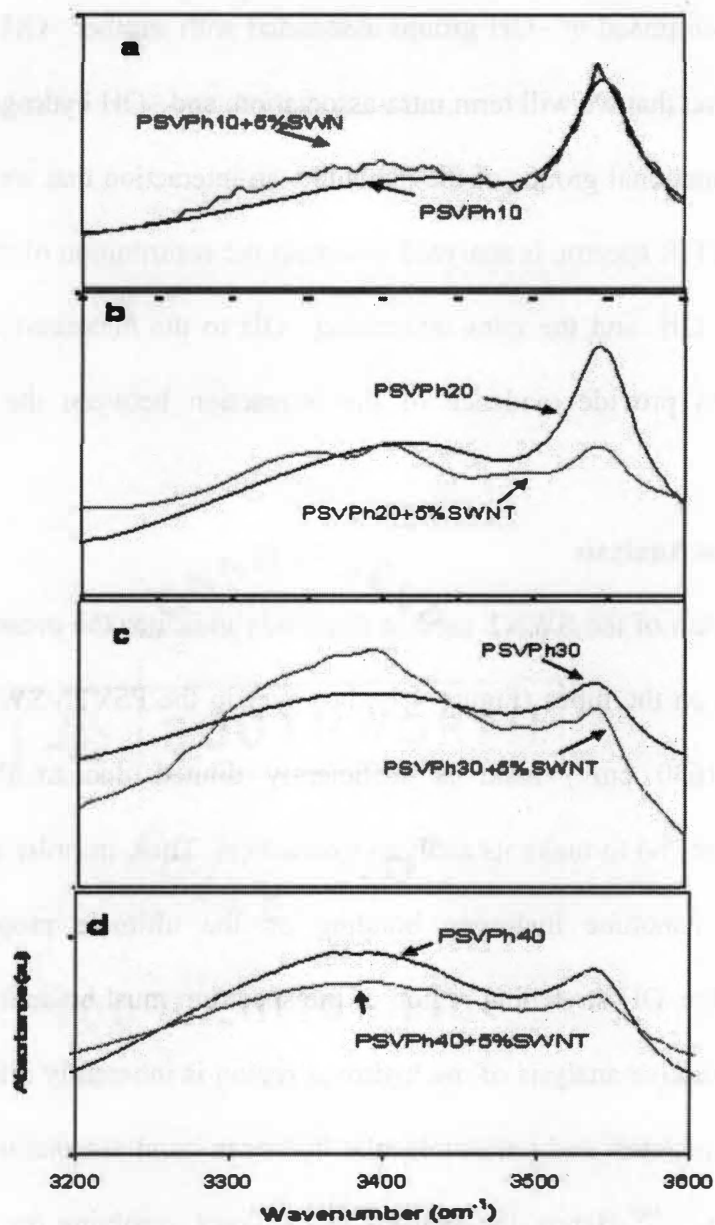


Figure 4.5: FTIR spectra of pure copolymers and their composites with SWNT (a) PSVPh10 & PSVPh10+5%SWNT, (b) PSVPh20 & PSVPh20+5%SWNT, (c) PSVPh30 & PSVPh30+5%SWNT and (d) PSVPh40 & PSVPh40+5%SWNT in the region of -OH vibration.

composites are comprised of –OH groups associated with another –OH on the polymer chain, an interaction that we will term intra-association, and –OH hydrogen bonding with the oxygenated functional groups of the nanotube, an interaction that we will term inter-association. The FTIR spectra, is analyzed to extract the contribution of the free –OH, the inter-associating –OH, and the intra-associating –OH to the measured spectra for each nanocomposites to provide evidence of the interaction between the nanotubes and polymer matrix.

4.3 FTIR Data Analysis

The spectrum of the SWNT used in this study indicates the presence of carbonyl functional groups on the tubes (Figure 4.1); however in the PSVPh-SWNT composites, the carbonyl ($\sim 1630\text{ cm}^{-1}$) band is sufficiently diluted due to the low SWNT concentration (5 wt. %) to make its analysis impractical. Thus, in order to determine the role of polymer–nanotube hydrogen bonding on the ultimate properties of these nanocomposites, the –OH stretching region of the spectrum must be analyzed. It must be noted that a quantitative analysis of the hydroxyl region is inherently difficult due to the vibration overlap of inter- and intra-molecular hydrogen bond association and overtones of carbonyl group.^{75, 105} Hence, the analysis that follows, resolving the vibration bands into free and associated –OH and analyzing these “separate” peaks to quantify the amount of each state of the hydroxyl group present (free vs. hydrogen bonded) does not provide absolute concentrations. The analysis, however, can be carefully used to document the relative change in the contribution of the free or hydrogen bonded –OH to the state of the system among a series of similar samples. Thus, this analysis must be viewed as semi-quantitative, but will provide insight into the role of intermolecular

association between carbon nanotubes and the surrounding polymer matrix on the engineering properties of these nanocomposites. The details of FTIR data analysis is given in Appendix A-1.

PSVPh Copolymers

The fit and deconvoluted peaks of one of the copolymers, PSVPh30, are shown in Figure 4.6. The results obtained from analysis of the deconvoluted peaks for the pure copolymers are given in Table 4.3. The peak around 3540 cm^{-1} corresponds to stretching vibrations of free -OH whereas the peak at 3440 cm^{-1} emerges from stretching vibrations of intra-molecularly associated -OH . Figure 4.7 shows the plot of the ratio of the calculated concentration of free -OH ($C_{F, \text{-OH}}/C_{T, \text{-OH}}$) to total -OH concentration and the ratio of associated OH ($C_{\text{Asso, -OH}}/C_{T, \text{-OH}}$) to total -OH concentration as a function of % vinyl phenol in the copolymer for the pure copolymer samples. The calculated fraction of free hydroxyl groups of the 10% PSVPh copolymer is 0.40, i.e., the contribution due to free -OH to the overall hydroxyl peak is 0.40 whereas the contribution of associated -OH to the whole hydroxyl peak is 0.60. Increasing the vinyl phenol content of the copolymer from 10 to 20% (PSVPh20) decreases the calculated fraction of free hydroxyl groups to 0.20, hence an increase in the vinyl phenol content enhances the intra-molecular -OH association among the polymer chains and reduces the relative concentration of free -OH . This trend continues as the vinyl phenol content is increased to 30% (PSVPh30), where the contribution from free -OH reduces to 0.07 and the contribution from associated -OH increases to 0.93. However, the change in contribution from associated -OH between PSVPh20 and PSVPh30 is less pronounced relative to the corresponding

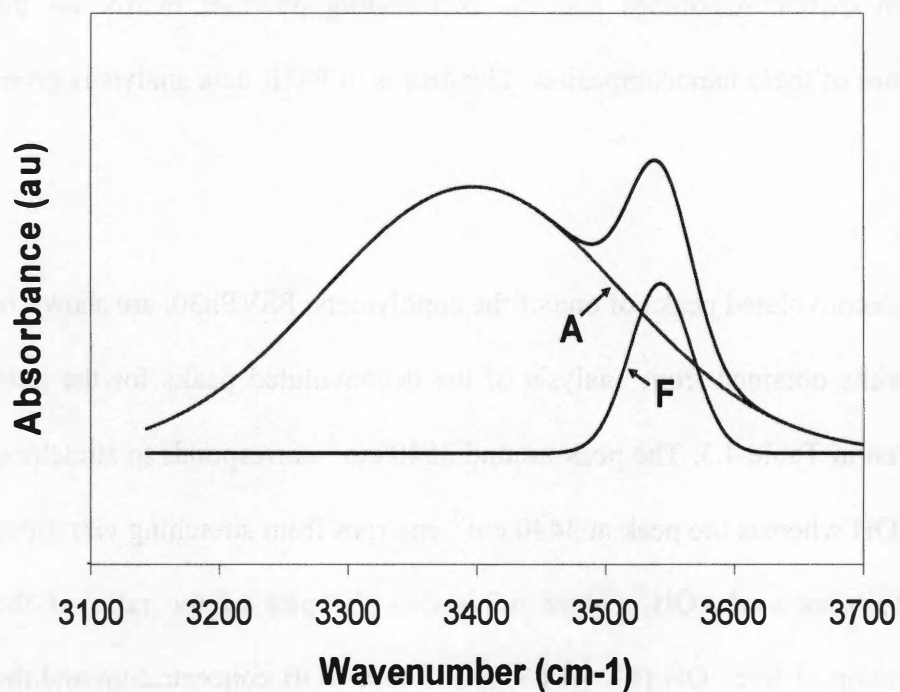


Figure 4.6: Example of fitting and deconvolution procedure for PSVPh30. The curves F and A are deconvoluted peaks assigned for Free and Intra-associated OH bonds respectively obtained from the fit.

Table 4.3: Curve fitting results for PSVPh polymers

	Free OH				Intra Associated OH				$C_{\text{FOH}}/C_{\text{T OH}}$	$C_{\text{asso OH}}/C_{\text{T OH}}$
	$\nu(\text{cm}^{-1})$	$W_{1/2}$	$A_{\text{FOH}}(\text{cm}^{-1})$	C_{FOH}	$\nu(\text{cm}^{-1})$	$W_{1/2}$	$A_{\text{AOH}}(\text{cm}^{-1})$	C_{AOH}		
PSVPh10	3547	21	4.05	471	3440	115	11.49	699	0.40	0.60
PSVPh20	3547	22	2.96	345	3424	116	12.57	1362	0.20	0.80
PSVPh30	3542	22	1.67	194	3399	118	13.86	2763	0.07	0.93
PSVPh40	3541	22	1.20	140	3389	119	14.33	3731	0.04	0.96

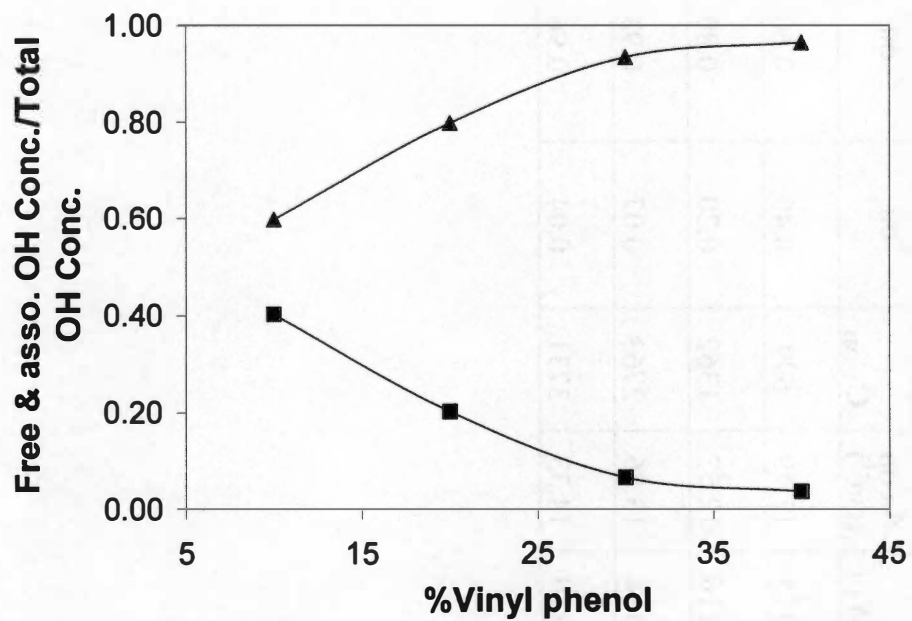


Figure 4.7: Dependence of calculated concentration of free OH to total OH, $C_{F,-OH}/C_{T,-OH}$ (■) and associated OH to total OH, $C_{asso,-OH}/C_{T,-OH}$ (▲) on % vinyl phenol for pure copolymers.

change between PSVPh10 and PSVPh20. For PSVPh40, the contribution of associated –OH is 0.96 as compared to 0.93 for PSVPh30 and the contribution from free –OH is only 0.04 as compared to 0.07 for PSVPh30. The small difference in the values of free and associated –OH contributions to the hydroxyl peak between PSVPh30 and PSVPh40 suggest that at this higher vinyl phenol content, the relative amount of free and associated–OH tends to change slightly with copolymer composition. This can be visualized in Figure 4.7, where a leveling off in the curve is observed after 30% vinyl phenol in both $C_{F,-OH}/C_{T,-OH}$ and $C_{Asso,-OH}/C_{T,-OH}$.

PSVPh-SWNT Composites

The fitting of the experimentally determined FTIR curves to the deconvoluted peaks for one of the composites, the PSVPh30-SWNT nanocomposite is shown in Figure 4.8. The results of the peak deconvolution and fitting process for the PSVPh-SWNT composites are given in Table 4.4. The results are also shown in Figure 4.9 as a plot of the ratio of the calculated concentration of free –OH ($C_{F,-OH}/C_{T,-OH}$) to total –OH concentration and the ratio of inter-associated OH ($C_{I,-OH}/C_{T,-OH}$) to total –OH concentration and the ratio of intra-associated OH ($C_{A,-OH}/C_{T,-OH}$) to total –OH concentration as a function of % vinyl phenol in the copolymer.. In the case of the nanocomposites, the associated –OH peak is resolved into two peaks, namely that of the intra-associated hydrogen bonded –OH and the inter-associated hydrogen bonded –OH. The IR demonstrates that the nanocomposite with the copolymer that has 20% vinyl phenol has the most hydrogen bonding interactions between the nanotube and polymer, which correlates very well with the tensile test results for the composite systems. This agreement of trends between FTIR data and tensile data indicates that increasing inter-

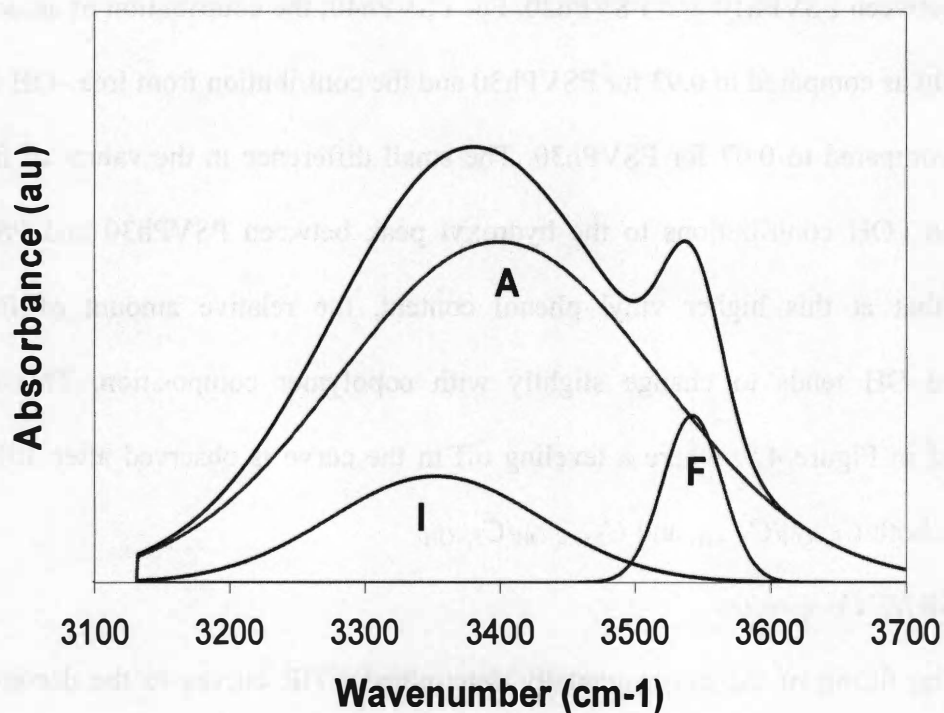


Figure 4.8: Example of fitting and deconvolution procedure for and PSVPh30-SWNT. The curves F, A and I are deconvoluted peaks assigned for Free, Intra- and Inter-associated OH bonds respectively obtained from the fit.

Table 4.4: Curve fitting results for PSVPh-SWNT composites

	Free OH				Intra Associated OH				Inter Associated OH				C_{FOH}/C_{TOH}	$C_{A_{OH}}/C_{TOH}$	$C_{I_{OH}}/C_{TOH}$	$C_{base_{OH}}/C_{TOH}$
	ν (cm^{-1})	$W_{1/2}^*$	A_{FOH} (cm^{-1})	C_{FOH}	ν (cm^{-1})	$W_{1/2}^*$	$A_{A_{OH}}$ (cm^{-1})	$C_{A_{OH}}$	ν (cm^{-1})	$W_{1/2}$	$A_{I_{OH}}$ (cm^{-1})	$C_{I_{OH}}$				
PSVPh10 -SWNT	3547	21	4.46	519	3440	115	9.54	511	3373	50	1.53	82	0.44	0.43	0.07	0.50
PSVPh20 -SWNT	3547	22	1.61	187	3424	116	10.77	1109	3334	79	3.16	325	0.11	0.65	0.19	0.84
PSVPh30 -SWNT	3542	22	1.10	128	3399	118	11.91	2214	3352	78	2.52	467	0.04	0.74	0.16	0.89
PSVPh40 -SWNT	3541	22	1.25	146	3389	119	12.79	3163	3370	82	1.49	368	0.04	0.82	0.10	0.91

* Values fixed during curve fitting

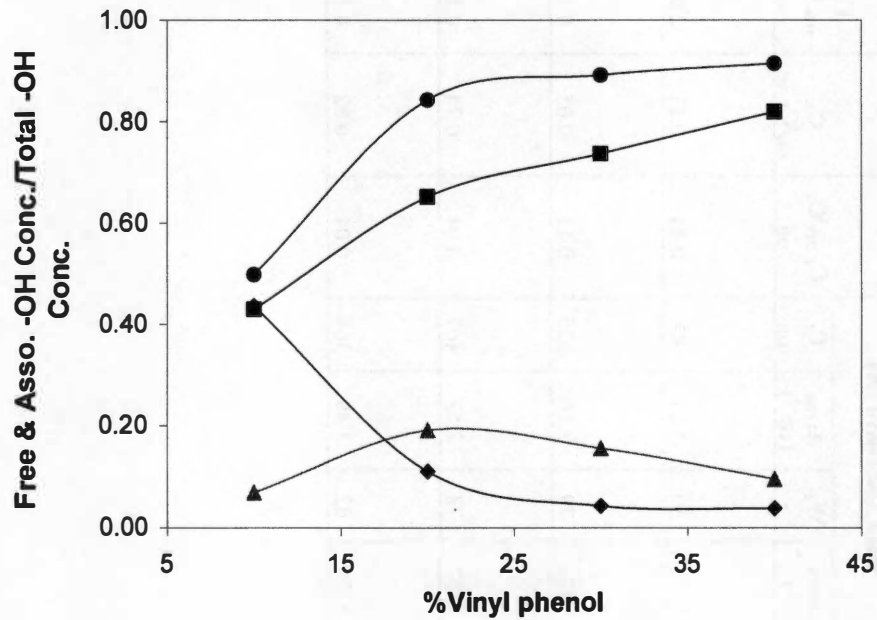


Figure 4.9: Dependence of calculated concentration of free OH to total OH, $C_{F,-OH}/C_{T,-OH}$ (◆), associated OH to total OH, $C_{asso,-OH}/C_{T,-OH}$ (●), intra-associated OH to total OH, $C_{A,-OH}/C_{T,-OH}$ (■) and inter-associated OH to total OH, $C_{I,-OH}/C_{T,-OH}$ (▲) on % vinyl phenol for PSVPh-SWNT composites.

molecular hydrogen bonding between the copolymer and SWNT results in enhanced mechanical strength.

PSVPh-MWNT Composites

The peak deconvolution and fitting results for the PSVPh-MWNT composites are given in Table 4.5 and plotted in Figure 4.10. In general, the trends for the contribution of the free, inter and intra associated –OH groups to the hydroxyl peak in the PSVPh-MWNT composites are similar to PSVPh-SWNT composites. The trends also reasonably compare with the tensile test results for PSVPh-MWNT composites.

4.4 Discussion

In this study, the dependence of the contribution of the free, intra- and inter-associated –OH to the hydroxyl peak in the FTIR spectra of the nanocomposites on the composition of the copolymer and its correlation to the tensile properties of the nanocomposites can be explained in terms of accessibility of the –OH^{76,77,84} on the copolymer chain to participate in hydrogen bonding with the oxygenated functional groups on the nanotubes as discussed in chapters 3. However, in this study, direct observation of changes in the free and associated hydroxyl groups with variation in vinyl phenol content is evident. For a copolymer with a vinyl phenol content as low as 10%, both free and intra-associated –OH groups exist. However, at this vinyl phenol content, insufficient free –OH groups are available to interact with many of the defect sites of the SWNT. This lack of sufficient vinyl phenol groups limits the extent to which the polymer chain can hydrogen bond with the SWNT. This is exemplified in the IR peak analysis which shows a small contribution from the inter-associated –OH (0.08) to the FTIR curve. As the content of vinyl phenol on polymer backbone increases, the amount of

Table 4.5: Curve fitting results for PSVPh-MWNT composites

	Free OH				Intra Associated OH				Inter Associated OH				$C_{F\text{OH}}/C_T$	$C_{A\text{OH}}/C_T$	$C_{I\text{OH}}/C_T$	$C_{\text{asso OH}}/C_{T\text{OH}}$
	ν (cm^{-1})	$W_{1/2}^*$	$A_{F\text{OH}}$ (cm^{-1})	C_F OH	ν (cm^{-1})	$W_{1/2}^*$	$A_{A\text{OH}}$ (cm^{-1})	$C_{A\text{OH}}$	ν (cm^{-1})	$W_{1/2}$	$A_{I\text{OH}}$ (cm^{-1})	C_I OH				
PSVPh10 -MWNT	3547	21	3.17	368	3440	115	10.48	630	3340	58	1.88	113	0.33	0.56	0.10	0.66
PSVPh20 -MWNT	3547	22	2.38	278	3424	116	9.66	986	3346	76	3.49	356	0.16	0.58	0.21	0.79
PSVPh30 -MWNT	3542	22	1.22	142	3399	118	11.55	2153	3346	78	2.76	514	0.05	0.72	0.17	0.89
PSVPh40 -MWNT	3541	22	0.91	105	3389	119	11.95	2919	3337	88	2.67	653	0.03	0.75	0.17	0.92

* Values fixed during curve fitting

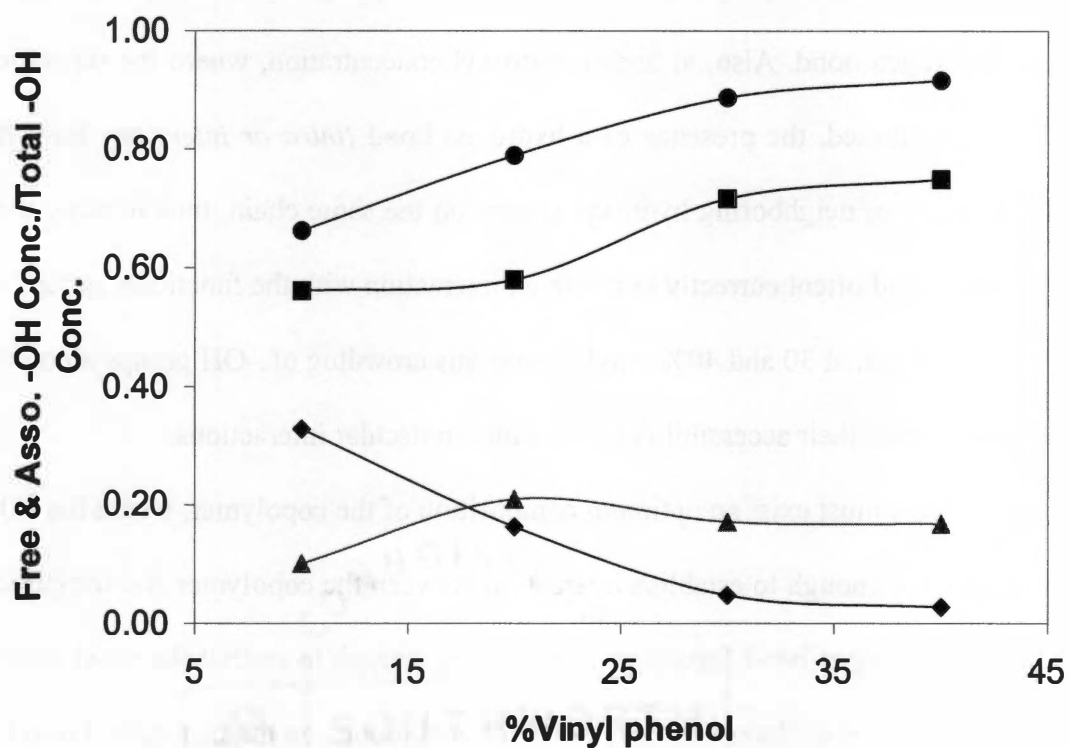


Figure 4.10: Dependence of calculated concentration of free OH to total OH, $C_{F,-OH}/C_{T,-OH}$ (♦), associated OH to total OH, $C_{asso,-OH}/C_{T,-OH}$ (●), intra-associated OH to total OH, $C_{A,-OH}/C_{T,-OH}$ (■) and inter-associated OH to total OH, $C_{I,-OH}/C_{T,-OH}$ (▲) on % vinyl phenol for PSVPh-MWNT composites.

hydroxyl group that can interact with the nanotube increases, and the analysis of the FTIR data indicates that this indeed occurs.

However, as the amount of hydroxyl groups further increases the average distance between vinyl phenol moieties decreases. At some increased vinyl phenol content, the separation between two vinyl phenol groups becomes sufficiently small to promote interaction among hydroxyl groups via hydrogen bonding, or formation of intramolecular hydrogen bond. Also, at higher hydroxyl concentration, where the separation of hydroxyls is limited, the presence of a hydrogen bond (*intra or inter*) can limit the dynamic mobility of neighboring hydroxyl groups on the same chain, thus limiting their ability to access and orient correctly to create an interaction with the functional groups on the nanotubes. Thus, at 30 and 40% vinyl phenol this crowding of –OH groups along the polymer chain limits their accessibility to form intermolecular interactions.

Thus, there must exist an optimum composition of the copolymer, where the –OH population is large enough to establish interaction between the copolymer and the carbon nanotubes but hydrogen bond formation is not strong enough to restrict the vinyl phenol groups on the copolymer chain to access the functional groups on the nanotube. From the tensile results, electrical conductivity, and FTIR analysis, it appears that the copolymer with 20% vinyl phenol corresponds to this optimum state.

Chapter 5

Polymer-Nanofiber Composites: Enhancing Composite Properties by Nanofiber Oxidation

This chapter presents the results that document the mechanical and thermal properties of composites prepared from carbon nanofibers and copolymers of styrene and vinyl phenol with varying vinyl phenol content. The copolymers are synthesized according to the procedure described in Chapter 3. The molecular weights, polydispersity and compositions of the polymers used in this study are given in Table 5.1. The properties of the composites formed with as received nano fibers and oxidized nanofibers are compared and contrasted, with the idea that the oxidized nanofibers contain oxygenated defect sites that can form intermolecular interactions with the hydroxyl group of the vinyl phenol in the matrix copolymer. Carbon nanofibers are oxidized by using ruthenium tetroxide as described in Chapter 2.

5.1 Experimental

Composite Preparation:

Composites were prepared by dissolving 500 mg of the copolymer in THF. Separately, appropriate amount of nanofibers were sonicated for an hour in THF using a sonic bath (Branson 1510, frequency 40 kHz). The polymer solution and the nanofiber dispersion are then mixed together and sonicated for another hour. The resulting mixture was stirred in a fume hood until some of the solvent evaporates. The resulting composite

Table 5.1: Composition and molecular weight of polymers prepared for chapter 5

	% Vinyl phenol	Mn, (g/mol)	PDI
PSVPh10	11.2	93,800	1.71
PSVPh20	21.5	101,000	1.60
PSVPh40	40.7	91,700	1.72

was precipitated into cold methanol (cold hexane for PSVPh40 & its composites), filtered and dried under vacuum at 60-70°C overnight to remove traces of solvent.

Dynamic Mechanical Analysis (DMA)

Mechanical properties of the copolymers and their composites were studied by dynamic mechanical analysis (DMA) using a DMTA V by Rheometrics. In dynamic mechanical analysis an oscillating force is applied to a sample and the material's response is analyzed. The output of a DMA experiment provides the storage modulus, E' , which is representative of the elastic behavior of material, and the loss modulus, E'' , which corresponds to the viscous behavior of the material. The ratio of the loss to storage modulus is known as $\tan \delta$.

The samples for DMA were prepared as follows: the copolymer or the composite material was first placed in a mold (20 x 5 x 1 mm, dimensions within ASTM standard (D5418-99)) with a Mylar layer above and below the mold. The mold was compressed by a mechanical press at 25000 psi, 150°C for 30 minutes, after which the mold was allowed to cool down to room temperature and the composite bar was withdrawn from the mold. The resulting composite bar was kept in an oven at 60-70 °C for 4-5 hours in order to minimize residual mechanical stresses in the bar. DMA measurements were completed using a dual cantilever fixture, ramping the temperature from room temperature to 150 °C at a ramp rate of 2 °C/min and at a constant frequency of 1 Hz.

Scanning Electron Microscopy (SEM)

The dispersion of the nanofibers in the copolymer matrices was observed using scanning electron microscopy (SEM). The fractured surface of the bar for DMA analysis

was analyzed with a Hitachi S4700 SEM. The sample surface was coated with gold to avoid charging under the microscope. The SEM images were acquired at a voltage of 10 kV and a beam current of 20 μ A.

The glass transition temperature (T_g) of the copolymers and composites were measured by differential scanning calorimetry (DSC) (Mettler Toledo model DSC821, calibrated with Indium) from 25 to 160 $^{\circ}$ C at a rate of 10 $^{\circ}$ C/min.

5.2 Results

Dynamic Mechanical Analysis

The storage modulus (E') of the copolymers PSVPh10, PSVPh20 and PSVPh40 and their composites with 1 and 5 weight % oxidized nanofibers as well as with 1 weight% unoxidized nanofibers, are plotted as a function of the temperature in Figures 5.1, 5.2 and 5.3 respectively. The average storage moduli of the composites, averaged from 40 $^{\circ}$ C to 90 $^{\circ}$ C, are summarized in Table 5.2. The average storage modulus is normalized to the modulus of the pure copolymer and plotted as a function of the percent vinyl phenol in the copolymer in Figure 5.4. The storage modulus values are normalized in this figure to account for changes in modulus due to molecular weight and copolymer composition effects.

A modest enhancement of 4% in the storage modulus was observed when 1% unoxidized nanofibers were added to the PSVPh10 copolymer, whereas, the modulus increases by about 11% for the composite of PSVPh10 with 1% oxidized nanofibers. A further increase in the oxidized nanofibers loading to 5% increased the storage modulus by 16% over that of the pure copolymer. A similar trend was observed for the composites

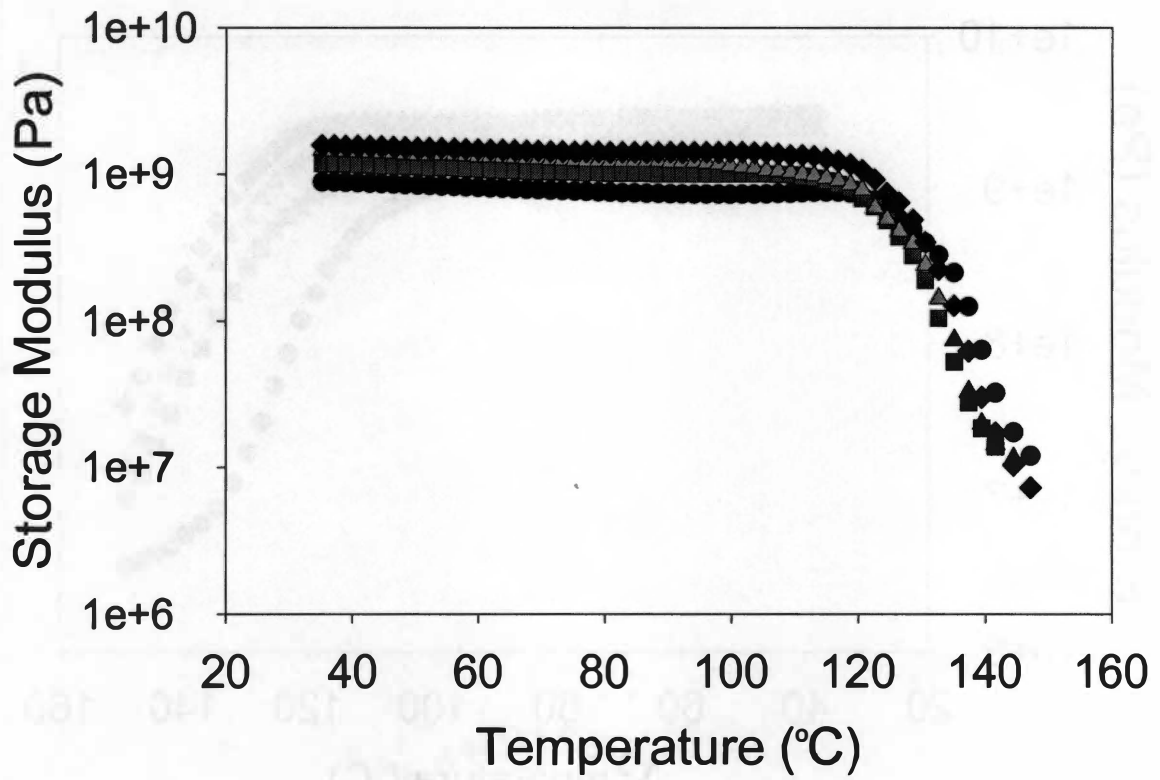


Figure 5.1: Storage modulus (E') versus temperature for PSVPh10 (●) and its composites with 1% unoxidized nanofibers (■), 1% oxidized nanofibers (▲) and 5% oxidized nanofibers (◆).

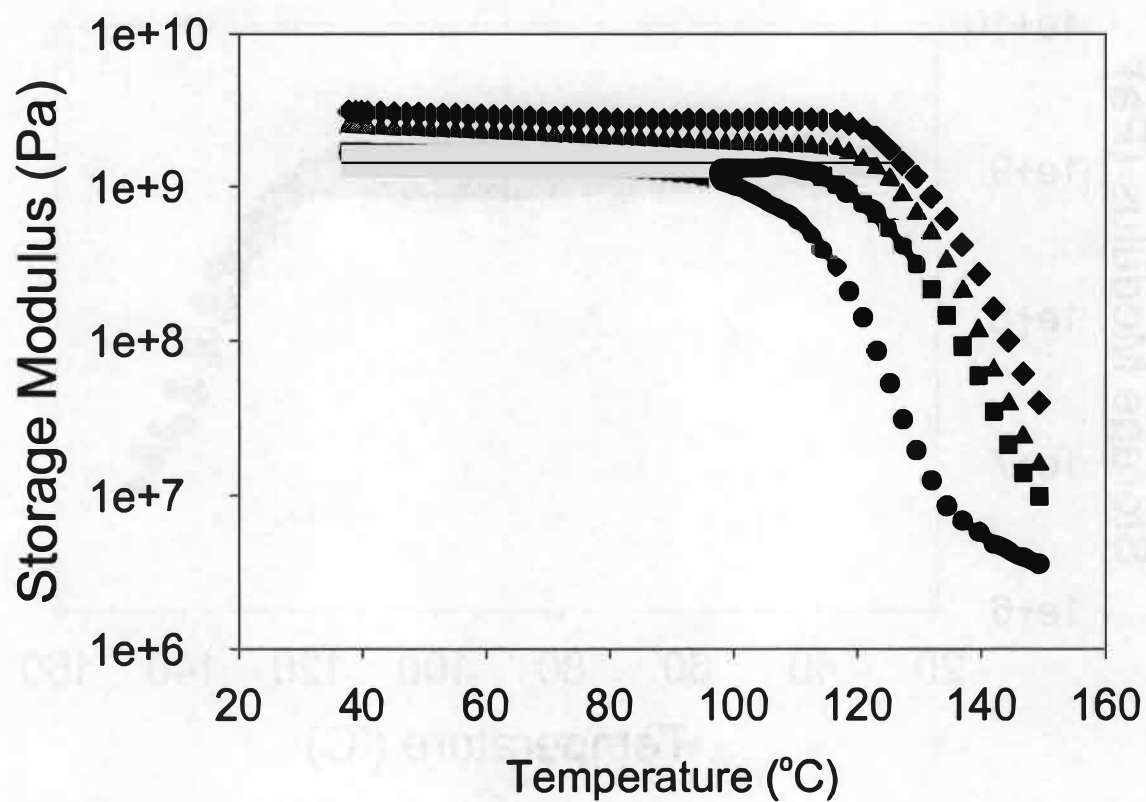


Figure 5.2: Storage modulus (E') versus temperature for PSVPh20 (●) and its composites with 1% unoxidized nanofibers (■), 1% oxidized nanofibers (▲) and 5% oxidized nanofibers (◆).

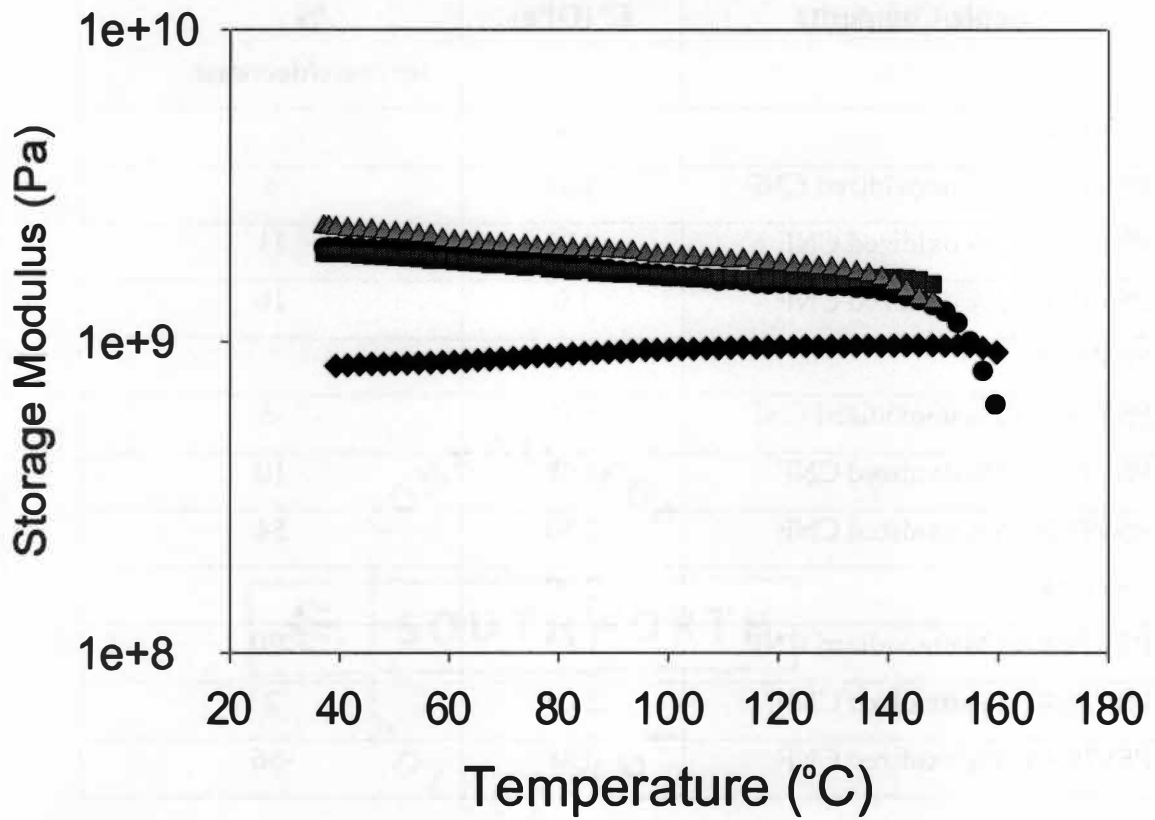


Figure 5.3: Storage modulus (E') versus temperature for PSVPh40 (●) and its composites with 1% unoxidized nanofibers (■), 1% oxidized nanofibers (▲) and 5% oxidized nanofibers (◆).

Table 5.2: Storage modulus for composites of PSVPh and CNF

Sample/Composite	E' (GPa)	% increase/decrease
PSVPh10	0.86	
PSVPh10+1% unoxidized CNF	0.89	4
PSVPh10+1% oxidized CNF	0.96	11
PSVPh10+5% oxidized CNF	1.0	16
PSVPh20	1.62	
PSVPh20+1% unoxidized CNF	1.55	-5
PSVPh20+1% oxidized CNF	1.78	10
PSVPh20+5% oxidized CNF	2.50	54
PSVPh40	2.00	
PSVPh40+1% unoxidized CNF	1.60	-20
PSVPh40+1% oxidized CNF	2.04	2
PSVPh40+5% oxidized CNF	0.88	-56

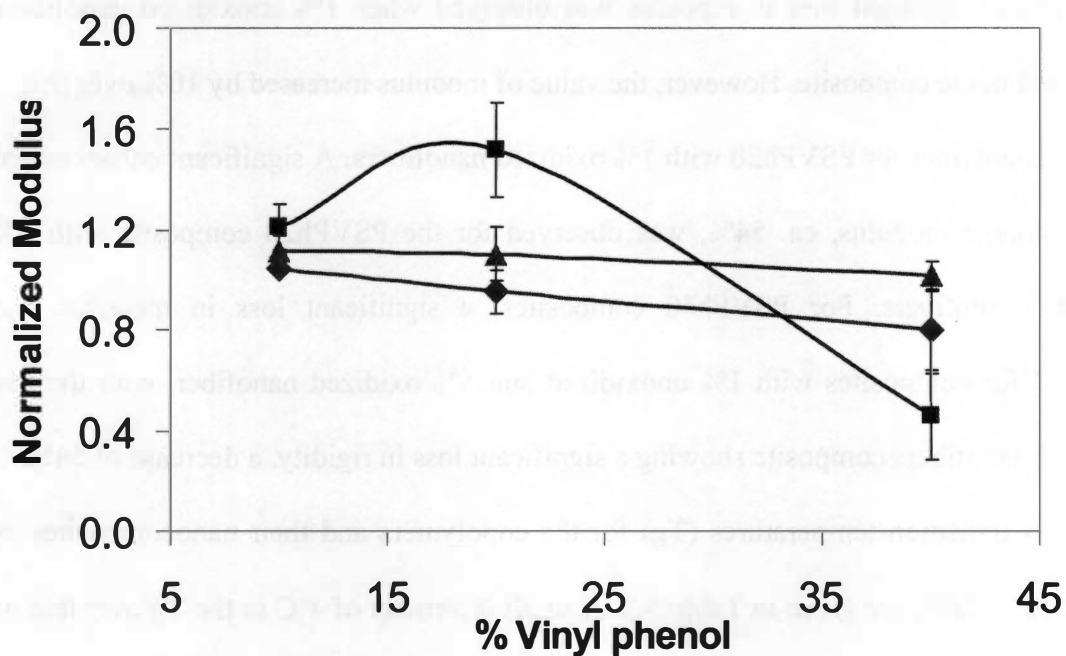


Figure 5.4: Normalized Storage modulus versus % Vinyl phenol for PSVPh+1% unoxidized-CNF (◆), PSVPh+1% oxidized CNF (▲) and PSVPh+5% oxidized CNF (■).

of PSVPh20. A slight loss in modulus was observed when 1% unoxidized nanofibers were used in the composite. However, the value of modulus increased by 10% over that of pure copolymer for PSVPh20 with 1% oxidized nanofibers. A significant enhancement in the storage modulus, ca. 54%, was observed for the PSVPh20 composite with 5% oxidized nanofibers. For PSVPh40 composites, a significant loss in modulus was observed for composites with 1% unoxidized and 5% oxidized nanofiber, with the 5% oxidized nanofibers composite showing a significant loss in rigidity, a decrease of 56%.

The glass transition temperatures (T_g) for the copolymers and their nanocomposites as measured by DSC are given in Table 5.3. A small increment of 4°C in the T_g over that of the pure copolymer is observed for the composite of PSVPh10 with 1% unoxidized nanofibers. For the composite of 1% oxidized nanofiber, the T_g increased by 5°C relative to that of the pure copolymer. Increasing the oxidized nanofiber loading to 5% increases the T_g by 9°C . A similar trend in the T_g was observed for the composites of PSVPh20. A 4°C increment in the T_g for the composite with 1% unoxidized nanofiber was observed, while the composite with 1% oxidized nanofibers exhibits a glass transition increase of 11°C . A further increase in the oxidized nanofiber content to 5% further increases the T_g to 121°C , an enhancement of 13°C . For the composites of PSVPh40, a 2°C increase in T_g was observed for the composite with 1% unoxidized nanofibers, the glass transition temperature increased by 5°C for the composite with 1% oxidized nanofibers, and the T_g increased only 2°C for the composite with 5% oxidized nanofibers.

Table 5.3: Glass transition temperature (T_g, °C) of PSVPh and composites

	Polymer	1% Unoxidized CNF	1% Oxidized CNF	5% Oxidized CNF
PSVPh10	108	112	113	117
PSVPh20	108	112	119	121
PSVPh40	141	143	146	143

Scanning Electron Microscopy

The SEM images of the fractured surfaces of the composites of PSVPh20 and PSVPh40 with 5% oxidized nanofibers are shown in Figure 5.5 and 5.6, respectively. It is evident from these micrographs that the oxidized tubes are dispersed very well in the PSVPh20 matrix, while the composite with PSVPh40 exhibits a very heterogeneous mixture, where there are clumps of nanofibers and large areas with no filler, indicating a very poorly dispersed morphology.

5.3 Discussion

The results demonstrate that the oxidation of the carbon nanofibers and the composition of the copolymer matrix play an important role in the thermal and structural properties, as well as the dispersion, of the final nanocomposite. Generally, the nanocomposites formed from oxidized nanofibers exhibited better mechanical and thermal properties relative to the composites formed with the unoxidized nanofibers. One exception is the composite of the PSVPh40 copolymer and 5% oxidized CNF, where the structural rigidity degraded significantly. Additionally, among the composites with oxidized CNF, the thermal and mechanical properties are optimized for the composite with the PSVPh20 copolymer as the matrix. For all copolymer matrices, the composites of the unoxidized nanofibers provide modest to little change in the thermal and mechanical properties.

The primary difference between the oxidized and the unoxidized nanofibers is the presence of significant oxygenated groups on the oxidized nanofiber surface. One can therefore anticipate that there exists a potential for interaction between the copolymer and the oxidized nanofibers that is absent in the composites with the unoxidized nanotubes.

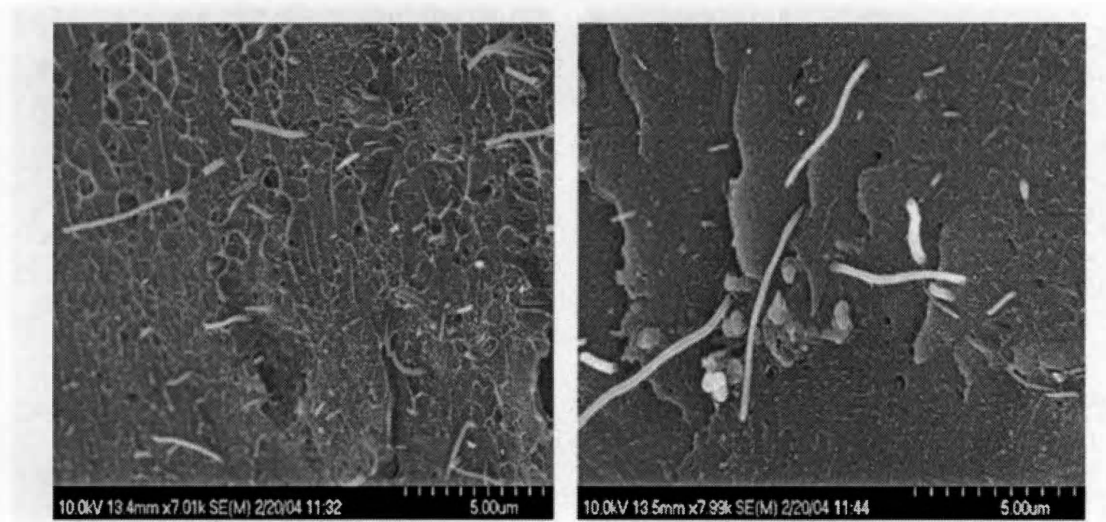


Figure 5.5: SEM images of fractured surface of composite PSVPh20+5% oxidized CNF.

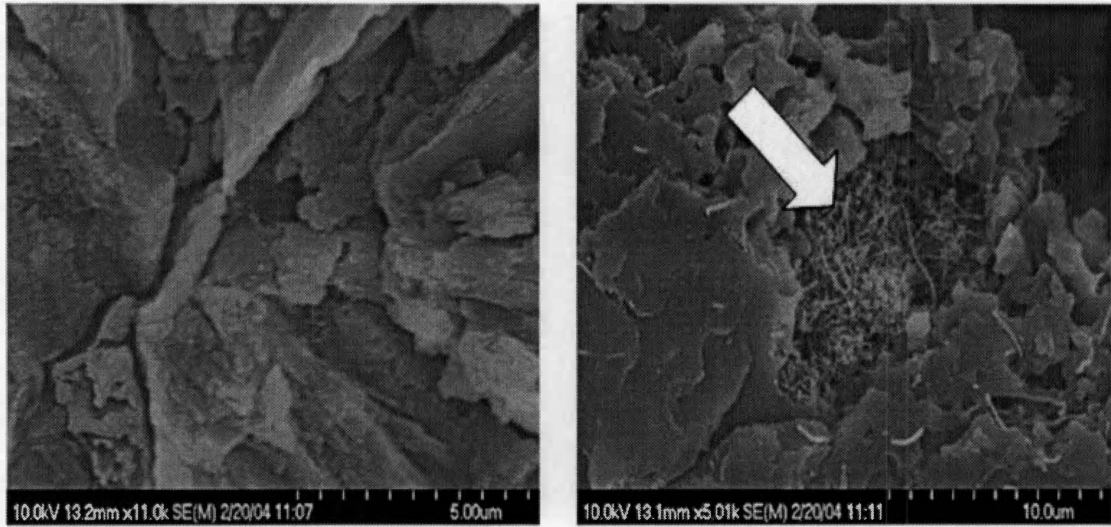


Figure 5.6: SEM images of fractured surface of composite PSVPh40+5% oxidized CNF.

Thus, the observed improvement in thermal and mechanical properties of the oxidized nanotube nanocomposites, which is absent with the unoxidized nanotubes, may be due to an increase in intermolecular interactions that exist between the vinyl phenol groups of the copolymer and the defect sites on the oxidized nanofibers. Attempts to examine these interactions by FTIR spectroscopy were not successful. However, the results are in excellent agreement with previous work on LCP blends by Viswanathan et al⁸⁰⁻⁸⁴ that document that the incorporation of intermolecular hydrogen bonding between the polymers improved miscibility and properties of the resultant blends.

The optimization of the properties in the composites formed with the oxidized nanofibers for the system with the copolymer with 20% vinyl phenol as the matrix can be explained by the presence of intermolecular hydrogen bonding between the polymer and CNF that is optimized for this copolymer composition. The fact that the interactions between the CNF and this copolymer are optimized for this copolymer is related to the accessibility of the hydroxyl groups to form intermolecular interactions between the oxidized CNF and the copolymer chain.

Optimizing the intermolecular interactions between a polymer and SWNT leads to improved dispersion and properties in SWNT composites (as discussed in Chapters 3 & 4) and it is logical to interpret the results presented in this chapter in a similar manner. Moreover, the observed behavior indicates a strong interaction between the polymer matrix and CNF filler. For instance, the mechanical (Figure 5.6) and thermal (Table 5.3) properties of the oxidized nanofiber composites clearly shows that the PSVPh20 composite exhibits the highest storage modulus and maximum enhancement in the glass transition temperature of the oxidized nanofiber composites studied. The enhancement in

the glass transition temperature upon addition of a nanofiller is a manifestation of the restricted segmental chain mobility of the copolymer in the composite, while the enhancement in the modulus in a composite indicates the ability to transfer stress from the polymer matrix to the nanofiber. In both of these cases, intimate interactions between the polymer matrix and nanofibers are critical to the successful observation of these changes upon addition of nanofiller.

Thus, the optimum enhancement in the glass transition for the PSVPh20 oxidized nanofiber composite indicates that there exists a significant restriction on the segmental mobility of these polymer chains, which in turn suggests that the polymer chains are in close proximity and interact significantly with the nanofibers. The improved ability to transfer the load from polymer matrix to the nanofiber as evident by the superior mechanical properties also suggests a strong interaction between the hydroxyl groups of the copolymer and the oxidized nanofiber.

Therefore, the optimization of the mechanical and thermal properties for the oxidized nanofibers composite with the copolymer that contains 20% vinyl phenol can be attributed to the optimization of the interactions between the defect sites of the nanofiber and the vinyl phenol groups of PSVPh20. The enhanced dispersion of the oxidized nanofibers in the PSVPh20 as determined by SEM further substantiates this interpretation.

The correlation of the results in the present study to similar results on SWNT nanocomposites suggests that similar physics are controlling the properties of these nanocomposites, where the oxidized nanotubes are able to form favorable interactions with the vinyl phenol of the matrix copolymer, which in turn correlates to improved

dispersion and increased thermal and mechanical properties of the ultimate nanocomposite. This interpretation is further strengthened by noting the lack of improvement in the thermal or mechanical properties of the nanocomposites formed from the unoxidized nanotubes, which are unable to form these favorable interactions.

Chapter 6

Conclusions and Future Work

The results presented in this thesis clearly establish that the protocol of optimizing the intermolecular interactions that occur between a polymer and nanotubes can enhance the ultimate dispersion in a polymer nanocomposite. The optical microscopy results in chapter 3 and electrical conductivity results in chapter 4 clearly demonstrate that the copolymer composition impacts the extent of dispersion in the nanocomposite. The correlation between the intermolecular interaction that exists between the nanotubes and polymer matrix as measured by Raman spectroscopy (chapter 3) and infra-red spectroscopy (chapter 4) and the observed enhancement in the mechanical and electrical properties of the composite is evident. However, there remains uncertainty as to whether the property improvement is brought about due to improvement in dispersion or is it a result of better adhesion between the phases due to presence of the improved intermolecular interaction. In other words, based on the reported results, it is not clear what the critical reinforcement mechanism is; improved dispersion of the nanofiller or improved adhesion at the polymer-nanofiller interface. Also, the role of the amount of functional groups present on the nanotubes still needs further investigation. The results presented in this thesis clearly point towards the possibility of creating materials with tunable properties in future.

A comparison of the tensile modulus obtained experimentally for the composite of copolymer with 20% vinyl phenol and single walled carbon nanotubes (chapter 4) to

that obtained by using the modified rules of mixture reveals the efficacy of this approach to create an ideally dispersed nanocomposite. The rule of mixtures predicts that the composite modulus, E_C , when fibers (nanotubes in this case) are oriented along the fiber direction is equal to

$$E_C = E_{NT}V_{NT} + E_MV_M \quad (1)$$

where E_C is composite modulus, E_M and V_M are the modulus and volume fraction for polymer matrix, E_{NT} and V_{NT} are modulus and volume fraction for carbon nanotubes.

The rule is modified to account for the orientation effects by Bowyer and Bader¹⁰⁶, as

$$E_C = K_1K_2E_{NT}V_{NT} + E_MV_M \quad (2)$$

where K_1 is the orientation factor, and K_2 is the fiber (nanotubes in this case) orientation factor.

$$K_1 = \frac{1}{E_{NT}V_{NT}} \int_{-\pi/2}^{\pi/2} n(\phi)E(\phi)d\phi$$

$n(\phi)$ is the fraction of nanotubes at an angle ϕ to the applied load, for randomly oriented nanotubes,

$$\int_{-\pi/2}^{\pi/2} n(\phi)d\phi = 1, \text{ which yields } n=1/\pi$$

$$E(\phi) = \left[\frac{\cos^4 \phi}{E_{Voight}} + \frac{\sin^4 \phi}{E_{Reuss}} + \left(\frac{1}{G_{13}} - \frac{2\nu_m}{E_{Voight}} \right) \sin^2 \phi \cos^2 \phi \right]^{-1}$$

where ϕ is the angle of orientation, ν_m is the polymer's Poisson ratio,

$$E_{\text{Voight}} = E_M V_M + E_{NT} V_{NT}$$

$$E_{\text{Reuss}} = \left[\frac{V_{NT}}{E_{NT}} + \frac{V_M}{E_M} \right]^{-1}$$

$$G_{13} = \left[\frac{V_{NT}}{G_{NT}} + \frac{V_M}{G_M} \right]^{-1}$$

where G_{NT} and G_M are the shear moduli for the nanotubes and polymer matrix respectively.

For a tube with very high aspect ratio, which is the case with carbon nanotubes, the nanotube efficiency factor, K_2 can be written as,

$$K_2 = 1 - \frac{1}{4a} \frac{\sigma_{NT}}{\tau_i} \quad \text{if } a \gg \frac{\sigma_{NT}}{\tau_i}$$

where “a” is the nanotubes’ aspect ratio, σ_{NT} is the nanotubes’ tensile strength and τ_i is the shear strength of the polymer nanotube interface.

To estimate the modulus of the nanocomposite containing 20% vinyl phenol with single walled carbon nanotubes by the rule of mixtures, the nanotube modulus is considered to be 1 TPa. The modulus of polymer matrix is obtained from experimental result and is 1.6 GPa (Chapter 4). The volume fraction of the SWNT is calculated based on 5 weight % SWNT in composite and SWNT density of 1.2 g/cm³. The volume fraction of the copolymer is estimated considering 95 weight % and assuming density of copolymer to be equal to that of polystyrene (1.05 g/cm³). The Poisson ratio, ν_m , is considered to be that for polystyrene (0.34). The shear modulus of SWNT, G_{NT} is considered to be 1 GPa taken from reported literature.¹¹ The shear modulus for the copolymer, G_M is calculated according to equation

$$G_M = \frac{E_M}{2(1+\nu_M)}$$

and is calculated to be 0.60 GPa. The tensile strength of nanotubes, σ_{NT} is considered to be 150 GPa. The interfacial shear strength of polymer-nanotube interface is taken from literature value to be 75 MPa.³³ To estimate the aspect ratio of the nanotubes, it is assumed that the tubes are 1000 nm long with a diameter of 1.3 nm. Substituting the values in eq (2), the estimated modulus of an ideal composite containing polymer with 20% vinyl phenol and 5% single walled carbon nanotubes, is, ~3.3 GPa. The value however, is relatively higher than the one measured experimentally (2.9 GPa).

The lower experimental value of the tensile modulus could be attributed to a number of factors including the presence of nanotubes in bundles, the state of dispersion of the nanotubes in the polymer matrix and possible slippage at the polymer-nanotube interface. Additionally, the Young's modulus used for nanotubes in the rule of mixture equation is evaluated for a defect free nanotube. However, in our experiment, the presence of defects in the form of the oxygenated functional groups was confirmed by infrared spectroscopy. Is it possible that the presence of defects are making the nanotubes weaker as argued by Wagner⁴, thereby the entire composite is weaker than anticipated? To date there is no study that provides the experimental evidence of the weakening of nanotubes by the presence of defects. In order to create an ultimate composite whose measure properties matches the predicted values, it is critical to understand this fundamental question, hence towards the end of this thesis, the following questions are proposed to pursue for future investigations;

- (1) Does incorporating different amounts of defects (functional groups) on the nanotubes alter their properties and the properties of resultant composite?**
- (2) Can a surfactant (breaking the bundles apart and not letting them aggregate back) be used in the similar system to further enhance the dispersion and properties?**
- (3) Does incorporating functional groups on nanotubes alter its properties?**
- (4) What are the effects of creating covalent linkages between the polymer and the nanotubes?**

REFERENCES

1. 1987
2. 1987
3. 1987
4. 1987
5. 1987
6. 1987
7. 1987
8. 1987
9. 1987
10. 1987
11. 1987
12. 1987
13. 1987
14. 1987
15. 1987
16. 1987
17. 1987
18. 1987
19. 1987
20. 1987
21. 1987
22. 1987
23. 1987
24. 1987
25. 1987
26. 1987
27. 1987
28. 1987
29. 1987
30. 1987
31. 1987
32. 1987
33. 1987
34. 1987
35. 1987
36. 1987
37. 1987
38. 1987
39. 1987
40. 1987
41. 1987
42. 1987
43. 1987
44. 1987
45. 1987
46. 1987
47. 1987
48. 1987
49. 1987
50. 1987
51. 1987
52. 1987
53. 1987
54. 1987
55. 1987
56. 1987
57. 1987
58. 1987
59. 1987
60. 1987
61. 1987
62. 1987
63. 1987
64. 1987
65. 1987
66. 1987
67. 1987
68. 1987
69. 1987
70. 1987
71. 1987
72. 1987
73. 1987
74. 1987
75. 1987
76. 1987
77. 1987
78. 1987
79. 1987
80. 1987
81. 1987
82. 1987
83. 1987
84. 1987
85. 1987
86. 1987
87. 1987
88. 1987
89. 1987
90. 1987
91. 1987
92. 1987
93. 1987
94. 1987
95. 1987
96. 1987
97. 1987
98. 1987
99. 1987
100. 1987

References

1. Ebbesen, T. W.; *Carbon Nanotubes: Preparation & properties*, CRC press, 1997.
2. Drzal, L. T.; Rich, M. J.; Lloyd, P. F. *The Journal of Adhesion*, 1982, 16, 1-30.
3. Tibbetts, G. G.; Gorkiewicz, D. W.; Hammond, Jr. D. C. *US Patent No. 5024, 818*, 1991.
4. Kumar, S.; Doshi, H.; Srinivasarao, M.; Park, J. O.; Schiraldi, D. *Polymer*, 2002, 43, 1701-1793.
5. Glasgow, D. G.; Burton, D.; Hughes, T. W.; Lake, M. L. Paper presented at Nanocomposite 2002, Amsterdam, The Netherlands, 28-29 January 2002.
6. Iijima, S. *Nature* 1991 354, 56
7. Ajayan, P. M.; Lambert, J. M.; Bernier, P.; Barbedette, L.; Colliex, C.; Planeix, J. M., *Chem Phys Lett*, 1993, 215, 509-517.
8. Falvo, M. R.; Clary, G. J.; Taylor II, R. M.; Chi, V.; Brooks Jr, F. P.; Washburn, S.; Superfine, R. *Nature*, 1997, 389, 582-584.
9. Wong, W. E.; Sheehan, P. E.; Lieber, C. M. *Science*, 1997, 277, 1971-1975.
10. Treacy, M. M. J.; Ebbesen, T. W.; Gibson, J. M. *Nature*, 1996, 381, 678-680.
11. Salvétat, J. P.; Briggs, G. A. D.; Bonard, J. M.; Revathi, R. B.; Kulik, A. J.; Stockli, T.; Burnham, N. A.; Forro, L. *Phys Rev Lett* 1999, 82, 944-947.
12. Mackeyev, Y. A.; Marks, J. W.; Rosenblum, M. G.; Wilson, L. J. *J.Phys. Chem. B* 2005, 109, 5482-5484.
13. Jang, B. Z. *Advanced Polymer Composites: Principals and Applications* published by ASM International, Materials Park, OH 1994.

14. Dresselhaus, M. S.; Dresselhaus, G.; Saito, R. *Phys. Rev. B* **1992**, *45*, 6234-6242.
15. Hone, J.; Llaguno, M. C.; Biercuk, M. J.; Johnson, A. T.; Batlogg, B.; Fischer, J. E. *Appl. Phys. A* **2002**, *74*, 339-343.
16. Tans, S. J.; Devoret, M. H.; Dai, H.; Thess, A.; Smalley, R. E.; Geerligs, L. J. *Nature* **1997**, *386*, 474-477.
17. Satio, S. *Science* **1997**, *278*, 77-78.
18. Lefebvre, J.; Antonov, R. D.; Radosavljevic, M.; Lynch, J. F.; Liaguno, M.; Johnson, A. T. *Carbon* **2000**, *38*, 1745-1749.
19. Collins, P. G.; Zettl, A.; Bando, H.; Thess, A.; Smalley, R. E. *Science* **1997**, *278*, 100-103.
20. Tans, S. J.; Verschueren, A. R. M.; Dekker, C. *Nature* **1998**, *393*, 49-52.
21. Li, S.; Yu, Z.; Yen, S. F.; Tang, W. C.; Burke, P. J. *Nano Letters* **2004**, *4*, 753-756.
22. Heer, W. A.; Chatelain, A.; Ugarte, D. *Science* **1995**, *270*, 1179-1180.
23. Wang, Q. H.; Setlur, A. A.; Lauerhaas, J. M.; Dai, J. Y.; Seelig, E. W.; Chang, R. P. H. *App Phys Let* **1998**, *72*, 29122913.
24. Rinzler, A. G. *Science* **1995**, *269*, 1550.
25. Saito, Y.; Uemura, S. *Carbon* **2000**, *38*, 169.
26. Calvert, P. *Nature* **1999**, *399*, 210-211.
27. Baughman, R. H., Zakhidov, A. A., Heer, W. A. *Science* **2002**, *297*, 787-792.
28. Drzal, L. T., Rich, M. J., Lloyd, P. F., *J. Adhes.* **1983**, *16*, 1-30.
29. Hughes, J. D. H., *Compos. Sci. Technol.* **1991**, *41*, 13-33.
30. Kim, J-K., Mai Y-W., *Compos. Sci. Technol.* **1991**, *41*, 333-378.

31. Liao, K.; Li, S. *App Phys Lett* **2001**, *79*, 4225-4227.
32. Frankland, S. J. V.; Caglar, A.; Brenner, D. W.; Griebel, M. *J. Phys Chem B* **2002**, *106*, 3046-3048.
33. Wagner, H. D. *Chem Phys Lett* **2002**, *361*, 57-61.
34. Frankland, S. J. V.; Harik, V. M.; Odegard, G. M.; Brenner, D. W.; Gates, T. S. *Comp Sci Tech* **2003**, *63*, 1655-1661.
35. Gou, J.; Minaie, B.; Wang, B.; Liang, Z.; Zhang, C. *Computational Mat Sci* **2004**, *31*, 225-236.
36. Lourie, O.; Wagner, H. D. *App Phys Lett* **1998**, *73*, 3527.
37. Bower, C.; Rosen, R.; Jin, L. *App Phys Lett* **1999**, *74*, 3317-3319.
38. Change, H. B.; Liu, Z. Q.; Sun, L. F.; Tang, D. S.; Zhou, W. Y.; Wang, G.; Qian, L. X.; Xie, S. S.; Fen, J. H.; Wan, M. X. *J Low Temp Phys* **2000**, *119*, 41-48.
39. Ding, W.; Eitan, A.; Fisher, F. T.; Chen, X.; Dikin, D. A.; Andrews, R.; Brinson, L. C.; Schadler, L. S.; Ruoff, R. S. *Nano Lett* **2003**, *3*, 1593-1597.
40. Schadler, L. S.; Giannaris, S. C.; Ajayan, P. M. *App Phys Lett* **1998**, *73*, 3842-3844.
41. Ajayan, P. M.; Schadler, L. S.; Giannaris, C.; Rubio, A. *Adv Mater* **2000**, *12*, 750-753.
42. Wood, J. R.; Frogley, M. D.; Meurs, E. R.; Prins, A. D.; Peijs, T.; Dunstan, D. J.; Wagner, H. D. *J. Phys. Chem. B* **1999**, *103*, 10388-10392.
43. Wood, J. R.; Zhao, Q.; Frogley, M. D.; Meurs, E. R.; Prins, A. D.; Peijs, T.; Dunstan, D. J.; Wagner, H. D. *Physical Review B* **2000**, *62*, 7571-7575.
44. Cooper, C. A.; Young, R. J.; Halsall, M. *Composites A* **2001**, *32*, 401-411.

45. Ausman, K. D.; Piner, R.; Lourie, O.; Ruoff, R. S. *J. Phys Chem B* **2000**, *104*, 8911-8915.
46. Kong, J.; Dai, H. *J. Phys. Chem. B* **2001**, *105*, 2890-2893.
47. Kong, J.; Franklin, N. R.; Zhou, C.; Chapline, M. G.; Peng, S.; Cho, K.; Dai, H. *Science* **2000**, *287*, 622-625.
48. Adu, C. K. W.; Sumanasekera, G. U.; Pradhan, B. K.; Romero, H. E.; Eklund, P. *C. Chem Phys Lett* **337**, 2001, 31-35.
49. Zhang, J.; Lee, J. K.; Wu, Y.; Murray, R. W. *Nano Lett* **2003**, *3*, 403-407.
50. Wise, K. E.; Park, C.; Siochi, E. J.; Harrison, J. S. *Chem Phys Lett* **2004**, *391*, 207-211.
51. Shim, M.; Javey, A.; Kam, N. W. S.; Dai, H. *J Am Chem Soc* **2001**, *123*, 11512-11513.
52. Claye, A.; Rahman, S.; Fischer, J. E.; Sirenko, A.; Sumanasekera, G. U.; Eklund, P. *C. Chem Phys Lett* **2001**, *333*, 16-22.
53. Jouguelet, E.; Mathis, C.; Petit, P. *Chem Phys Lett* **2000**, *318*, 561-564.
54. Wagner, H. D.; Lourie, O.; Feldman, Y.; Tenne, R. *Appl Phys Lett* **1998**, *72*, 188-190.
55. Cooper, A. C., Cohen, S. R., Barber, A. H., Wagner H. D. *Applied Physics Letters*, **2002**, *81*, 3873-3875
56. Barber, A. H., Cohen, S. R., Wagner, H. D. *Applied Physics Letters*, **2003**, *82*, 4140-4142
57. Poggi, M. A., Lillehei, P. T., Bottomley, L. A. *Chem of Mat.* **2005**, *17*, 4289-4295.

58. Poggi, M. A., Bottomley, L. A., Lillehei, P. T. *Nano Letters* **2004**, *4*, 61-64
59. Wong, M.; Paramsothy, M.; Xu, X. J.; Ren, Y.; Li, S.; Liao, K. *Polymer* **2003**, *44*, 7757-7764.
60. Haggemueller, R.; Gommans, H. H.; Rinzler, A. G.; Fischer, J. E.; Winey, K. I. *Chem Phys Lett* **2000**, *330*, 219-225.
61. Gou, J.; Liang, Z.; Zhang, C.; Wang, B. *Composite B* **2005**, *36*, 524-533.
62. Jin, X.; Pramoda, K. P.; Xu, G.; Goh, S. H. *Chem. Phys. Lett.* **2001**, *337*, 43-47.
63. Thostenson, E. T.; Ren, Z.; Chou, T. W. *Comps. Sci. Technol.* **2001**, *61*, 1899-1912.
64. Thostenson, E. T.; Chou, T. W. *J. Phys. D: Appl Phys* **2002**, *35*, 77-80.
65. Shaffter, M. S. P.; Windle, A. H. *Adv. Mater.* **1999**, *11*, 937-941.
66. Gong, X.; Liu, J.; Baskaran, S.; Voise, R. D.; Young, J. S. *Chem. Mater.* **2000**, *12*, 1049-1052.
67. Jia, Z.; Wang, Z.; Xu, C.; Liang, J.; Wei, B.; Wu, D.; Zhu, S. *Mater. Sci. Eng. A* **1999**, *271*, 395-400.
68. Zhu, J.; Kim, J.; Peng, H.; Margrave, J. L.; Khabashesku, V. N.; Barrera, E. V. *Nano Lett* **2003**, *3*, 1107-1113.
69. Zhang, X., Liu, T., Sreekumar, T. V., Kumar, S., Moore, V. C., Hauge, R. H., Smalley, R. E. *Nano Letters* **2003**, *3*, 1285-1288.
70. Geng, H.; Rosen, R.; Zheng, B.; Shimoda, H.; Fleming, L.; Liu, J.; Zhou, O. *Adv Mater* **2002**, *14*, 1387-1390.
71. Putz, K. W.; Mitchell, C. A.; Krishnamoorti, R. L.; Green, P. F. *J Polym Sci Part B: Polym Phys* **2004**, *42*, 2286-2293.

72. Grady, B. P.; Pompeo, F.; Shambaugh, R. L.; Resasco, D. E. *J Phys Chem B* **2002**, *106*, 5852-5858.
73. Painter, P. C.; Tang Wei-Long, Graf, J. F.; Thomson, B.; Coleman, M. M. *Macromolecules* **1991**, *24*, 3929-3936.
74. Coleman, M. M.; Pehlert, G. J.; Painter, P. C. *Macromolecules* **1996**, *29*, 6820-6831.
75. Coleman, M. M.; Lee, K. H.; Skrovanek, D. J.; Painter, P. C. *Macromolecules* **1986**, *19*, 2149
76. Eastwood, E.; Viswanathan, S.; O'Brien, C. P.; Kumar, D.; Dadmun, M. D. *Polymer*, **2005**, *46*, 3957.
77. Viswanathan, S.; Dadmun, M. D. *Macromolecules* **2003**, *36*, 3196-3205.
78. Viswanathan, S.; Dadmun, M. D. *Macromol. Rapid Commun.* **2001**, *22*, 779-782.
79. Viswanathan, S.; Dadmun, M. D. *Macromolecules* **2002**, *35*, 5049-5060.
80. Viswanathan, S.; Dadmun, M. D. *J. Poly. Sci.: Poly. Phys.*, **2004**, *42*, 1010-1022.
81. Bom, D., Andrews, R., Jacques, D., Anthony, J., Chen, B., Meier, M. S., Selegue, J. P. *Nano Letters*, **2002**, Vol 2, No. 6, 615-619
82. Mawhinney, D. B., Naumenko, V., Kuznetsova, A., Yates Jr., J. T., Liu, J., Smalley, R. E., *Chemical Physics Letters* **2000**, *324*, 213-216
83. Liu, J.; Rinzler, A. G.; Dai, H.; Hafner, J. H.; Kelley, B. R.; Boul, P. J.; Lu, A.; Iverson, T.; Shelimov, K.; Huffman, C. B.; Rodriguez-Macias, F.; Shon, Y. S.; Lee, R. T.; Colbert, D. T.; Smalley, R. E. *Science* **1998**, *280*, 1253
84. Hernadi, K.; Siska, L.; Thien-Nga, K.; Forro, L.; Kiricsi, I. *Solid State Ionics* **2001**, *141*, 203-209

85. Kuznetsova, A.; Popova, I.; Yates, J.T.; Jr.Bronikowski, M. J.; Huffman, C. B.; Liu, J.; Smalley, R. E.; Hwu, H.H.; Chen, J. G.; *J. Am. Chem. Soc.* **2001**, *123*, 10699.
86. Zhang, J.; Zou, H.; Qing, Q.; Yang, Y.; Li, Q.; Liu, Z.; Guo, X.; Du, Z. *J.Phys. Chem. B.* **2003**, *107*, 3712-3718.
87. Satishkumar, B. C.; Govindaraj, A.; Mofokeng, J.; Subbanna, G. N.; Rao, C. N. *R. J. Phys. B: At. Mol. Opt. Phys.* **1996** *29*, 4925-4934
88. Hwang, K. C. *J. Chem. Soc., Chem. Commun.* **1995**, 173
89. Yao, N.; Lordi, V.; Ma, S. X. *C. J. Mater. Res.* **1998**, *13*, 2432-2437
90. Banerjee, S.; Micheal, G. C. K.; Stainlaus, S. W.; *Chem. Eur. J.* **2003**, *9*, 1898-1908.
91. Spitzer, U. A.; Lee, D. G. *J. Org. Chem.* **1974**, *39*, 2468
92. Nunez, M. T.; Martin, V. S. *J. Org. Chem.* **1990**, *55*, 1928-1932
93. Mendez, A.; Bermejo, J.; Santamarfa, R.; Blanco, C. G.; Menendez, R. *Energy & Fuels* **2000**, *14*, 936-942
94. Ashby, E. C.; Goel, A. B.; *J. Org. Chem.* **1981**, *46*, 3936-3938
95. Colomer, J. F.; Piedigrosson, P.; Willems, I.; Journet, C.; Bernier, P.; Van G. T. , *J. Chem. Soc., Faraday Trans.* **1998**, *94*, 3753
96. Dresselhaus, M. S.; Dresselhaus, G.; Eklund, P. C. *Science of Fullerenes and Carbon Nanotube*, Academic Press 1996
97. Endo, M.; Nishimura, K.; Kim, Y. A.; Hakamada, K.; Matushita. T.; Dresselhaus, M. S.; Dresselhaus, G. *J. of Mat. Res.* **1999**, *14*, 4474-4477.

98. Hamon, M. A.; Hu, H.; Bhowmik, P.; Niyogi, S.; Zhao, B.; Itkis, M. E.; Haddon, R. C. *Chemical Physics Letters* **2001**, *347*, 8-12
99. Radmard, B.; Dadmun, M. D. *Polymer* **2001**, *42*, 1591-1600.
100. Poretzky, A. A.; Geohegan, D. B.; Fan, X.; Pennycook, S. J. *Appl. Phys. A* **2000**, *70*, 153
101. Kyotani, T.; Nakazaki S.; Xu W.; Tomita A. *Carbon* **2001** *39* 782-785
102. Dresselhaus, M. S.; Dresselhaus, G.; Jorio, A.; Souza Filho, A. G.; Saito, R. *Carbon* **2002**, *40*, 2043-2061
103. Zhao, Q.; Wagner, D. *Phil. Trans. R. Soc. Lond. A* **2004**, *362*, 2407-2424.
104. Li, S., Qin, Y., Shi, J., Gou, Z. X., Li, Y., Zhu, D. *Chem. Mater* **2005**, *17*, 130-135
105. Li, D.; Brisson, J. *Polymer* **1998**, *39*, 793-800
106. Bowyer, W. H.; Bader, M. G. *J Mat Sci* **1972**, *7*, 1315-1321.

APPENDIX

APPENDIX

A-1

Details of FTIR Analysis

PeakFit v4.11 software was used to analyze the –OH bond stretching region in the FTIR spectra. In all fitting procedures, a Gaussian band shape was assumed. The –OH region between 3700-3100 cm^{-1} was resolved into free and associated –OH groups. During this deconvolution process in the analysis of the nanocomposites, the position and the width of the free and intra-associated hydrogen bonded –OH groups were fixed at those observed for the pure copolymer. The position and the width of the inter-associated –OH were allowed to vary in the fitting process.

The absorbance of a given vibration can be quantified using Beer-Lambert's law according to

$$A = a \cdot b \cdot C \quad (1)$$

where A is the absorbance of a given vibration, a is its absorption coefficient, b is the path length or the sample thickness, and C is the concentration of the vibration group in the sample. The total concentration of –OH in the copolymer and the composite can be expressed as

$$C_{T,-OH} = C_{F,-OH} + C_{Asso,-OH} \quad (2)$$

where $C_{T,-OH}$ is the total –OH concentration, $C_{F,-OH}$ is the concentration of free –OH groups and $C_{Asso,-OH}$ is the concentration of –OH that participate in hydrogen bonding.

The total –OH concentration in the sample can be calculated from

$$C_{T,-OH} = d \cdot w f_{VPH} / M, \quad (3)$$

where d is the polymer density, w is the weight fraction of polymer in the system, f_{VPh} , is the molar fraction of vinyl phenol present in the copolymer and M is the molecular weight of vinyl phenol repeat unit. The concentration of free OH is calculated using eq. 1 in the form:

$$C_{F,-OH} = A_{F,-OH} / (a_{F,-OH} \cdot b) \quad (4)$$

The concentration of associated –OH is obtained by subtracting the concentration of free –OH from the total concentration of –OH. In eq. 4, the absorption coefficient for the free –OH vibration ($a_{F,-OH}$) is determined from the calculated values of the free –OH concentration and film thickness of PVPh, as well as the reported values for its absorbance,⁹⁶ and is used for all copolymer and composite systems.

In the nanotube-polymer composite system, the associated –OH group can be separated into contributions from the intra-associated –OH group and the inter-associated –OH group. The total –OH in the composite system is thus, given as,

$$C_{T,-OH} = C_{F,-OH} + C_{I,-OH} + C_{A,-OH} \quad (5)$$

where $C_{I,-OH}$ is the concentration of hydrogen bonded –OH via inter-association and $C_{A,-OH}$ is the concentration of hydrogen bonded –OH via intra association. The values for $C_{I,-OH}$ and $C_{A,-OH}$ are calculated from

$$C_{I,-OH} = A_{I,-OH} / (a_{asso,-OH} \cdot b) \quad (6)$$

$$C_{A,-OH} = A_{A,-OH} / (a_{asso,-OH} \cdot b) \quad (7)$$

respectively, where $A_{I,-OH}$ and $A_{A,-OH}$ are determined experimentally from the FTIR spectra and the fitting process. Due to the overlap of the inter- and intra-associated –OH peaks, it was assumed that the absorption coefficients for inter- and intra-associated –OH are the same. Since, the values of absorption coefficients and thickness are same in eq. 6

and eq. 7, the ratio $C_{I,-OH} / C_{A,-OH}$ is equal to $A_{I,-OH} / A_{A,-OH}$. Normalizing the values of $A_{I,-OH}$ and $A_{A,-OH}$ to 1, the concentration of inter- and intra-associated -OH can then be calculated by multiplying the normalized absorbance of inter- and intra-associated -OH to the concentration of associated -OH respectively.

The assumption that the absorption coefficients for inter- and intra-associated -OH are the same is a potential source of error in quantifying the -OH concentration and for this reason, the values that emerge from this analysis can only be used to compare the data presented here, and the values presented do not indicate an absolute measure of the percent -OH that are free or hydrogen bonded in each sample.

Vita

Asif Rasheed was born on November 24, 1970 in Karachi, Pakistan. He attended junior and high school in Karachi. In 1993 he completed his undergraduate degree in Applied Chemistry from University of Karachi. He worked as a technologist for an engineering consultancy company from June 1994 to January 1996. He joined King Fahd University of Petroleum and Minerals in February 1996 to pursue higher studies and received MS in Chemistry in May 1998. He worked in Saudi Basic Chemical Industries (Sabic) research center as Catalyst Technologist from January 1998 to June 2000. He joined University of Tennessee, Knoxville in the fall of 2000. He successfully defended his dissertation on March 8, 2006 and graduated following May. He accepted a postdoctoral research position in the School of polymer, textile and fiber engineering, Georgia Institute of Technology beginning in May of 2006.

4582 4346 5
07/28/06 MFB